January 2012

Theoretical Studies Of The Ground And Low-Lying Excited States Of [3,3']bidiazirinylidene(c2n4), Tetramethyleneethane Diradical, And Arsenic And Selenium Oxides

Rashel Makane Mokambe Sumpter

THEORETICAL STUDIES OF THE GROUND AND LOW-LYING EXCITED STATES OF [3,3']BIDIAZIRINYLIDENE(C_2N_4), TETRAMETHYLENEETHANE DIRADICAL, AND ARSENIC AND SELENIUM OXIDES

by

Rashel Makane Mokambe Sumpter
Bachelor of Science, University of Lagos, 1988
Master of Science, University of Lagos, 1989

A Dissertation
Submitted to the Graduate Faculty

of the

University of North Dakota

In partial fulfillment of the requirements

for the degree of

Doctor of Philosophy

Grand Forks, North Dakota
August
2012

This dissertation, submitted by Rashel Makane Mokambe Sumpter in partial fulfillment of the requirements for the Degree of Doctor of Philosophy from the University of North Dakota, has been read by the Faculty Advisory Committee under whom the work has been done and is hereby approved.

_____
Dr. Mark R Hoffmann (Chairperson)

_____
Dr. Harmon Abrahamson

_____
Dr. Lothar Stahl

_____
Dr. Kathryn A Thomasson

_____
Dr. Ju Kim

This dissertation meets the standards for appearance, conforms to the style and format requirements of the Graduate School of the University of North Dakota, and is hereby approved.

_____
Dr. Wayne Swisher
Dean of the Graduate School

_____
Date

PERMISSION

Title:	Theoretical Studies of The Ground And Low-Lying Excited States of [3,3']Bidiazirinylidene(C_2N_4), Tetramethyleneethane Diradical, And Arsenic And Selenium Oxides
Department:	Chemistry
Degree:	Doctor of Philosophy

In presenting this dissertation in partial fulfillment of the requirements for a graduate degree from the University of North Dakota, I agree that the library of this University shall make it freely available for inspection. I further agree that the permission for extensive copying for scholarly purpose may be granted by the professor who supervised my dissertation work or, in his absence, by the chairperson of the department or the dean of the Graduate School. It is understood that any copying or publication or other use of this dissertation or part thereof for financial gain shall not be allowed without my written permission. It is also understood that due recognition shall be given to me and to the University of North Dakota in any scholarly use which may be made of any material in my dissertation.

Signature _____
Rashel Makane Mokambe Sumpter

Date 06-21-12

TABLE OF CONTENTS

Page

LIST OF FIGURES

Figure Page

LIST OF TABLES

Table Page

ABBREVIATIONS

Abbreviation	Definition
aug-cc-pVDZ	Augmented Correlation Consistent Polarized Valence Double Zeta
aug-cc-pVTZ	Augmented Correlation Consistent Polarized Valence Triple Zeta
BLYP	Becke-Lee-Yang-Parr Exchange Correlation Functional
B3LYP	Becke's 3 parameter Lee-Yang-Parr Exchange Correlation Functional
CASSCF	Complete Active Space Self-Consistent Field
cc-pVDZ	Correlation Consistent Polarized Valence Double Zeta
cc-pVTZ	Correlation Consistent Polarized Valence Triple Zeta
CCSD	Coupled Cluster with Single and Double Excitations
CCSD(T)	Coupled Cluster Singles and Doubles with inclusion of pertubative Triple Excitations
CI	Configuration Interaction
CISD	Configuration Interaction with Singles and Doubles Excitations
CR-CCSD(T)	Completely Renormalized Coupled Cluster Singles and Doubles with inclusion of pertubative Triple Excitations
CSF	Configuration State Function
DFT	Density Functional Theory
EOM-CCSD	Equation-of-motion Coupled-Cluster method with Single and Double Excitations
FORS	Full optimized reaction space

GGA	Generalized Gradient Approximation
GUGA	Graphical Unitary Group Approach
GVVPT2	Second-order Generalized Van Vleck Perturbation Theory
LANL2DZ	Los Alamos National Laboratory 2-double-Z
LDA	Local Density Approximation
LSDA	Local Spin Density Approximation
MBPT	Many-Body Perturbation Theory
MCSCF	Multi-Configuration Self-Consistent Field
MP2	Second-order Møller-Plesset Pertubation Theory
MRCISD	Multireference Configuration Interaction including Single and Double Excitations
MRPT	Multireference Pertubation Theory
OS-SCS-MP2	Open-shell Spin-component-scaled Second-order Møller-Plesset Perturbation Theory
PES	Potential Energy Surface
QCAS-SCF	Quasi-Complete Active Space Self-Consistent Field
QCI	Quadratic Configuration Interaction
QCISD(T)	Quadratic Configuration Interaction with Single and Double Excitations and perturbative inclusion of Triple Excitations
QDPT	Quasi-Degenerate Perturbation Theory
RAS-SCF	Restricted Active Space Self-Consistent Field
SCF	Self-Consistent Field
SC-QDPT	Self-consistent Quasi-Degenerate Perturbation Theory
SCS-MP2	Spin-component-scaled Second-order Møller-Plesset Perturbation Theory

SLYP	Slater Lee-Yang-Parr Exchange Correlation Functional
SVWW	Slater Vosko-Wilk-Nusair Exchange-Correlation Functional
TDDFT	Time-Dependent Density Functional Theory
TZ2P	Triple Zeta plus Double Polarization
UNDMOL	University of North Dakota Molecular Electronic Structure Code

ACKNOWLEDGEMENTS

I want to really thank my Research Advisor Prof. Mark R Hoffmann for the opportunity he gave me not just to work in his group, but that of fulfilling my dream of going back to school for a Ph.D in Chemistry. He has been a father, mentor and very encouraging and patient; without his guidance and support the realization of this dissertation would not have been possible. I also want to thank the present and past members of my Graduate Advisory Committee, Drs. Kathryn Thomasson, Harmon Abrahamson, Lothar Stahl, Ju Kim, Anamitro Banerjee, Ewan Delbridge and Juana Moreno for their guidance, support and time. Very special thanks to Drs. Yuri Khait and Zhenhua Chen for their willingness to help me at all times.

I would like to thank the members of Prof. Hoffmann's research group especially Patrick Tamukong, Jason Hicks, Eric Timian, Kristine Carlson, Drs. Yvonne Bongfen Mbote, Daniel Theis, Alexander Azenkeng, Wanyi Jiang and Yuanjun Li. We have lived like a family and I appreciated every moment we spent together. I also extend a warm thank you to all the faculty, staff and graduate students of UND Chemistry Department especially Dr. Julie Abrahamson, Dr. Irina Smoliakova, Dr. Relindis Mawo-Sunjo, Kenneth Ngale and Boris Sango.

I would also thank my sisters Felicity Mokambe and Mrs Rebecca Mokwe, my niece and nephew Zinata Mokambe and Masoma Ndume and my entire family for their support and love.

The people who deserve my most sincere thanks are my mother Hannah Diale Mokambe and my daughter Nasare Etah Nde Bea and my beloved husband Joseph Sumpter, who has been a constant source of support and encouragement especially during difficult times. Finally, all of these would not have been accomplished without the help of the Almighty God. There were times I felt like giving up but prayers kept me going and finally it is done.

ABSTRACT

The prediction and characterization of molecules with small energy gaps between their ground and low-lying excited electronic states is of interest in a number of areas. In this dissertation, four types of molecules that probe the characteristic of small gap molecules, i.e., [3,3']bidiazirinylidene (C_2N_4), tetramethyleneethane (TME) diradical, As_nO_m and Se_nO_m are described.

The recent interest in the search for molecular species having long-lived metastable ground states has led to the investigation of the ground and low-lying excited electronic states of [3,3']bidiazirinylidene (C_2N_4), using the second order generalized Van Vleck perturbation theory (GVVPT2) variant of multireference perturbation theory. In all the low-lying electronic excitations it was observed that the CN_2 ring is maintained and that it is highly multiconfigurational.

Studies of ground and low-lying excited states of [3,3']bidiazirinylidene molecule continued with the relaxation of the symmetry to C_{2v}. The lowest $^1A_1$ ground state was observed to be lower in energy than the lowest ^1A_g state for the same molecule in D_{2h} symmetry by 0.075 eV (1.73 kcal/mol). This suggests that the molecule has multiple minima on its ground state surface.

Previously studied low-lying singlet and triplet states of tetramethyleneethane (TME) diradical have been revisited using second-order generalized Van Vleck perturbation theory. This was motivated by disagreements for the ground state of TME

molecules between previous experimental and theoretical results, GVVPT2 results on TME with C_1 symmetry confirms that the ground state of TME diradical is very sensitive to geometry.

Toxic trace elements released in the environment may have great adverse effect on human health and the ecosystem. Some arsenic and selenium semi-metals and their oxides have been found to be toxic and their toxicity depends on its oxidation state. GVVPT2 method alongside other methods has been employed in this study to obtain an understanding of the species, the structures of the oxides and their transition states. Moreover, the barriers between the different structures of the compounds have been calculated. Four stable structures and three transition states for As_2O_3, and three stable structures and two transition states for Se_2O_3 were observed. For As_2O_5 seven stable structures and for transition states, and for Se_2O_5, three stable isomers and one transition states were also observed. In general, results on the metalloid oxides show that they can exist in different stable structures and that little energy is needed for the metalloid oxides to be transformed from one local minimum to another.

CHAPTER I

INTRODUCTION

The geometric structures (or isomers) and electronic states in which molecules exist affect, sometimes profoundly, their thermal and photochemical reactions. Molecules with small energy gaps between their ground and low-lying excited electronic states are of interest in a number of areas: as energy carriers or for laser excitation; for utilizing both spin and magnetic properties; and relative to environmental pollution. In this dissertation, the prediction and characterization of the electronic structures and equilibrium geometries of the following compounds; [3,3′]bidiazirinylidene (C_2N_4), tetramethyleneethane diradical (C_6H_8), and various arsenic and selenium oxides are the points of focus. The principal technique used in achieving this goal is a high level *ab initio* method that accurately accounts for both dynamic and nondynamic electronic correlation effects accurately. These theoretical studies are pertinent in assisting experimentalists to gain understanding of the spectroscopic properties, equilibrium geometries, and thermodynamic stabilities of these compounds. Transition state structures, which are generally experimentally inaccessible or need to be inferred from other data, have also been optimized for some of these compounds. Due to the small energy gaps of the compounds studied in this dissertation, the monitoring of their structures experimentally are difficult, more so, some occur at elevated temperatures.

The main high level *ab initio* electronic structure method used in carrying out the studies in this dissertation is the second order generalized Van Vleck perturbation theory

(GVVPT2) method [1], a variant of multireference perturbation theory. The GVVPT2 level of theory is the method of choice because the low-lying ground and excited states of [3,3′]bidiazirinylidene, the low-lying singlet and triplet states of tetramethyleneethane diradical, and many of the arsenic and selenium oxides are highly multiconfigurational in nature. To obtain accurate energies, it is necessary to use a multireference method that is capable of treating equally both the nondynamic and dynamic electron correlation effects of these systems. The GVVPT2 method meets these requirements, since it gives a balanced treatment of nondynamic and dynamic correlation effects [1]. GVVPT2 has proved to be sufficiently accurate in describing the ground and excited electronic states of closely related polyatomic molecules to the principal molecules of interest, giving results comparable to those of coupled cluster with singles and doubles excitations with perturbative triples [CCSD(T)] when CCSD is applicable [2, 3], and it is free from intruder state problems, guaranteeing smooth potential energy surfaces. In this dissertation, GVVPT2 results for the ground states are in general found to agree with those of quadratic configuration interaction with single and double excitations (QCISD) [4], and CCSD(T), and the excited states results agree with those of equation of motion-coupled cluster singles and doubles excitations (EOM-CCSD). Previously, GVVPT2 has been shown to be a credible alternative to multireference configuration interaction with single and double excitations (MRCISD) [5] which is computationally very intensive. GVVPT2 can be applied to a broad range of geometries.

The B3LYP variant of density functional theory (DFT) [6, 7] was used to optimize the geometries of some arsenic and selenium oxides and their transition states. The optimized geometries of the low-lying singlet and triplet states of tetramethyleethane

diradical were studied using B3LYP and CASSCF(6,6). On the optimized geometries obtained, GVVPT2 single point calculations were done, using MCSCF [8] optimized orbitals. In the course of performing these studies, codes were written to broaden the range of calculations that the existing local codes could handle. To the University of North Dakota Molecular Electronic Structure Code (UNDMOL) package, a spin-component-scaled MP2 (SCS-MP2) code was realized during dissertation research and is presented in this dissertation. The motivation for working on the SCS-MP2 code was to get a computationally less intensive method than CCSD(T) for open-shell molecules.

[3,3′]Bidiazirinylidene (C_2N_4)

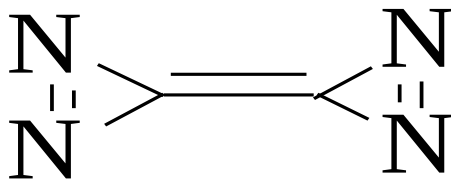

Figure 1. D_{2h} symmetry having two equivalent CN_2 rings for C_2N_4 molecule.

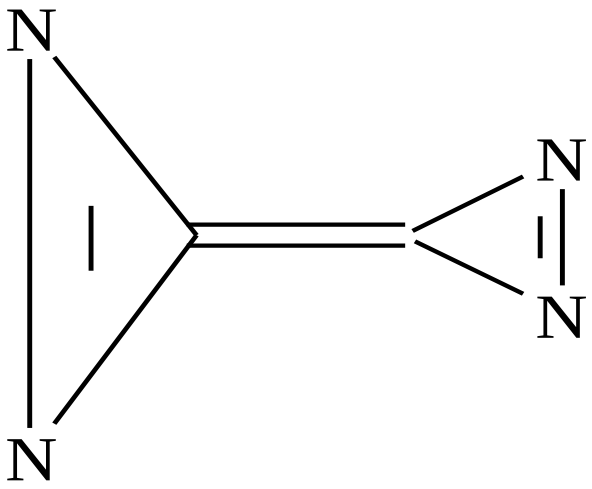

Figure 2. C_{2v} symmetry having two unequivalent CN_2 rings in C_2N_4 molecule.

Research interest in diazirine and its derivatives has increased lately because of their applicability. They are high energy density molecules due to the presence of their three-membered CN_2 rings which cause them to be highly strained and metastable in nature [2, 9]. Upon dissociation and/or combustion, their energy yields can be large, leading to their use as explosives, propellants and rocket fuels, and laser excitation sources, etc. They are a preferred source of carbene, a reactive intermediate, which has an important role in many areas of chemistry, e.g., in understanding the mechanism of some reactions like molecular interactions between small bioactive ligands and proteins [10-12], and difluoromethylation of olefins [13, 14]. Their use as a source of carbene is due to their relative stability, ease of handling and production of carbenes at short irradiation time [10]. In order to have an understanding of the electronic structure and properties of the low-lying electronic states of diazirine (DA) and 3,3' dimethyldiazirine (DMD), Han et al. [15], used *ab initio* quantum chemical methods and found that the first excited singlet state is of $^1B_1$ symmetry, resulting from the n-π^* transition, while that of the triplet state is of the $^3B_2$ symmetry resulting from the π-π^* transition. Theoretical studies on difluorodiazirine by Boldyrev et al. [9] showed that it dissociates to $CF_2 + N_2$ with the release of 28.9 kcal/mol energy. The difluorocarbene diradical produced is used for stereospecific difluoromethylation of olefin. Pandey et al. [2] used the GVVPT2 method to study the ground and low-lying excited electronic states of difluorodiazirine. The GVVPT2 method addressed all the states of interest without any computational or mathematical difficulties.

Since there is still need for novel high energy density molecules with better handling and also new carbene sources, a diazirine derivative, [3,3′]bidiazirinylidene

(C_2N_4) with two CN_2 rings is investigated in this dissertation. The geometrical parameters and spectroscopic properties of this compound were unknown. Moreover, there is no theoretical or experimental information about the ground or low-lying excited states of this compound. From the theoretical study of related molecules like difluorodiazirine, it was anticipated that this molecule should have unusual properties and will be multiference in nature, making the use of conventional *ab initio* methods for its study challenging.

The high level *ab initio* correlated method GVVPT2 was used to study the ground and several low-lying excited states of D_{2h} symmetry (2^1A_g, 1^1B_{1g}, 1^3B_{1g}, 1^1B_{2g}, 1^3B_{2g}, 1^1B_{3g}, 1^3B_{3g},1^1B_{2u},1^3B_{2u}, 1^1B_{3u}, and 1^3B_{3u}) and of C_{2v} symmetry (2^1A_1, 1^1B_1, 1^3B_1, 1^1B_2, 1^3B_2, 1^1A_2, 1^3A_2) of this molecule. Its ground and low–lying equilibrium geometries, adiabatic and vertical excitation energies and vertical emission energies were obtained. These results were expected to give insight into the electronic structure and spectroscopic properties of this molecule and to be useful in describing the reaction pathway of its photolytic decomposition.

Tetramethyleneethane diradical (C_6H_8)

In recent times, there has been a growing interest in the study of diradicals by both experimentalists [16-18] and theoreticians [19, 20]. Diradicals are of interest because they are often intermediates or transition states in a number of reactions, especially thermal or photochemical reactions [21, 22]. Diradicals account for the kinetics, stereochemistry and the magnetic properties of these important reactions [23]. A good understanding of diradicals is needed to have an insight into the mechanism [17] and reactivity of such reactions. Diradicals can permit both intermolecular and

intramolecular coupling reactions because they have two binding sites [17, 18], that is, their two electrons can occupy two exactly or approximately degenerate orbitals. Slipchenko et al. [17] illustrated this phenomenon by explicitly considering six Slater determinants that can be generated by distributing two electrons in two molecular orbitals as follows:

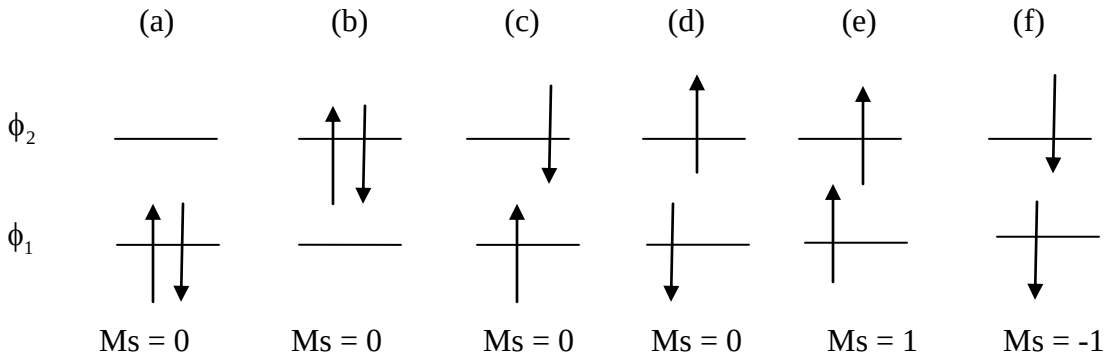

Figure 3. Slater determinants that can be generated by distributing two electrons in two molecular orbitals.

From the above determinants in Figure 3, the following six wavefunctions can be written:

$$\Psi_1^s = \tfrac{1}{2}\left[\lambda(\phi_1)^2 - \sqrt{1-\lambda^2}(\phi_2)^2\right](\alpha\beta - \beta\alpha), \quad (1)$$

$$\Psi_2^s = \tfrac{1}{2}\left[\lambda(\phi_1)^2 + \sqrt{1-\lambda^2}(\phi_2)^2\right](\alpha\beta - \beta\alpha), \quad (2)$$

$$\Psi_3^s = \tfrac{1}{2}(\phi_1\phi_2 + \phi_2\phi_1)(\alpha\beta - \beta\alpha), \quad (3)$$

$$\Psi_1^t = \tfrac{1}{2}(\phi_1\phi_2 - \phi_2\phi_1)(\alpha\beta + \beta\alpha), \quad (4)$$

$$\Psi_2^t = \tfrac{1}{\sqrt{2}}(\phi_1\phi_2 - \phi_2\phi_1)(\alpha\alpha), \quad (5)$$

$$\Psi_3^t = \tfrac{1}{\sqrt{2}}(\phi_1\phi_2 - \phi_2\phi_1)(\beta\beta), \quad (6)$$

That is, three singlet and three triplet wavefunctions as shown above, with $\phi_i \phi_j$ representing $\phi_i(1)\phi_j(2)$, while $\alpha\beta$ stands for $\alpha(1)\beta(2)$. From the above wave functions, it follows that a diradical can be well described only by a multiconfigurational model, such as multiconfigurational self-consistent field (MCSCF) [8, 24, 25]. Because of the exact or approximate degeneracy of the orbitals, the low-lying singlet and triplet states of diradicals often have close energies [19, 23, 26], thus, determination of the ground state is a challenge. A single reference wave function cannot give a good description of such diradical. A yet better description of the energy of a diradical can be achieved by the inclusion of dynamic electron correlation, which can be afforded by the GVVPT2 [1] method. This is the case with tetramethyleneethane diradical, which is a disjoint organic radical, see Figure 4.

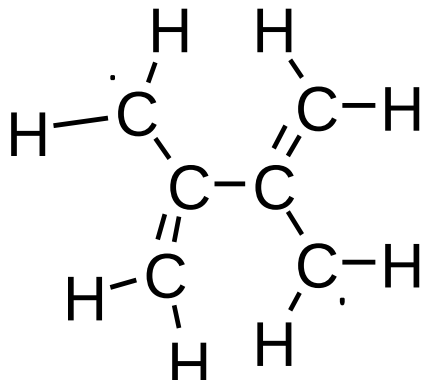

Figure 4. Tetramethyleneethane (TME) diradical

The identification of the ground state of tetramethyleneethane diradical has brought a lot of debate between experimentalists [27, 28] and theoreticians [29, 30]. Dowd in 1970 [27] synthesized TME and recorded its EPR spectrum. From its Curie-Weiss plot, which is linear, he arrived at the conclusion that either the ground state was a triplet state, or the singlet and triplet states were degenerate [27, 28]. Borden et al. [30]

performed SCF calculations on TME and found the ground state to be singlet. Ovchinnikov's [31] theoretical calculations also showed that the ground state of TME is a singlet. Nachtigall et al. carried out SD-CI/TZ2P [32] single point energy calculations on MCSCF(6,6)/3-21G [33] optimized parameters and arrived at a conclusion that the triplet state of TME lies energetically about 1.0 – 1.5 kcal/mol below the single state [33] . This finding of his almost reconciled the experiment and theory. However, Clifford et al. [16] carried out negative ion photoelectron spectroscopy of the $[TME]^-$ anion and their results showed that the ground state of TME in the gas phase is in a singlet state. Filatov et al. [34], in 1999, used the spin-restricted ensemble-referenced Kohn-Sham (REKS) method and their calculations indicated that the ground state of TME is the singlet state. Later, in 2001, Pittner et al. [20], used multireference coupled cluster theories (MRCC); their result showed the singlet state of TME to be the ground state. However, high-level theoretical calculations for the ordering of the lowest singlet and triplet states of TME are still rare. In Chapter IV of this dissertation, GVVPT2 results on the low-lying singlet and triplet states of TME will be presented and discussed.

Arsenic oxides

Arsenic oxides and their dimmers can be expected to have rich and complex structures with some resemblance to oxides of nitrogen. Practical interest in the study of arsenic in this dissertation is based in part on the fact that arsenic in the environment has become a public health concern, due to its toxicity, and because it adversely affects power production. It acts as a chronic poison, and thus poses a risk to humans, animals and plants. It leads to the cause of several diseases like diabetes [35], hypertension [36], ischemic heart disease [37], peripheral vascular disease and cancers of the skin, bladder,

liver and lung [38-40]. Besides its effect on health, arsenic affects equipment negatively. It poisons the catalytic converter used in selective catalytic reduction (SCR) of NO_x [41, 42]. Recently the Department of Toxic Substances Control (DTSC) has been awarded a Training Research and Technical Assistance Grant to conduct an Arsenic Relative Bioavailability Study by the United States Environmental Protection Agency Region IX (USEPA) [43]. Natural sources and occurrences of arsenic in the environment are: mineral species, for example arsenopyrite [44]; volcanic actions followed by low temperature volatilization; inorganic arsenic of geological origin found in underground water used as drinking water, for example in Bangladesh [45, 46]; and organic arsenic compounds such as arsenobetaine, arsenocholine, tetramethylarsonium salts, arsenosugars and arsenic-containing lipids, mainly found in marine organisms although some of these compounds have also been found in terrestrial species [47]. By high-temperature combustion processes, such as coal-fired power generation plants, burning vegetation and volcanic processes, arsenic is emitted into the atmosphere [45, 47, 48]. In the course of the emission, a major fraction is trapped on fly ash particles, but a significant amount is released into the environment through flue-gas stacks [44]. The arsenic released into the atmosphere adds up; therefore there arises a need for an effective means of removal of arsenic. An understanding of the form in which arsenic occurs in the fly ash and flue gases is needed. Because its toxicity and the development of good methods for its removal depend on its form and structure, speciation of arsenic release in fly ash has been studied experimentally in many areas around the world. Huggins et al. [44] and Shah et al. [41] used X-ray absorption fine structure spectroscopy (XAFS) to study the oxidation states and speciation of arsenic in fly ash and stated that arsenic is

present in the As(V) state. Monahan-Pendergast et al. [49] used theoretical methods to predict the species of arsenic under atmospheric conditions and the result was that all favored reactions can occur under tropospheric conditions.

Irrespective of the fact that concerns have been shown about the impending danger of the presence of As in the environment, there are relatively few studies in the literature about the form, structure and the mechanistic pathway of the formation of molecular compounds of arsenic. However, since the formation of As compounds released into the atmosphere usually occurs at elevated temperatures and in chemically complex environments, direct experimental studies of the forms, structure and the mechanistic pathway of the formation of these species can be a challenge. From a theoretical perspective, only methods that can account for both dynamic and nondynamic electron correlation, that is high level *ab initio* methods, can be expected to be reliable. It is for these reasons that these studies are done, by the use of GVVPT2 and CR-CCSD(T) [50-53] methods. The GVVPT2 and CR-CCSD(T) methods are used to study the types of arsenic species likely to be formed, their stabilities and some possible reaction pathways.

Selenium oxides

Selenium is both a toxic and an essential element, but the gap between how much is essential and how much is toxic is not known precisely and is known to be small [54, 55]. The toxicological, nutritional, and biochemical impact of selenium on a biological system depends on its oxidation state, form [41, 54], and concentration present [41, 54]. In Australia, both selenium deficiency and toxicity have been experienced [41]. Zheng et al. [56] reported that there are about 500 cases of human selenosis in southern China, due to the use of selenium-rich carbonaceous shales. It is reported that domestic animals with

a consumption of forage containing 1 mg/kg and above have experienced selenium poisoning [57]. On the other hand Clark et al. found that selenium-enriched yeast dietary supplements significantly limit the development of colorectal, lung and prostate cancers [58]. But the detailed metabolic pathways of selenium compounds acting as anti-carcinogenic agents in the human body are not fully understood. This uncertainty surrounding selenium reveals that potential hazards exist and indicates the need for further research into the structures and forms of selenium compounds found in the environment and relevant reaction pathways. The oxidation states in which selenium is present in its compounds are: -2, 0, +4, and +6. About 70 – 80% of selenium in coal occurs in a form related to organic materials, and about 5 – 10% is present with pyrite, FeS_2 [41, 44, 57], in which it substitutes sulfur. The form in which selenium occurs is known to be directly related to its absorption, metabolic activity, and anti-carcinogenic activity. For example, selenomethionine is suggested to be less toxic than the inorganic forms of selenium [54, 59]. Selenium, because of it high volatility during coal combustion, is released into the atmosphere through flue gas emission. Studies on trace element emission by Zhang et al. [60] showed that the volatility of selenium increases with increases in combustion temperature. Andren et al. [61] did some chemical tests and found that, at about 150°C, flue gas contains mainly elemental selenium. Meanwhile, thermodynamic calculations showed that Se is present as gaseous SeO_2 [60] at high temperatures with some transforming to gaseous SeO [60, 62]. Some experimental techniques like microwave spectroscopy have been used to determine the geometries of a few selenium compounds like: $SeCl_2$, SeO and SeO_2 [63, 64]. Urban et al. [65] performed theoretical studies on the properties and reactions involving selenium

compounds present in coal combustion flue gases using density functional theory and a broad range of other *ab initio* methods. Their results revealed that the use of DFT B3LYP/LANL2DZ for the prediction of enthalpy changes were inconsistent through each reaction, with errors as large as about 50 kcal/mol when compared to experimental results. On the other hand, use of the 6-311++G(3df,3pd) basis set with QCI and CC methods did a good job producing differences within 5 kcal/mol for each reaction of their experimental value. Monahan-Pendergast et al. [49] used *ab initio* methods to study the thermochemical properties of selenium species thought to be released into the atmosphere during coal combustion. They studied the following reactions:

$$Se + OH \rightarrow SeOH \quad (7)$$

$$Se + HO_2 \rightarrow SeO + OH \quad (8)$$

$$SeO + HO_2 \rightarrow SeO_2 + OH \quad (9)$$

Their results showed that the best performance was obtained from the used of QCISD/6-311G* and QCISD with the ECP28MWBl variant of Stuttgart psuedopotentials. The above methods and basis set were then used to perform single point energy calculations. Their results showed that the selenium atom is more likely to be oxidized by the OH radical to form SeOH rather than by HO_2 radical to form SeO. The oxidation of SeO was favored [57] by reaction with HO_2 and not by OH radicals. Irrespective of the known potentially adverse effects of selenium in the environment, relatively few studies on selenium have been recorded in the literature. There is some experimental and theoretical information on the monomeric selenium oxides like SeO, SeO_2, and SeO_3, but for the dimeric selenium oxides Se_2O_3 and Se_2O_3, no studies have been reported prior to this dissertation.

Some of the work presented in this dissertation involves the use of computational methods to study plausible forms of selenium oxides released into the atmosphere during high temperature combustion processes. In addition, the possible reaction pathways through which these oxides are produced are predicted. This study of both the monomeric and dimeric selenium oxides is the first of its kind. GVVPT2, B3LYP and CR-CCSD(T) methods are used to study the monomeric selenium oxides, while the dimeric selenium oxides were studied using the B3LYP and CR-CCSD(T) methods. The B3LYP method was used to obtain the optimized geometries and single point energy calculations were done on the optimized geometries using GVVPT2 and CR-CCSD(T) for the monomeric oxides and CR-CCSD(T) for the dimeric oxides.

Organization and Structure

The work presented in this dissertation is organized by molecular systems under consideration, with each major type of molecule and related species studied constituting a chapter. This introductory chapter gave an overall insight as to the reason why there was need for working on the systems studied in this dissertation. The detailed description of the theoretical electronic structure methods used is presented in Chapter II. In Chapter III, the equilibrium geometries of the ground and low-lying electronic states, adiabatic energy separations of the excited states, vertical excitation energies, and vertical emission energies of the diazirine derivative, with two CN_2 rings, i.e., C_2N_4, in both D_{2h} and C_{2v} symmetry are presented. In Chapter IV, the GVVPT2 results for the lowest-lying singlet and triplet states of the organic disjoint diradical, tetramethyleneethane, are discussed. In Chapter V, the study of the different forms of arsenic oxides released into the atmosphere during high temperature combustion processes, and the reaction pathways for their

formation, which is a challenge theoretically, are presented. In Chapter VI, results on a closely related study on the selenium oxides are presented. Chapter VII provides description of the development of closed and open shell spin-component-scaled (SCS) MP2 methods in the UNDMOL program environment. This development is expected to facilitate further studies on systems that are too large to study using CCSD and especially CCSD(T).

CHAPTER II

METHODS OF MOLECULAR ELECTRONIC STRUCTURE THEORY

Modern quantum mechanical methods can be divided into two main classes: *ab initio* electronic structure methods that optimize the wavefunction, and the density functional theory method that optimizes the electron density directly. Both categories of quantum mechanical methods are used to study systems presented in this dissertation, with the nature and size of the chemical system under investigation having determined which of these techniques was used for a particular study.

The compounds investigated in this dissertation are molecules with small energy gaps between their ground and low-lying excited electronic states. Description of such systems involves exploration of potential energy surfaces (PESs), which are complex and cannot in general be well described with the use of single reference methods. Multiconfigurational electronic structure techniques such as multiconfigurational self-consistent field (MCSCF) theory [66] and second-order generalized Van Vleck perturbation theory (GVVPT2) [67-71] are used. The multiconfigurational wave function, both at the MCSCF and GVVPT2 levels of theory, were generated through use of the macroconfigurational approach [4, 72, 73]. For the study of tetramethyleneethane diradical and the metalloid oxides, because of their size, the B3LYP DFT method was employed to calculate optimized geometrical parameters.

A description of the Hartree-Fock method, the method that provides the starting point molecular orbitals used for the more elaborate theoretical methods, begins this chapter. Then a description of second-order Møller-Plesset perturbation theory method is presented. A brief review of coupled-cluster (CC) methods is then given. This is followed by a discussion of MCSCF (including complete and incomplete model spaces) and GVVPT2 methods. In the final part of the chapter, the DFT method will be described.

The Hartree-Fock Approximation

Non-relativistic quantum electronic structure methods are developed to find approximate solutions to the non-relativistic time-independent Schrödinger equation [73, 74] (i.e., Equation 10), for a chemical system [67, 75-77].

$$\hat{H}\left|\Psi\right\rangle = E\left|\Psi\right\rangle \tag{10}$$

where $\hat{H}$ is the Hamiltonian operator, $\left|\Psi\right\rangle$ is the wavefunction and E is the energy of the system in a specific electronic state. The systems referred to in this dissertation are isolated molecules and radicals, although a molecule could in principle be part of an extended system (e.g., liquid). All the physical and chemical information, such as dipole (and multipole) moments, polarizability, etc. about a physical system can be obtained from the wavefunction, once it is constructed properly. For a molecule containing N electrons and M nuclei, the Hamiltonian operator can be written as follows

$$\mathbf{H} = -\sum_{i=1}^{N}\frac{1}{2}\nabla_i^2 - \sum_{A=1}^{M}\frac{1}{2M_A}\nabla_A^2 - \sum_{i=1}^{N}\sum_{A=1}^{M}\frac{Z_A}{r_{iA}} + \sum_{i=1}^{N}\sum_{j>i}^{N}\frac{1}{r_{ij}} + \sum_{A=1}^{M}\sum_{B>A}^{M}\frac{Z_A Z_B}{R_{AB}} \tag{11}$$

The first term in Equation (11) is the kinetic energy operator for the electrons; the second term is the kinetic energy operator for the nuclei; the third term represents the coulomb attraction between electrons and nuclei; the fourth and fifth terms represent the repulsion potential between electrons and between the nuclei respectively. Atomic nuclei are much heavier than the electrons; they tend to move much slower than the electrons surrounding them. It can then be approximated that the electrons are moving in a field of fixed nuclei. This leads to the Born-Oppenheimer Approximation [78, 79] which states that the wavefunction of the electrons can be treated separately from that of the nuclei as follows

$$\left|\Psi\right\rangle = \left|\Psi^{\text{nuc}}\right\rangle\left|\Psi^{\text{elec}}\right\rangle \tag{12}$$

with the following electronic Hamiltonian

$$\hat{\text{H}}_{\text{elec}} = -\sum_{\text{i=1}}^{\text{N}} \tfrac{1}{2}\nabla_{\text{i}}^{2} - \sum_{\text{i=1}}^{\text{N}} \sum_{\text{A=1}}^{\text{M}} \frac{\text{Z}_{\text{A}}}{\text{r}_{\text{iA}}} + \sum_{\text{i=1}}^{\text{N}} \sum_{\text{j>i}}^{\text{N}} \frac{1}{\text{r}_{\text{ij}}} \tag{13}$$

In a compact manner, the electronic Hamiltonian can be written as

$$\hat{\text{H}}_{\text{elec}} = \sum_{\text{i=1}}^{\text{N}} \hat{\text{T}}_{\text{i}}^{\text{elec}} + \sum_{\text{I=1}}^{\text{M}} \sum_{\text{i}}^{\text{N}} \hat{\text{V}}_{\text{I,i}}^{\text{nuc,elec}} + \sum_{\text{i=1}}^{\text{N}} \sum_{\text{j>i}}^{\text{N}} \hat{\text{V}}_{\text{i,j}}^{\text{elec,elec}} \tag{14}$$

where $\hat{\text{T}}$ is the kinetic energy operator, and $\hat{\text{V}}$ is the potential energy operator; superscripts *nuc* and *elec* indicate nuclei and electrons respectively. The electronic Schrödinger equation is then written as

$$\left[\sum_{\text{i=1}}^{\text{N}} \hat{\text{T}}_{\text{i}}^{\text{elec}} + \sum_{\text{I=1}}^{\text{M}} \sum_{\text{i}}^{\text{N}} \hat{\text{V}}_{\text{I,i}}^{\text{nuc,elec}} + \sum_{\text{i=1}}^{\text{N}} \sum_{\text{j>i}}^{\text{N}} \hat{\text{V}}_{\text{i,j}}^{\text{elec,elec}}\right]\left|\Psi^{\text{elec}}\right\rangle = \text{E}_{\text{elec}}\left|\Psi^{\text{elec}}\right\rangle \tag{15}$$

Solving for E_{elec} for various nuclear geometries produces the potential energy surface (PES) for the nuclei, from which important information about the system can be obtained (such as the equilibrium geometries and vibrational frequencies).

The solution for a one electron system, like the hydrogen atom, can be calculated exactly. The Hartree-Fock theory assumes that in a many electron system, each electron is experiencing an average or mean electric field from all other electrons and nuclei. E.g. the H^- ion with two electrons is solved by neglecting instantaneous interactions, which leads to a separable Hamiltonian and the total electronic wavefunction describing the motion of the two electrons, $\Psi(r_1, r_2)$, would just be the product of two one-electron wavefunctions (orbitals), $\Psi_H(r_1)\Psi_H(r_2)$. For more electrons, a general product wavefunction would be

$$\Psi_{HF}(r_1, r_2, r_3 ....., r_N) = \phi_1(r_1)\phi_2(r_2)\phi_3(r_3).....\phi_N(r_N) \quad (16)$$

But this function does not satisfy the antisymmetry principle, which states that a wave function of fermions must be antisymmetric with respect to the interchange of any set of spin space coordinates X = {r, ω}, with ω representing the generic spin coordinates (α or β) and r representing the three spatial degrees of freedom. Including spin degrees of freedom, products of orbitals change from the spatial orbital form, $\phi(r)$, to the spin orbital form, $\chi(x)$,

$$\Psi_{HF}(x_1, x_2, x_3 ....., x_N) = \chi_i(x_1)\chi_j(x_2)\chi_k(x_3).....\chi_N(x_N) \quad (17)$$

For Eq. 17 to satisfy the antisymmetry principle, a determinant of spin orbitals, called a Slater determinant, must be constructed. For N electrons, the determinant is written as follows,

$$\Psi = \frac{1}{\sqrt{N!}} \begin{vmatrix} \chi_i(x_1)\chi_j(x_1)\cdots\chi_N(x_1) \\ \chi_i(x_2)\chi_j(x_2)\cdots\chi_N(x_2) \\ \vdots \quad \vdots \quad \ddots \quad \vdots \\ \chi_i(x_N)\chi_j(x_N)\cdots\chi_N(x_N) \end{vmatrix} \tag{18}$$

The factor $(N!)^{-1/2}$ is the normalization factor. N electrons are occupying N spin orbitals ($\chi_i, \chi_j, \ldots, \chi_k$) without specification of which electron occupies a particular orbital. Since the rows of the determinant are labeled by the electrons and the columns are labeled by the spin orbitals, interchanging two rows corresponds to interchanging the coordinates of two electrons. This changes the sign of the determinant, resulting in the Slater determinant meeting the requirement of the antisymmetry principle (i.e., Pauli exclusion principle). If two electrons with the same spin occupy the same spin orbital, this will correspond to having two columns of the determinant equal, causing the determinant to equal zero.

The Hartree-Fock wavefunction for a two electron particle is thus

$$\Psi(x_1, x_2) = \frac{1}{\sqrt{2}}\left[\chi_i(x_1)\chi_j(x_2) - \chi_i(x_2)\chi_j(x_1)\right] \tag{19}$$

The Hamiltonian can be divided into a term containing only one-electron terms,

$$h(i) = -\frac{1}{2}\nabla_i^2 - \sum_A \frac{Z_A}{r_{iA}}, \tag{20}$$

and the two electron operator $\nu(i,j)$,

$$\nu(i,j) = \frac{1}{r_{ij}} \tag{21}$$

So that electronic Hamiltonian can be written as

$$\hat{H}_{elec} = \sum_{i} h(i) + \sum_{i>j} \nu(i,j) + V_{NN} \tag{22}$$

with V_{NN} being just a constant for a fixed set of nuclear coordinates {R}.

The Hartree-Fock energy can be calculated as follows, assuming that the wavefunction is normalized

$$E_{HF} = \langle \Psi_{HF} | \hat{H}_{elec} | \Psi_{HF} \rangle \tag{23}$$

The variational theorem, which states that the energy of an approximate wavefunction is always an upper bound of the true energy, is then employed. Beginning with some initial guess of one electron wavefunctions (e.g., by ignoring the interactions between electrons), the guess orbitals will be refined iteratively, using the mean field of all other electrons. Because of this approach, Hartree-Fock is called a Self-Consistent method. The best approximate spin-orbital is that which by varying the parameters minimizes the electronic energy E_{elec} within the functional space, leading to the correct molecular orbitals. This functional space is large and leads to marginal improvements with substantial computational effort. Instead, the molecular orbitals are obtained as a linear combination of a set of basis functions (called "atomic orbital" basis functions, which are usually atom-centered Gaussian type functions),

$$\Psi_\alpha = \sum_{\mu=1} C_{\mu i} \phi_\mu \tag{24}$$

In Eq. (24), Ψ_α are the optimized, or molecular, orbitals, and ϕ_μ is the set of basis functions or atomic orbitals. Lagrange's method of undetermined multipliers is the mathematical method used in the HF approximation to calculate the molecular orbitals. In a situation where the basis set functions (atomic orbitals) are not orthonormal as is usual, the molecular orbital coefficient C can be obtained by solving the generalized eigenvalue problem involving the Fock matrix,

$$FC = SC\varepsilon \tag{25}$$

where ε are the Lagrange multipliers. S is the overlap matrix of the basis set functions

$$S_{\mu\nu} = \langle \phi_\mu | \phi_\nu \rangle \tag{26}$$

The Fock operator $\hat{f}_i$ (one electron Hamiltonian operator) in the one electron approximation is related to the orbitals

$$\hat{f}_i = -\tfrac{1}{2}\nabla_i^2 - \sum_{A=1}^{M} \frac{Z_A}{r_{iA}} + v^{HF}(i) \tag{27}$$

because $v^{HF}(i)$ is the average potential experienced by the ith electron due to the presence of the other electrons. As stated earlier, $h(i) = -\tfrac{1}{2}\nabla_i^2 - \sum_{A=1}^{M} \frac{Z_A}{r_{iA}}$ is the kinetic and potential energy of attraction to the nuclei of the ith electron. The eigenvalue can be computed as follows,

$$\hat{f}_i \left| \Psi_i \right\rangle = \sum_{\mu} \varepsilon_{\mu i} \left| \Psi_\mu \right\rangle \tag{28}$$

where $\varepsilon_{\mu i}$ is the Lagrange multiplier, which is equivalent to the Fock matrix element in the HF approximation

$$\varepsilon_{\mu i} = \left\langle \Psi_\mu \left| \hat{f}_i \right| \Psi_i \right\rangle \tag{29}$$

The diagonalization steps are repeated iteratively until C converges, the Fock matrix also depends on C through construction of V^{HF}. Since the HF determinant is invariant with respect to unitary transformation of occupied spin orbitals (those included in the determinant), the resulting molecular orbitals obtained from Eq. 25 can be brought to canonical form and Eq. 28 transformed to

$$\hat{f}_i \left| \Psi_i \right\rangle = \varepsilon_i \left| \Psi_i \right\rangle \tag{30}$$

in which ε_i are orbital energies.

In the restricted Hartree-Fock (RHF) approximation, the same set of spatial orbitals is used to describe two electrons with opposite spins (α and β). In Restricted Open-shell Hartree-Fock (ROHF), the doubly occupied orbitals are described using the same set of spatial orbitals, similar to RHF. For unrestricted Hartree-Fock (UHF), two sets of spatial orbitals are used, one for spin-up and the other for spin-down. Clearly, only ROHF and UHF can be used for open shell cases.

Møller-Plesset Perturbation (MP2) Theory

Second-order many-body perturbation theory [also known as Møller-Plesset perturbation theory (MP2)] is the simplest and least expensive *ab initio* electronic

structure method for including electron correlation [69, 80]. This method is not variational (i.e., it does not give an upper bound of the exact energy), but it is size consistent. In this method, the total Hamiltonian of the system is divided into two parts: a zero order part, H_0, is the Hartree-Fock Hamiltonian which has known eigenfunctions and eigenvalues, and a perturbation V.

The Hamiltonian is partitioned as follows

$$H = H_0 + V \tag{31}$$

where H_0 is

$$H_0 = \sum_i h(i) + \sum_i \nu^{HF}(i) \tag{32}$$

and the perturbation V, is

$$\mathbf{V} = \sum_{\mathbf{i<j}} \mathbf{r_{ij}^{-1}} - \sum \boldsymbol{\nu}^{\mathbf{HF}}\mathbf{(i)} \tag{33}$$

where $\nu^{HF}(i)$ stands for the Coulomb and exchange interactions of the ith electron with the other electrons in the Hartree-Fock sense. From the expression for the Hartree-Fock energy, one can see that

$$\nu^{HF}\chi_i(i) = \sum_j \int dx_2 \frac{\left|\chi_j(x_2)\right|^2}{r_{12}}\chi_i(x_1) - \sum_j \int dx_2 \frac{\chi_j^*(x_2)\chi_i(x_2)}{r_{12}}\chi_j(x_1) \tag{34}$$

$$= \sum_j \left[j\left| r_{12}^{-1} \right| j\right]\chi_i(x_1) - \sum_j \left[j\left| r_{12}^{-1} \right| i\right]\chi_j(x_1) \tag{35}$$

The expectation value of ν^{HF} for orbital i can be found to be

$$\left[i\left|v^{HF}\right|i\right]=\sum_j\left[ii\left|jj\right]-\left[ij\right|ji\right] \tag{36}$$

The Hartree-Fock Slater determinant, $\left|\Psi_0^{(0)}\right\rangle$, is an eigenfunction of H_0, therefore,

$$H_0\left|\Psi_0^{(0)}\right\rangle = E_0^{(0)}\left|\Psi_0^{(0)}\right\rangle \tag{37}$$

having eigenvalues

$$E_0^{(0)}=\sum_i \varepsilon_i \tag{38}$$

where, ε_i, is the orbital energy for the ith electron. Note that the zero-order energy is different than the Hartree-Fock energy of the system because the Hartree-Fock Hamiltonian is the exact Hamiltonian.

The first order correction to the energy is as follows

$$E_0^{(1)}=\left\langle\Psi_0\left|V\right|\Psi_0\right\rangle \tag{39}$$

$$=\left\langle\Psi_0\left|\sum_{i<j} r_{ij}^{-1}\right|\Psi_0\right\rangle-\left\langle\Psi_0\left|\sum_i v^{HF}(i)\right|\Psi_0\right\rangle \tag{40}$$

$$=\frac{1}{2}\sum_i\sum_j\left(\left[ii|jj\right]-\left[ij|ji\right]\right)-\sum_i\left[i\left|v^{HF}\right|j\right] \tag{41}$$

$$=-\frac{1}{2}\sum_i\sum_j\left[ii|jj\right]-\left[ij|ji\right] \tag{42}$$

Eq. 38 gives the zero-order energy and Eq. 42 gives the first-order correction to the energy; these can be summed to give the Hartree-Fock energy

$$E_0^{HF} = E_0^{(0)} + E_0^{(1)}$$

$$= \sum_i \varepsilon_i - \frac{1}{2}\sum_i \sum_j \left[ii \middle| jj\right] - \left[ij \middle| ji\right] \tag{43}$$

The above results show that to obtain correlation energy there is need to go to second order or higher.

Second order energy correction is as follows

$$E_0^{(2)} = \sum_n \frac{\left|\left\langle \Psi_0 \middle| V \middle| \Psi_n \right\rangle\right|^2}{E_0^{(0)} - E_n^{(0)}} \tag{44}$$

$\left\langle \Psi_n \right|$ is a Slater determinant corresponding to an electron configuration that is excited relative to the HF reference and will have higher energy. But determinants for single, triple and higher order excitations do not contribute to the second order correction $E_0^{(2)}$, e.g., for a single excitation

$$\left\langle \Psi_0 \middle| V \middle| \Psi_i^a \right\rangle = 0 \tag{45}$$

Only a double excitation determinant, $\left|\Psi_{ij}^{ab}\right\rangle$, can give a non-zero contribution

$$\left\langle \Psi_0 \middle| \sum_{i<j} r_{ij}^{-1} \middle| \Psi_{ij}^{ab} \right\rangle = \left[ia \middle| jb\right] - \left[ib \middle| ja\right] \tag{46}$$

resulting in the following energy eigenvalue, $E_0^{(0)} - \varepsilon_i - \varepsilon_j + \varepsilon_a + \varepsilon_b$, that is

$$H_0 \left|\psi_{ij}^{ab}\right\rangle = \left(E_0^{(0)} - \varepsilon_i - \varepsilon_j + \varepsilon_a + \varepsilon_b\right) \left|\Psi_{ij}^{ab}\right\rangle \tag{47}$$

This results in the following second order energy correction

$$E_0^{(2)} = \sum_{i<j} \sum_{a<b} \frac{\left|\left\langle \Psi_0 \left| \sum_{i<j} r_{ij}^{-1} \right| \Psi_{ij}^{ab} \right\rangle\right|^2}{\varepsilon_i + \varepsilon_j - \varepsilon_a - \varepsilon_b} \tag{48}$$

$$= \sum_{i<j} \sum_{a<b} \frac{\left|\left[ia|jb\right] - \left[ib|ja\right]\right|^2}{\varepsilon_i + \varepsilon_j - \varepsilon_a - \varepsilon_b} \tag{49}$$

The second-order energy can be expressed as a sum over contributions from each pair of electrons in occupied orbitals

$$E_0^{(2)} = \sum_{i<j} e_{ij} \tag{50}$$

and the contribution from each pair involves a sum over pairs of virtual orbitals

$$e_{ij} = \sum_{a<b} \frac{\left|\left[ia|jb\right] - \left[ib|ja\right]\right|^2}{\varepsilon_i + \varepsilon_j - \varepsilon_a - \varepsilon_b} \tag{51}$$

The MP2 energy can therefore be written as shown below

$$E_0^{MP2} = E_0^{(0)} + E_0^{(1)} + E_0^{(2)} \tag{52}$$

$$E_0^{MP2} = E^{(HF)} + E_0^{(2)} \tag{53}$$

Coupled Cluster Theory (CC)

Coupled Cluster methods are one of the most accurate high-level theoretical means of accounting for the correlation energy with HF functioning as a reference [50, 81]. This method was introduced in quantum chemistry by Cizek [4, 82, 83]. The CC theory is not variational but it is size consistent. Substituted configurations are introduced in the wavefunction in CC methods in an exponential manner rather than

additively, as is the case of CI. It is assumed that the exact wave function, Ψ, has a non-zero projection on the reference HF state. The ground-state wave function in a single reference CC theory for an N-electron system is represented as follows:

$$\left|\Psi\right\rangle = e^{T}\left|\phi\right\rangle \tag{53}$$

where $\left|\Psi\right\rangle$ is the exact wavefunction, T is the coupled cluster excitation operator, and $\left|\phi\right\rangle$ is the reference wavefunction (i.e., single determinant, usually Hartree-Fock). The excitation operator can be written as a linear combination of single, double, triple, and up to N excitations for an N electron system as follows

$$T = T_1 + T_2 + T_3 + \ldots\ldots\ldots\ldots\ldots T_N \tag{54}$$

The single and double excitation operators can be defined as

$$T_1 = \sum_{i}^{occ} \sum_{a}^{virt} t_i^a E_i^a \tag{55}$$

$$T_2 = \sum_{i>j}^{occ} \sum_{a>b}^{virt} t_{ij}^{ab} E_{ij}^{ab} \tag{56}$$

where E_i^a, E_{ij}^{ab}, etc., are orbital excitation operators, and t_i^a, t_{ij}^{ab}, are cluster amplitudes to be determined in order to construct the coupled cluster wavefunction.

The orbital excitation operators are given by

$$E_i^a = X^{a\alpha} X_{i\alpha} + X^{a\beta} X_{i\beta} \tag{57}$$

$$E_{ij}^{ab} = E_i^a E_j^b \tag{58}$$

where $X^{a\alpha}$ and $X_{i\alpha}$ are creation and annihilation operators, respectively, and σ stands for spin-up (α) or spin-down (β) eigenfunctions for a particle with spin $\frac{1}{2}$. For example,

$$\left|\phi_i^a\right\rangle = E_i^a\left|\phi\right\rangle, \tag{59}$$

$$\left|\phi_{ij}^{ab}\right\rangle = E_{ij}^{ab}\left|\phi\right\rangle. \tag{60}$$

The exponential operator is defined by the following expansion

$$e^T = \sum_{N=0}^{\infty}\frac{T^N}{N!} = 1 + T + \frac{1}{2}T^2 + \frac{1}{3!}T^3 + ... \tag{61}$$

and thus

$$e^T = 1 + (T_1 + T_2 + T_3 + ...) + (T_1 + T_2 + T_3 + ...)^2 + (T_1 + T_2 + T_3 + ...)^3 + ... \tag{62}$$

The CC chain of equations used for the cluster amplitudes is obtained by projecting the connected-cluster form of the electronic Schrödinger equation, (i.e., Eq. 53),

$$\left(H_N e^T\right)_C\left|\phi\right\rangle = \Delta E\left|\phi\right\rangle \tag{63}$$

onto the excited configurations generated by T, where $H_N = H - \langle\phi|H|\phi\rangle$ is the electronic Hamiltonian, and $\Delta E = E - \langle\phi|H|\phi\rangle$ is the correlation energy when $|\phi\rangle$ is the Hartree-Fock determinant and subscript C indicates the connected part of a given expression.

Recalling Eqs. (59) and (60)

$$\left|\phi_i^a\right\rangle = E_i^a\left|\phi\right\rangle, \tag{64}$$

$$\left|\phi_{ij}^{ab}\right\rangle = E_{ij}^{ab}\left|\phi\right\rangle, \ldots\ldots \tag{65}$$

the equations determining the cluster operators are obtained from

$$\left\langle\phi_i^a\left|e^{-T}H_N e^T\right|\phi\right\rangle = 0, \tag{66}$$

$$\left\langle\phi_{ij}^{ab}\left|e^{-T}H_N e^T\right|\phi\right\rangle = 0, \tag{67}$$

when T is restricted to singly and doubly excited clusters. The CC approximation that results is CCSD [68, 84], and the correlation energy will be determined by T_1 and T_2 amplitudes as follows,

$$\Delta E_{CCSD} = \left\langle\phi\left|H_N\left(T_1 + T_2 + \frac{1}{2}T_1^2\right)_C\right|\phi\right\rangle \tag{68}$$

Despite the accuracy of CCSD for system that are qualitatively well-described by a single Slater determinant, it has however proven to be insufficient for the description of systems that are multiconfigurational in nature. Truncating T to singly, doubly, and triply excited clusters (i.e., $T = T_1 + T_2 + T_3$) results in the CCSDT approximation. The inclusion of the triple excitations has proven to be very expensive and almost impractical; to go around this difficulty, different approximations have been developed. In CCSD(T) the triple excitation is included perturbatively (i.e., treated noniteratively) [73, 85, 86] . The CCSD(T) method has been quite effective and accurate in systems in which CCSD is applicable, but in systems that involve bond breaking CCSD(T) is inadequate. In the CR-CCSD(T) [87] method, complete renormalization, including the triple (T) corrections, is

performed. This method has improved the description of bond breaking, while retaining the single reference description. CCSD(T) is inadequate to study excited states of systems when a suitable single determinant reference does not exist. As a remedy, the equation of motion EOM-CCSD(T) extension is used for the calculation of excited states [24, 25] .

The quadratic configuration interaction with singles and doubles (QCISD) method is an intermediate method between configuration interaction and coupled cluster theory developed by Pople et al. [25, 88-90]. This method was used in this present work, and gives results often approximately equal to that of CCSD at a lower cost.

Multiconfigurational Self-Consistent Field (MCSCF) Theory

The equilibrium geometries of molecules, including the structures of reactants and products, often may be described reasonably well by single-reference wavefunction methods. For such cases, Hartree-Fock is a good zero-order approximation, on which correlation energy can be efficiently and accurately calculated by the use of such single-reference methods as, many-body perturbation theory(MBPT) [i.e., Møller-Plesset perturbation theory(MP2)] [24, 91], and the coupled cluster methods [92, 93]. However, chemistry involves much more than that; it involves the formation and breaking of bonds and the excitation of atoms or molecules into excited electronic states. In such cases, the Hartree-Fock determinant does not dominate the wavefunction, and sometimes can just be one of a number of important electronic configurations (i.e., different arrangements of electrons) that ought to be included in the description of the wavefunction. An example of a system where the use of a Hartree-Fock wavefunction as a reference fails even for the ground state is that of diradicals, because they usually have low-lying unoccupied

orbitals and hence low-lying excited electronic states. Trimethylenemethane (TMM) is one of such diradicals. TMM has four π electrons that can be distributed over four π type orbitals in different ways as shown below in Figure 5, having the following energy diagram as shown in Figure 6.

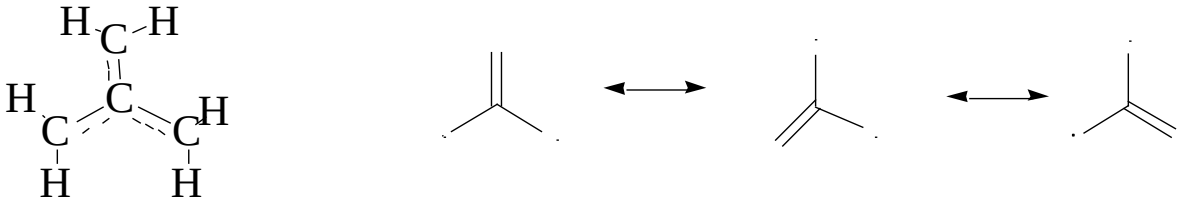

Figure 5. Isomerization of trimethyleethane diradical [94].

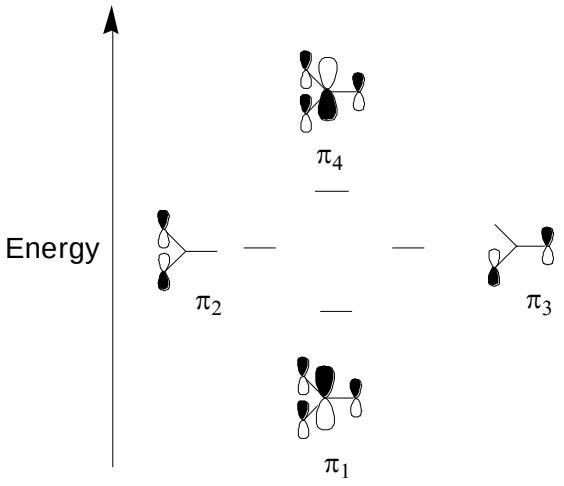

Figure 6. Energy diagram for trimethylenemethane [17, 94].

Therefore a qualitatively correct zero order description of TMM or other such diradicals will need to be a multiconfigurational model, such as provided by the

multiconfigurational self-consistent field (MCSCF) [95, 96] method. The general form of a MCSCF wavefunction can written as

$$\left|\Psi_{\mathrm{MCSCF}}\right\rangle = \sum_{\mathrm{I}} \mathrm{A}_{\mathrm{I}} \left|\Phi_{\mathrm{I}}\right\rangle \tag{69}$$

$$\Phi_{\mathrm{I}} = \mathrm{A}\left\{\prod_{\mathrm{i}\subset\mathrm{I}} \phi_{\mathrm{i}}\right\} \tag{70}$$

$$\phi_{\mathrm{i}} = \sum_{\mu} \chi_{\mu} \mathrm{C}_{\mu\mathrm{i}} \tag{71}$$

$\left|\Psi_{\mathrm{MCSCF}}\right\rangle$ is a linear combination of several configuration state functions (CSFs), Φ_{I} that are generated from one or more configurations. The different arrangements of electrons in the molecular orbitals, ϕ_{i}, differentiate one configuration from the other. In MCSCF the configuration mixing coefficients A_{K} and the MO expansion coefficients $\mathrm{C}_{\mu\mathrm{i}}$ are optimized variationally. For the configuration interaction (CI) method, only the configuration mixing coefficients A_{K} are optimized. Full optimized reaction space (FORS) [96] or a complete active space SCF (CASSCF) [97] is a MCSCF wavefunction in which the active electrons are rearranged in all possible ways among the active orbitals. This is a Full CI type of wavefunction in the valence space.

The drawback with the CASSCF method is that too many configurations to be computationally feasible are often generated. To solve this problem, the restricted active space SCF (RASSCF) [92, 98] and the quasi-complete active space SCF (QCAS-SCF) [99] methods were developed. These methods are designed in such a way that the orbitals in the model space are divided into three categories: orbitals with limited number

of electrons, a fully active orbital set, and orbitals with limited number of vacancies. In this work, a more flexible alternative, the macroconfigurational approach [95] developed by Prof. Hoffmann's group, has been used. Since the MCSCF wavefunction is an analog of the Hartree-Fock wave function for systems without a simple one-configuration description, accurate energies for the system can be acquired only by the inclusion of correlation corrections.

Macroconfiguration Approach

The macroconfiguration approach is a technique developed by Prof. Hoffmann's research group to construct physical, reasonable, compact model spaces. This approach results in significant improvement of computational methods like MCSCF and multireference correlated methods used in describing dynamic correlation effects. The issue of constructing truncated configuration spaces, with the right choice of reference configurations, which describe the nondynamic part of the correlation energy correctly and provide adequate references for use in obtaining a good description of dynamic correlation, is addressed. Even though full exploitation of the concept of macroconfigurations is relatively recent [92, 99], some ideas were already used in the restricted active space SCF (RASSCF) [100, 101] method, the restricted configuration interaction (RCI) [102] method and in the quasicomplete active space (QCAS-SCF) method. In CASSCF, the set of orbitals are divided into groups of Core (C), active (A), and virtual (V) orbitals. It has only one macroconfiguration: $C^{2d_C} A^{N} V^{0}$, where d_C is the number of closed shell (or core) orbitals and N is the number of active electrons. RASSCF, in addition, partitions active orbitals into three groups (A_1, A_2, A_3) and a subset of macroconfigurations $C^{2N_C} A_1^{N_1} A_2^{N_2} A_3^{N_3} V^{0} \left(N_1 + N_2 + N_3 = N \right)$, is used to describe it.

In the QCAS-SCF method, there is the possibility of using one fixed macroconfiguration with an arbitrary number of groups. In contrast, the macroconfiguration approach supports an arbitrary number of macroconfigurations.

In general, consider a fixed partitioning, N = (N_1, N_2, ……,N_g) of N electrons in g disjoint orbital groups {G_1, G_2, …….G_g}; a macroconfiguration is

$$æ(N): G_1^{N_1} G_2^{N_{21}} \cdots G_g^{N_g} \tag{72}$$

A macroconfiguration specifies occupation numbers of fixed groups, unlike conventional electron configurations that give the occupancies of separate orbitals. The group (N_1, N_2, ……,N_g) occupation numbers must obey the following restrictions

$$0 \le N_t \le 2d_t \; t \in [1, g], \tag{73}$$

$$N_1 + N_2 + \cdots + N_g = N, \tag{74}$$

where d_t is the number of orbitals in group N_t ($t \in [1, g]$) and N is the number of active electrons. A CAS model space is created when g = 1, giving the single macroconfiguration $C^{2N_C} A_1^{N_1} A_2^{N_2} \cdots A_g^{N_g} V^0$ and a RAS-type model space is obtained when g = 3, etc. In principle, a model space that includes all desired reference configurations can be obtained.

Through the following inequalities,

$$1 \le N_V \le 2, \tag{75}$$

$$\mathrm{Max}\left(0, N_t^0 - 2\right) \le N_t \le N_t^0, t \in [1, g], \tag{76}$$

$$N_1 + N_2 + \ldots + N_g + N_V = N \tag{77}$$

the group occupancies of all external macroconfigurations, $æ_{ext}(n, n_v) = C^{2N_C} A_1^{N_1} A_2^{N_2} \cdots A_g^{N_g} V^{N_V}$, excited relative to a given model macroconfiguration $æ_{mod}(n^0) = C^{2N_C} A_1^{N_1} A_2^{N_2} \cdots A_g^{N_g^0} V^0$, through single and double excitations into the virtual orbitals can be obtained. MCSCF-type schemes based on macroconfiguration descriptions of configuration spaces can guarantee the equitable treatment of correlation effects for all the states considered. The set of configurations in the model and external spaces can be generated independently, since they are created by disjoint sets of configurations and their configuration structure proves to be quite regular. The model and external spaces are direct sums of the spaces of the included model and external macroconfigurations, and the configuration space of each macroconfiguration is a direct sum of its configurations. Duplication in the list of external macroconfigurations is avoided by comparing generated configurations with previously generated ones. This technique, originally suggested by Panin and Simon of generating excited macroconfigurations, is computationally effective, and is also flexible in the fact that any desired additional restrictions on occupancies of separate (active and/or virtual) groups in external macroconfigurations is allowed. In the GVVPT2 program and other multireference techniques, macroconfigurations allow one to: (1) use effectively physical considerations in constructing compact model spaces and in generating external spaces; (2) eliminate the need of storage of large lists of external configurations and to efficiently generate the desired subsets of such configurations during calculations; and (3) omit effectively

Hamiltonian matrix blocks corresponding to noninteracting macroconfiguration pairs, which can decrease drastically the number of configurations pairs that must be explicitly calculated.

Second-Order Generalized Van Vleck Perturbation Theory (GVVPT2)

In an attempt to recover dynamic electron correlation energy, with the use of multiconfiguration self-consistent field (MCSCF) wavefunction as the zeroth-ordered wavefunction, many methods can be applied. The Multi-reference Configuration Interaction including Single and Double excitations (MRCISD) method is effective, but computationally is often too costly, since it scales as $\sim n^6$. Thus MRCISD is good for studying systems with three or four atoms (when entire potential energy surfaces are needed). Multi-reference (MRPT) and quasidegenerate (QDPT) perturbation theories, which scale as $\sim n^5$, are alternate methods that have been found to be computationally efficient for the description of dynamic electron correlation in molecules, but they are plagued with some drawbacks, notably the "intruder state" problem. It is a situation where the energy of the perturber is comparable to that of the zeroth-order wavefunction, resulting in a nearly zero denominator in the perturbative correction, causing divergent behavior in the PES curve. Recently, much progress has been made in order to resolve this problem [5, 103, 104], Moreover, as shown by Roos et al. [103], useful chemical information can still be obtained from potential energy surfaces that have localized singularities. The general applicability of the MRPT and QDPT methods has been limited because of the presence of "intruder states" and their removal by complex methods.

To circumvent the limitations observed in the MRPT and QDPT methods, a subspace-selective method, GVVPT2, was developed by the Hoffmann group. In the GVVPT2 method, a reference space (L) which contains an expansion of the set of target wavefunctions $\left|\Psi_p\right\rangle = \left|\psi_1, \psi_2, \ldots, \psi_{N_p}\right\rangle$ of the N_p - lowest electronic states, is partitioned into the "model" (or MCSCF) space L_M (dim $L_M > N_P$) and an "external" space, L_Q. The L_M space and the L_Q space are connected through electron excitations. In the model space, L_M, the reference functions $\{\Phi_P\}_{P=1}^{N_P}$ are generated, which constitute the subspace called the "primary" subspace (L_P), while its orthogonal complement is the "secondary" subspace (L_S): $L_P \oplus L_S = L_M$. A physically reasonable selected MCSCF model space will generate external configurations that can be expected to be energetically well separated from the lowest MCSCF states of interest (i.e., the L_P space), and have only a perturbative effect on this primary subspace. There is some uncertainty of partitioning the model space into an unrelaxed primary subspace L_P and it complement space L_S. This ambiguity is removed with the use of self-consistent quasidegenerate perturbation theory (SC-QDPT) [105]. However, it has been shown that there is a possibility of omitting primary space relaxation when a primary space that consists of all low-lying potentially quasidegenerate states is used. Moreover, GVVPT2 completely avoids the problem of possible quasidegeneracy between the secondary and external subspaces [105-107].

Considering the block-diagonal part of the Hamiltonian matrix in the $L_P \oplus L_Q$ space as the unperturbed Hamiltonian (H_0 = PHP + QHQ) and its off-diagonal block (V = PHP + QHP) as the perturbation, the P-Q interactions are taken into account first-order in

the wavefunction. Within the model space, the second-order perturbatively corrected Hamiltonian matrix is as follows [1]

$$H_{PP}^{eff} = H_{PP} + \tfrac{1}{2}\left(H_{PQ}Z_{QP} + Z_{QP}^{+}H_{QP}\right), \tag{78}$$

$$H_{SP}^{eff} = H_{SQ}Z_{QP}, \tag{79}$$

$$H_{SS}^{eff} = H_{SS}, \tag{80}$$

where contributions from the external CSFs to the final wavefunction are determined by the elements of anti-Hermitian matrix Z_{QP} (the P-Q rotational parameters). The system of linear equations below is used to determine the rotational parameters

$$\left(H_{QQ} - E_0^P\right)Z_{QP} = -H_{QP}, \tag{81}$$

where P is the primary space, and $\left\{ E_0^P = \left\langle \Phi_P \middle| H \middle| \Phi_P \right\rangle \right\}_{P=1}^{N_P}$ are the energies of the reference states (i.e., MCSCF energies within the L_M space). However, these second-order QDPT basic equations are block-diagonal and scale as n^6 and so are further approximated in the GVVPT2 method. The QDPT method allows the effects of the secondary states on the perturbed primary ones (through the $H_{SP}^{eff} = H_{SQ}Z_{QP}$, term), which is not the case with widely used multireference second-order perturbation theories such as the CASPT2 method developed by Roos et al. [108], MRPT2 by Murphy and Messmer [109], and MCQDPT by Hirao and Nakano [110]. Such effects are usually small but they can be important [1]. In the realization of the GVVPT2 method, the off-diagonal matrix elements are discarded and the required diagonal elements of the matrices $(H_{QQ} - E_0^P)$

[of Eq. (81)] are approximated beginning with the conventional, Møller-Plesset-type, one-electron Hamiltonians, $(H_{qq} - E_0^P) \approx \varepsilon_q^P - \varepsilon_0^P$ [5, 111]. To some extent this approximation proves to work well, but sometimes the "intruder state" problem occurs [112] , where the $\varepsilon_q^P - \varepsilon_0^P$ differences are small or even negative. In the present version of the GVVPT2 method developed by Hoffmann and coworkers [1], the "intruder state" problem was fixed by a theoretically well-justified formula for nonlinear responses to P-Q perturbations. Namely, a stabilized perturbation theory [1] is used to calculate the rotational parameter Z_{qp}

$$Z_{qp} = -\frac{\tanh\left(\varepsilon_{m_e}^p - \tilde{E}_{0,m_e}^p\right)}{\varepsilon_{m_e}^p - \tilde{E}_{0,m_e}^p} H_{qp} \tag{82}$$

where E_{0,m_e}^P is the degeneracy-corrected zero-order energy of the p-th primary state. This incorporates degeneracy corrections and allows for the effects of all external CSFs that are created by a given external configuration $\mathbf{m_e}$, which have degenerate energy $\varepsilon_{m_e}^p$,

$$\tilde{E}_{0,m_e}^p = \tfrac{1}{2}\left(\varepsilon_{m_e}^p + \varepsilon_0^p\right) - \tfrac{1}{2}\sqrt{\left(\varepsilon_{m_e}^p + \varepsilon_0^p\right)^2 + 4\sum_{q \in m_e} H_{qp}^2}\,. \tag{83}$$

The new Z_{qp} parameters are continuous for all regions of the potential energy curves (i.e., for all $\varepsilon_q^p - \varepsilon_0^p$ energy differences). In the $\varepsilon_{m_e}^p >> \varepsilon_0^p$ main region, Eqs. (82) and (83) reduce to the same result as the conventional theory, while, in the $\varepsilon_{m_e}^p \le \varepsilon_0^p$ region, they lead to small rotational parameters and small negative contributions of intruder states to the correction energy of a specific primary state. This version of the GVVPT2 program has been used in all the calculations reported in this dissertation. The revised GVVPT2

[1] method results in smooth potential energy surfaces even when the surfaces are in close proximity.

The main challenge in the use of a multireference method like GVVPT2 is that of constructing a well-balanced model space. The macroconfiguration technique can help in overcoming this problem.

Density Functional Theory (DFT)

Density functional theory (DFT), since being adopted by quantum chemists, has been very widely used for simulating ground state energy surfaces in molecules. Density functional theory (DFT) uses directly the electron density to describe N-electron systems, unlike the *ab initio* wavefunction methods described earlier which use complicated many-body expansions as the means for describing N-electron systems. The idea of DFT was originated in 1927 by Thomas and Fermi [113, 114] who came up with an approximate potential energy of a system, which is composed of classical (coulomb) and non-classical (exchange-correlation) components, in terms of a classical component alone and then computing the kinetic energy using a non-interacting electron gas. The Thomas-Femi (TF) model was improved on in 1930 by Dirac [115], who introduced a formula for the exchange-energy of a uniform electron gas, leading to what became known as the Thomas-Femi-Dirac (TFD) model. These models were not sufficiently accurate for predicting molecular binding, therefore making them practically far from being chemically useful [116]. A major breakthrough in DFT was reached when Hohenberg and Kohn [117] used a functional of the total electron density of a system to come up with an exact expression for the ground state electronic energy of an atom or molecule.

$$E[\rho] = T[\rho] + V_{ne}[\rho] + V_{ee}[\rho]$$

$$= T[\rho] + \int \rho(r)dr + J[\rho] + E_{xc}[\rho] \qquad (84)$$

This reduced the many-body problem of N electrons from 3N spatial coordinates to 3 spatial coordinates. Eq. 84 is subject to the condition that $\int \rho(r)dr = N$, where N is the total number of electrons in the system, $T[\rho]$ is the kinetic energy functional, $J[\rho]$ is the classical (coulomb) repulsion energy and $E_{xc}[\rho]$ is the exchange-correlation energy functional. The above expression is exact and can be applied to any system, but lacks definite formulas to obtain the various quantities.

In 1965 the Kohn-Sham method [118] came into existence when Kohn and Sham made a major advance in developing an indirect approach to obtain the $T[\rho]$ functional. This achievement led to a major change in the field of DFT and turned it into a practical tool for serious calculations. The idea that Kohn and Sham had was to develop simple formulas for a fictitious system of non-interacting electrons, to use in obtaining the exact kinetic energy functional through molecular orbitals for such systems. Furthermore they redefined the $E_{xc}[\rho]$ term to account for the difference between the kinetic energy of the fictitious and that of the real system, in addition to considering the nonclassical part of the electron-electron repulsion term. The effective external potential $\nu_{eff}(r)$ experienced by the system of non-interacting electrons is given by

$$\nu_{eff}(r) = \nu(r) + \frac{\delta J[\rho]}{\delta \rho(r)} + \frac{\delta E_{xc}[\rho]}{\delta \rho(r)}$$

$$= \nu(r) + \int \frac{\rho(r)}{|r - r'|} dr + \nu_{xc}(r) \tag{85}$$

where the exchange correlation is expressed as $\nu_{xc}(r) = \frac{\delta E_{xc}[\rho]}{\delta \rho(r)}$, and the total electron density $\rho(r)$ can be obtained by solving N one-electron equations

$$\left[-\frac{1}{2} \nabla^2 + \nu_{eff}(r) \right] \varphi_i = \varepsilon_i \varphi_i \tag{86}$$

Once the so-called Kohn-Sham orbitals, $\varphi_{i\sigma}$ are obtained, the total density, $\rho(r)$ is given by

$$\rho(r) = \sum_{i}^{N} \sum_{s} |\varphi_{i\sigma}(r)|^2 \tag{87}$$

Eqs. (85), (86), and (87) must be solved iteratively since $\nu_{eff}(r)$ depends on $\rho(r)$ through the ν_{xc} term. These are the equations generally known as Kohn-Sham equations. The total energy of the ground state can then be written as

$$E = \sum_{i}^{N} \varepsilon_i - \frac{1}{2} \int \frac{\rho(r)\rho(r')}{|r - r'|} dr\, dr' + E_{xc}[\rho] - \int \nu_{xc}(r)\rho(r) dr \tag{88}$$

The exact $E_{xc}(r)$ functional in the KS total energy expression has an unknown form. Approximation of E_{xc} therefore remains a focal point of research in DFT and has led to a multitude of different variants of DFT. One of these variant forms of DFT i.e., with the hybrid functional, B3LYP [6, 7, 119] has been used in some of the work presented in this dissertation.

B3LYP

B3LYP is a hybrid exchange-correlation density functional that includes Becke's three-parameter exchange energy term [7] and Lee-Yang-Parr's [119] correlation term. The acronym of this DFT variant gives the impression that the correlation contribution all comes from the LYP functional, but most practical implementations use only the non-local correlation energy contribution from the LYP functional and the local contribution comes from the Vosko, Wilk and Nuasir (VWN) [120] functional. The form of the B3LYP functional is

$$E_{xc}^{B3LYP}[\rho] = (1-a_0)E_x^{LDA}[\rho] + a_x\Delta E_x^{B88} + a_0E_x^{HF} + cE_c^{LYP}[\rho] + (1-c)E_c^{VWN}[\rho] \qquad (89)$$

where the empirical coefficients a_0, a_x, and c were determined by Becke in 1993 as 0.2, 0.72, and 0.81, respectively. The first two terms are the Becke's exchange energy term and are defined as

$$E_x^{B88}[\rho] = -\frac{3}{2}\left(\frac{3}{4\pi}\right)^{\frac{1}{3}}\int \rho^{\frac{4}{3}}dr - b\sum_{\sigma=\alpha,\beta}\int \rho_\sigma^{\frac{4}{3}}\frac{x_\sigma^2}{1+6bx_\sigma \sinh^{-1}x_\sigma}dr \qquad (90)$$

with $x_\sigma = \left|\frac{\nabla\rho_\sigma}{\rho_\sigma^{\frac{4}{3}}}\right|$,

and b = 0.0042.

E_x^{HF} is the Hartree-Fock exchange energy, and the LYP term is given as

$$E_c^{LYP}[\rho] = -a\int \frac{\rho(r) + b\rho(r)^{-2/3}\left[t_{HF}(r) - 2t_W(r)\right]e^{-c\rho(r)^{-1/3}}}{1+d\rho(r)^{-1/3}}dr \qquad (91)$$

where $t_{HF}(r) = \frac{1}{8}\sum_i \frac{|\nabla\rho_i(r)|^2}{\rho_i(r)} - \frac{1}{8}\nabla^2\rho$ is the Hartree-Fock kinetic energy density and

$t_W(r) = \frac{1}{8}\frac{|\nabla\rho(r)|^2}{\rho(r)} - \frac{1}{8}\nabla^2\rho$ is the local Weizsacker kinetic-energy density;

a = 0.04918, b = 0.132, c = 0.2533, and d = 0.349.

The correlation term by Vosko, Wilk and Nuasir is given by Eqs. (92) – (94) [120]

$$E_c^{VWN}[\rho] = \rho\varepsilon_c(x,\xi), \tag{92}$$

where $\rho = \rho_\beta + \rho_\alpha$, $x = \left(\frac{3}{4\pi\rho}\right)^{\frac{1}{6}}$, and $\xi = \frac{\rho_\alpha - \rho_\beta}{\rho}$.

The correlation potential ε_c has the form

$$\varepsilon_c(x,\xi) = \varepsilon_c^p(x) + \varepsilon_c^A(x)g(\xi)\times\left\{1 + \left[\frac{4}{9(2^{1/3}-1)}\frac{\varepsilon_c^F(x) - \varepsilon_c^P(x)}{\varepsilon_c^A(x)} - 1\right]\xi^4\right\}, \tag{93}$$

where $g(\xi) = \frac{9}{8}\left[(1+\xi)^{4/3} + (1-\xi)^{4/3} - 2\right]$ and the various ε_c have the form

$$\varepsilon_c(x) = A\left\{\ln\frac{x^2}{X(x)} + \frac{2b}{Q}\tan^{-1}\frac{Q}{2x+b} - \frac{bx_0}{X(x_0)}\left[\ln\frac{(x-x_0)^2}{X(x)} + \frac{2(2x_0+b)}{Q}\tan^{-1}\frac{Q}{2x+b}\right]\right\}$$

(94)

where $X(x) = x^2 + bx + c$, $Q = (4c - b^2)^{1/2}$, and A, b, c, and x_0 are parameters assuming different values for each individual ε_c.

Riley et al.[121] assessed the performance of the B3LYP method in its ability to calculate molecular properties, such as bond lengths, bond angles, ground state vibrational frequencies, heats of formation, conformation energies, reaction barrier heights, electron affinities (EA) and ionization energies (IP). B3LYP was found to produce results with the lowest errors for bond lengths, and bond angles, and was the most accurate of the hybrid-GGA class for calculating vibrational frequencies [121]. Also Raymond and Wheeler [122] used the B3LYP method to study numerous small inorganic molecules; they obtained results which were not only comparable to experimental results but comparable to results from other computational studies found in the literature. Maung et al. [123] used different DFT functionals to evaluate the bond dissociation energies for simple selenium-containing molecules and their calculations showed that B3LYP with the 6-311G*, 6-311+G(d,p) and 6-311++G(d,p) basis sets, produced the most accurate DFT energy (4.6 kcal mol^{-1} different from experiment) [124]. Moreover, B3LYP calculations have less basis set sensitivity compared to MP2 calculations [123, 125] because in progressing from a small basis set, e.g. 3-21G* to the extended basis set, e.g. 6-311++G(3df,3pd), the predicted bond dissociation energy for HSe-H bond changes only by 2.0 kcal/mol [123]. As a result, the B3LYP method, with appropriate basis sets, was used in obtaining optimized geometrical structures in this dissertation when optimizations using wave function methods were deemed as unnecessarily costly.

CHAPTER III

GROUND AND LOW-LYING EXCITED ELECTRONIC STATES OF [3,3']BIDIAZIRINYLIDENE (C_2N_4) in D_{2h} symmetry

Introduction

Diazirine and its derivatives have been studied extensively with emphasis on synthesis and understanding the mechanisms of their decomposition [10, 126-130]. They decompose and generate carbenes through thermolysis or photolysis with short irradiation time [10, 126]. Diazirine and its derivatives are a class of highly strained compounds [15], with the characteristic feature being their three-membered CN_2 rings. The particular compound of interest in this study, [3,3']bidiazirinylidene (C_2N_4) (Figure 1, Chapter I), is a derivative of diazirine with D_{2h} symmetry; it consists of two CN_2 rings. Based on previous investigations of substituted diazirines [131], [3,3']bidiazirinylidene was postulated to be electronically and geometrically similar, especially in the ring moieties. In particular, the compound is expected to be metastable with respect to its dissociation products. Recently, there has been renewed interest in the search for molecular species having long–lived metastable ground states not only because their decomposition is accompanied by the release of energy, but products are often formed in excited electronic states. Consequently, these types of molecules are possible energy carriers and/or laser excitation sources. Examples include: difluorodiazirine (F_2CN_2), which dissociates with the release of energy to form $CF_2 + N_2$ [2], CO_4, and CO_2N_2 [132, 133]. To the best of our knowledge, the ground- and low-lying excited electronic states of this diazirine

derivative have not been characterized either experimentally or theoretically prior to our paper [134]. Moreover, we are not aware of any other studies on compounds with multiple CN_2 rings; their investigation may identify new directions for novel high energy density molecules.

The theoretical investigation of C_2N_4, especially its excited electronic states, is a significant computational challenge and, like other diazirine derivatives, requires high–level methods that allow for a balanced treatment of dynamical and nondynamical electron correlation. The second-order generalized Van Vleck perturbation theory (GVVPT2) [1, 135], a variant of multireference perturbation theory, has been proven to describe well the ground and excited electronic states of closely related molecules, such as difluorodiazirine (F_2CN_2) [2] and difluorodioxirane (CF_2O_2) [136]. Additionally, the GVVPT2 method has been shown to elucidate other particularly difficult excited state electronic structures, including those of disulfur monoxide (S_2O) [137] and the azabenzenes [138], which also require balanced treatments of dynamical and nondynamical correlation effects. Its results are in good agreement to those of coupled cluster with single and double excitations (CCSD) [72] with perturbative triples CCSD(T) [4], when CCSD is applicable, although GVVPT2 is more widely applicable than single reference CCSD. GVVPT2 is a credible alternative to the significantly more computationally intensive multireference configuration interaction with single and double excitations (MRCISD) method for many problems.

In this chapter, the results of the equilibrium geometries of the ground and low-lying electronic states of the diazirine derivative C_2N_4 determined at the GVVPT2 level using a cc-pVDZ [139] basis are reported. Taking into account that studies on related

diazirines showed significant geometry changes with electronic state, optimization of geometries for all states was considered essential. Based on previous theoretical and experimental studies of related molecules with three-membered rings in their ground states (e.g., difluorodiazirine [2], dioxirane [136] and fluorofluoroxydioxirane [3]), low–lying excited states are expected to be produced by excitations located within the ring fragment with the retention of the ring moiety, but leading to elongation of the N–N bond length. Consequently, several low–lying excited states of D_{2h} symmetry (2^1A_g, 1^1B_{1g}, 1^3B_{1g}, 1^1B_{2g}, 1^3B_{2g}, 1^1B_{3g}, 1^3B_{3g}, 1^1B_{2u}, 1^3B_{2u}, 1^1B_{3u}, and 1^3B_{3u}) of this molecule were examined. Besides the adiabatic energy separations for the excited states, additional calculations were performed to obtain the vertical excitation energies from the ground state and the vertical emission energies from the excited states. Harmonic frequencies of the equilibrium ground state geometry were also determined, at the multiconfigurational self-consistent field (MCSCF) level, to predict the vibrational spectroscopy and estimate the rigidity of the molecule. Calculations with larger basis sets (cc-pVTZ [139] and aug-cc-pVTZ [139, 140]) were performed to assess basis set effects. All MCSCF and GVVPT2 calculations were performed using a local electronic structure software suite (i.e., UNDMOL). Additional studies of the ground-state geometry were also performed at other levels of theory: Hartree–Fock (RHF); second–order Møller–Plesset perturbation theory (MP2); coupled cluster with single and double excitations (CCSD); and quadratic configuration interaction with single and double excitations (QCISD) [4]. These calculations were performed using the Gaussian 03 program [141]. CCSD(T) [4] calculations on the ground state and additional calculations to characterize the excited states using EOM-CCSD [50, 142, 143] were done using GAMESS [144, 145].

The first part of this chapter is divided into three additional sections. In Section 2, computational details, including a description of the model space constructed using the macroconfiguration approach [96], is given. Section 3 presents the results of the study and a discussion that includes a comparison of features of C_2N_4 relative to those for difluorodiazirine, for which both experimental and theoretical results are available. A final section summarizes the work.

Computational details

The model spaces used in this study include all spin and space symmetry-allowed configurations generated by single and double excitations from the 14 highest occupied orbitals to the 10 lowest unoccupied orbitals. From preliminary single-reference studies of the 1^1A_g ground state, orbital groups for MCSCF and subsequent GVVPT2 calculations were constructed as follows: the fourteen highest occupied orbitals were divided into two subgroups (G_1 and G_2) involving eight and six orbitals, respectively. The first subgroup includes the eight lowest orbitals: $G_1 = (3a_g, 3b_{1u}, 4a_g, 2b_{2u}, 2b_{3g}, 4b_{1u}, 5a_g, 2b_{3u})$. The second subgroup involves the six highest lying occupied valence orbitals: $G_2 = (5b_{1u}, 6a_g, 1b_{2g}, 3b_{2u}, 3b_{3g}, 2b_{3u})$. The 10 lowest virtual orbitals were also divided into two subgroups (V_1 and V_2), involving six and four orbitals, respectively: $V_1 = (1b_{1g}, 1a_u, 4b_{2u}, 2b_{2g}, 6b_{1u}, 5b_{2u})$, $V_2 = (4b_{3g}, 7a_g, 7b_{1u}, 5b_{3g})$. Figure 7 shows the orbitals of the groups G_2 and V_1 that proved to be qualitatively significant for the low-lying excited electronic states. Based on this partitioning of the valence orbitals, fourteen macroconfigurations describing single and double excitations from G_1 and G_2 to V_1 and V_2 were created. Although the same model space could be generated from just three macroconfigurations using two groups, both computational efficiency and interpretability

is increased with the used granulation.

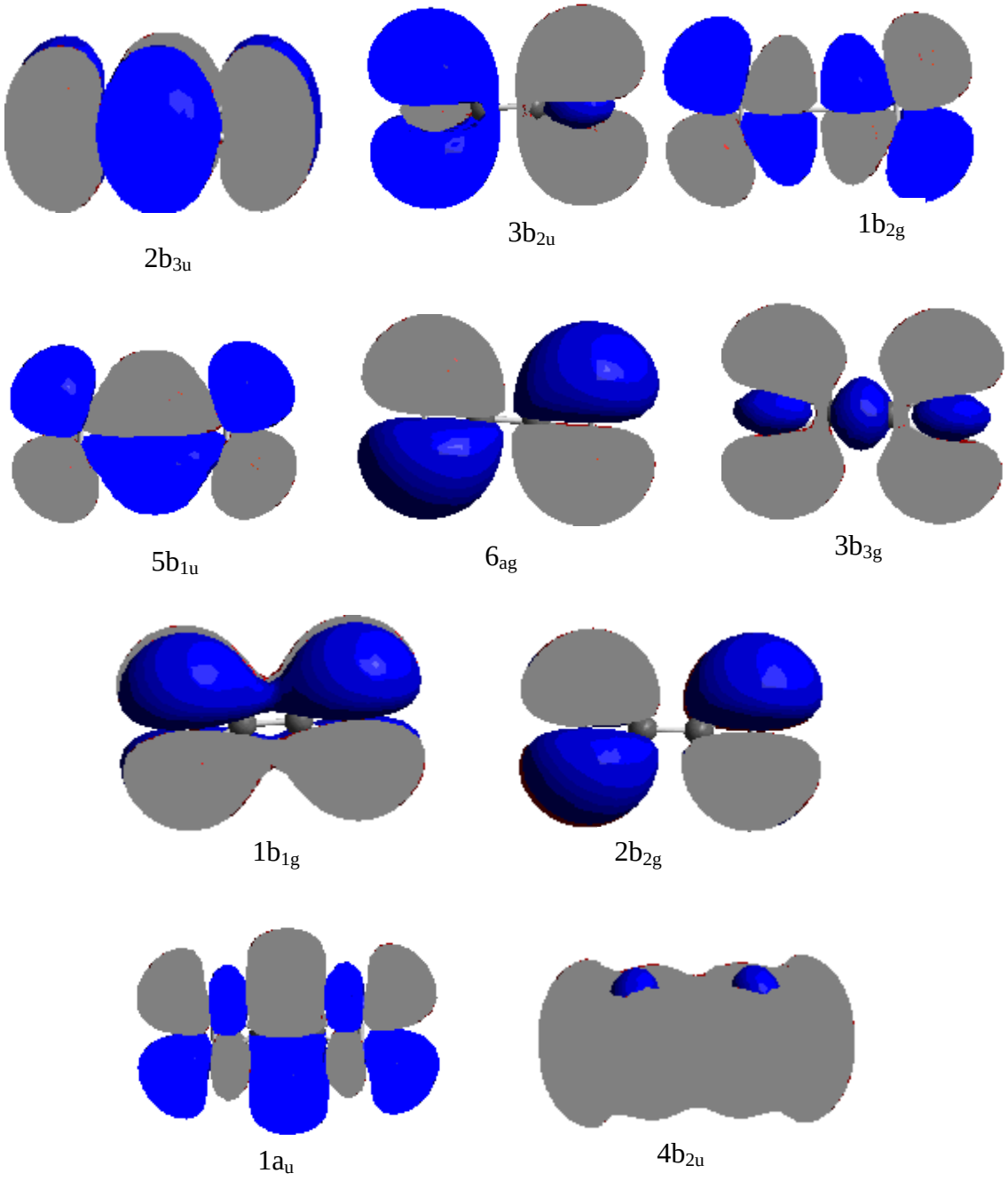

Figure 7. 3-D plots of orbitals of groups G_2 and some of V_1 of [3,3'] bidiazirinylidene in D_{2h} symmetry.

The list of macroconfigurations determining the incomplete model space used includes: the closed–shell macroconfiguration describing the ground state,

$(G_1)^{16}\,(G_2)^{12}\,(V_1)^{0}\,(V_2)^{0}$;

macroconfigurations describing all single excitations from G_1 or G_2 to V_1 or V_2,

$(G_1)^{15}\,(G_2)^{12}\,(V_1)^{1}\,(V_2)^{0}$, $(G_1)^{15}\,(G_2)^{12}\,(V_1)^{0}\,(V_2)^{1}$,

$(G_1)^{16}\,(G_2)^{11}\,(V_1)^{1}\,(V_2)^{0}$, $(G_1)^{16}\,(G_2)^{11}\,(V_1)^{0}\,(V_2)^{1}$; and

macroconfigurations describing all double excitations from G_1 and/or G_2 to V_1 and/or V_2,

$(G_1)^{14}\,(G_2)^{12}\,(V_1)^{2}\,(V_2)^{0}$, $(G_1)^{14}\,(G_2)^{12}\,(V_1)^{0}\,(V_2)^{2}$,

$(G_1)^{16}\,(G_2)^{10}\,(V_1)^{2}\,(V_2)^{0}$, $(G_1)^{16}\,(G_2)^{10}\,(V_1)^{0}\,(V_2)^{2}$,

$(G_1)^{14}\,(G_2)^{12}\,(V_1)^{1}\,(V_2)^{1}$, $(G_1)^{16}\,(G_2)^{10}\,(V_1)^{1}\,(V_2)^{1}$,

$(G_1)^{15}\,(G_2)^{11}\,(V_1)^{2}\,(V_2)^{0}$, $(G_1)^{15}\,(G_2)^{11}\,(V_1)^{0}\,(V_2)^{2}$,

$(G_1)^{15}\,(G_2)^{11}\,(V_1)^{1}\,(V_2)^{1}$.

The ground state has ^1A_g symmetry and its model space is spanned by 1390 configuration state functions (CSFs) created by 856 configurations. The dimension of the corresponding external space depends on the basis set used. For the cc-pVDZ atomic basis, the external space is spanned by 199,054,113 CSFs (26,803,566 configurations); the cc-pVTZ basis leads to a much larger dimension of about 1.43 billion CSFs (more than 187 million configurations). The dimensions of the model space for excited states

were as follows: for $^1B_{2u}$ and $^3B_{2u}$ states (as well as for $^1B_{3g}$ and $^3B_{3g}$ states), the model spaces were spanned by 1303 CSFs and 1824 CSFs, respectively (created by 782 configurations); for $^1B_{3u}$ and $^3B_{3u}$ states, the model spaces were spanned by 1183 CSFs and 1672 CSFs respectively (created by 694 configurations); for the 1^1B_{2g} and 1^3B_{2g} states, the model spaces were spanned by 1181 CSFs and 1680 CSFs respectively (created by 682 configurations); and the model spaces for both $^1B_{1g}$ and $^3B_{1g}$ states were spanned by 1672 CSFs (created by 656 configurations). The dimensions of the external spaces for triplet states were significantly larger than for ^1A_g symmetry (for example, 380.1 million CSFs for cc-pVDZ), but those for the singlet excited states were similar to that for the ground state (approximately 199 million CSFs). The current GUGA-based GVVPT2 program in UNDMOL [135] can perform the described calculations in reasonable time; e.g., a typical GVVPT2 calculation required 11 minutes for 199 million total CSFs and 1390 model CSFs on a 2.0 GHz dual-core AMD Opteron processor 2212.

Table 1. Comparison of Optimized Geometries of the Ground State of C_2N_4 cc-pVDZ.

	MP2	MCSCF	CCSD	QCISD	CCSD(T)	GVVPT2
R_{CC} (Å)	1.300	1.296	1.302	1.302	1.304	1.303
R_{CN} (Å)	1.433	1.420	1.428	1.429	1.437	1.433
R_{NN} (Å)	1.290	1.251	1.265	1.266	1.278	1.282
∠NCN (deg)	53.5	52.3	52.6	52.6	52.6	53.1
∠CNN (deg)	63.3	63.9	63.7	63.2	63.2	63.4

Table 2. Comparison of optimized geometries of the ground state of C_2N_4 to that of F_2CN_2 at the GVVPT2 level of theory.

	C_2N_4 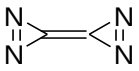		F_2CN_2 	
	cc-pVDZ	cc-pVTZ	cc-pVDZ[a]	cc-pVTZ[a]
R_{CC} (Å)	1.303	1.288	-	-
R_{CN} (Å)	1.433	1.424	1.421	1.417
R_{NN} (Å)	1.282	1.268	1.288	1.281
∠NCN (°)	53.1	52.9	53.9	53.7

[a] Reference [2]

Electronic and molecular structures

The geometry of the 1^1A_g ground state of C_2N_4 was optimized at the GVVPT2 level of theory using both cc-pVDZ and cc-pVTZ basis sets. Optimizations with other methods were performed using the cc-pVDZ basis set. Comparing the structural parameters for the ground state of the C_2N_4 molecule optimized at the GVVPT2 level to that obtained using the MP2, CCSD, and QCISD methods shows (Table 1) that they are in close agreement except for the N–N bond length. The R_{CC} bond length is about 0.001 Å longer than that from the CCSD and QCISD methods and 0.003 Å longer than that from the MP2 method; the R_{CN} bond length is 0.005 Å and 0.004 Å longer than that with

using CCSD and QCISD, respectively, but the same as for the MP2 method, but 0.004 Å shorter than with CCSD(T). There is greater variation between methods for the predicted R_{NN} bond lengths: the GVVPT2 result is 0.017, 0.016 and 0.031 Å longer than that of CCSD, QCISD, and MCSCF, respectively, and 0.008 Å shorter than that of MP2. The CCSD(T) N—N bond length is quite close to the GVVPT2 value, 0.004 Å; as in the case of F_2CN_2 [2], GVVPT2 and CCSD(T) are in good agreement. The $\angle$NCN angle predicted by GVVPT2 is only 0.5° larger than that for the CCSD and QCISD methods, 0.8° larger than for MCSCF, but is 0.4° smaller than that for the MP2.

Experimental results for C_2N_4 are not available. To gain further understanding of the results of the calculations, the optimized parameters for C_2N_4 are compared to those of F_2CN_2, which has been investigated both experimentally and theoretically (see Table 1 in Ref. 2), as can be seen from Table 2. R_{CN} and R_{NN} bond lengths and the $\angle$NCN angle obtained at the GVVPT2 level using the cc-pVDZ and cc-pVTZ basis sets for the C_2N_4 molecule are in good agreement with those for F_2CN_2. R_{CN} and R_{NN} bonds for C_2N_4 using the cc-pVDZ basis are only 0.012 Å and 0.006 Å longer than those for F_2CN_2, respectively, and the $\angle$NCN angle in C_2N_4 is only 0.8° smaller than that for F_2CN_2. These results show that [3,3']bidiazirinylidene is quite similar to F_2CN_2, and that GVVPT2 can be expected to describe the electronic structure of C_2N_4 to similar accuracy.

GVVPT2 calculations for the ground state of C_2N_4 show that the leading configuration is $\cdots (1b_{3u})^2(6a_g)^2(1b_{2g})^2(3b_{3g})^2(5b_{1u})^2(3b_{2u})^2(2b_{3u})^2$ with an amplitude of 0.73. This amplitude is much smaller than it is in the MCSCF calculation (where the amplitude is 0.93). Similar results are obtained for the excited states, which demonstrates the significant effect of dynamic correlation on the reference configurations.

Table 3. Vibrational frequencies (cm^{-1}) of the 1^1Ag state calculated at HF/cc-pVDZ, MP2/cc-pVDZ and MCSCF/cc-pVDZ levels of theory.

vibration	HF	MP2	MCSCF
υ_1 (B_{2u})	196.7	173.5	270.3
υ_2 (B_{3u})	306.3	263.9	311.5
υ_3 (B_{2g})	400.9	298.7	375.9
υ_4 (A_u)	410.0	364.4	449.2
υ_5 (B_{3g})	545.2	443.8	533.2
υ_6 (A_g)	680.5	605.4	608.2
υ_7 (B_{2u})	1099	819.0	934.4
υ_8 (B_{3g})	1149	890.3	995.5
υ_9 (B_{1u})	1291	1109	1127
υ_{10} (A_g)	1801	1352	1470
υ_{11} (B_{1u})	1906	1486	1562
υ_{12} (A_g)	2293	2078	2084

Frequency calculations of the C_2N_4 molecule at the HF, MP2 and MCSCF levels of theory with the cc-pVDZ basis are given in Table 3 at their respective equilibrium geometries. The NN symmetric and asymmetric stretching frequencies at 1470 cm^{-1} and 1562 cm^{-1} (at the MCSCF level) of C_2N_4 can be compared to the NN stretching mode of F_2CN_2 [9, 146] with a frequency of about 1650 cm^{-1}, which is characteristic of a N=N double bond. The B_{2u} and B_{3g} symmetric and asymmetric CN stretching frequencies of 934.4 cm^{-1} and 995.5 cm^{-1} (at the MCSCF level) are similar to the B_2 asymmetric CN stretching frequency in F_2CN_2 [9, 146] at 1091 cm^{-1}. The similarity of the vibrational spectrum of C_2N_4 to that of F_2CN_2 corroborates the supposition that they have similar electronic structures.

The stability of C_2N_4 relative to dissociation to N_2 + C_2N_2 was surveyed by a series of GVVPT2 calculations along an approximate reaction path. A path in which the distance between one N_2 moiety and the C_2N_2 fragment was gradually varied, with all

other geometrical parameters held constant, is shown in Figure 8. The abscissa is labeled by the distance from the center of the two carbons to the center of the two nitrogen atoms. As can be seen in Figure 8, the dissociation energy is predicted to be no larger than 1.32 eV (30.4 kcal/mol) with the barrier no larger than 5.64 eV (130 kcal/mol). Relaxation of geometrical parameters will lead to a lowering of these limits.

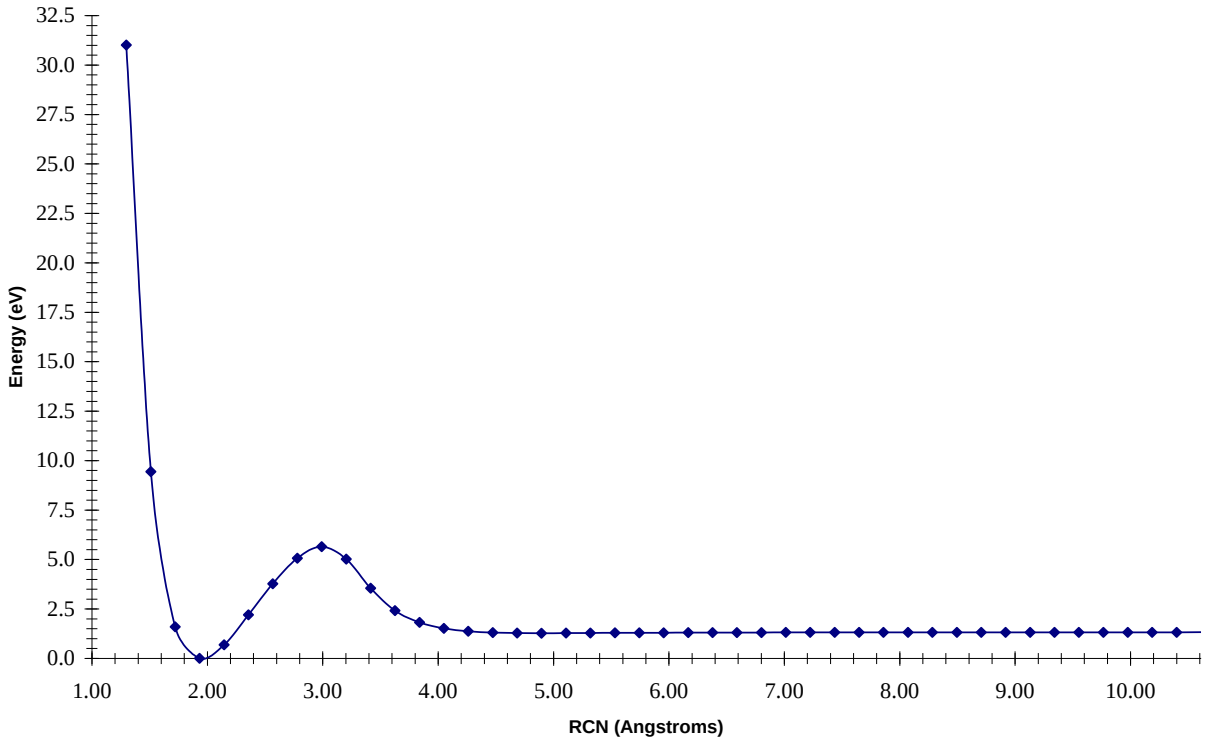

Figure 8. Cut along PES through the equilibrium geometry of the 1^1Ag state of C_2N_4 leading to dissociation to $N_2 + C_2N_2$.

In the 1^1B_{1g} excited state, the leading configuration by which this state is related to the ground state can be described as the $2b_{3u} => 4b_{2u}$ single electron excitation, as can be seen in Figure 9. The amplitude of this configuration is 0.631. Qualitatively the excitation is from a π-bonding N–N orbital to a σ-antibonding N–N orbital, which is consistent with the observed elongation of the N–N bond length (by +0.046 Å); R_{CN} also

increases by +0.034 Å (Table 4). The R_{CC} bond increases for this excitation by +0.035 Å. The leading configurations for the triplet state (1^3B_{1g}) can be described as two, single electron excitations, $5b_{1u}$ => $1a_u$ and $6a_g$ => $1b_{1g}$, having amplitudes of 0.541 and 0.566, respectively. These electron transitions are from σ-bonding N–N orbitals to π-antibonding N–N orbitals. They lead to elongation of the N–N bond by 0.094 Å, but the C–C bond does not change.

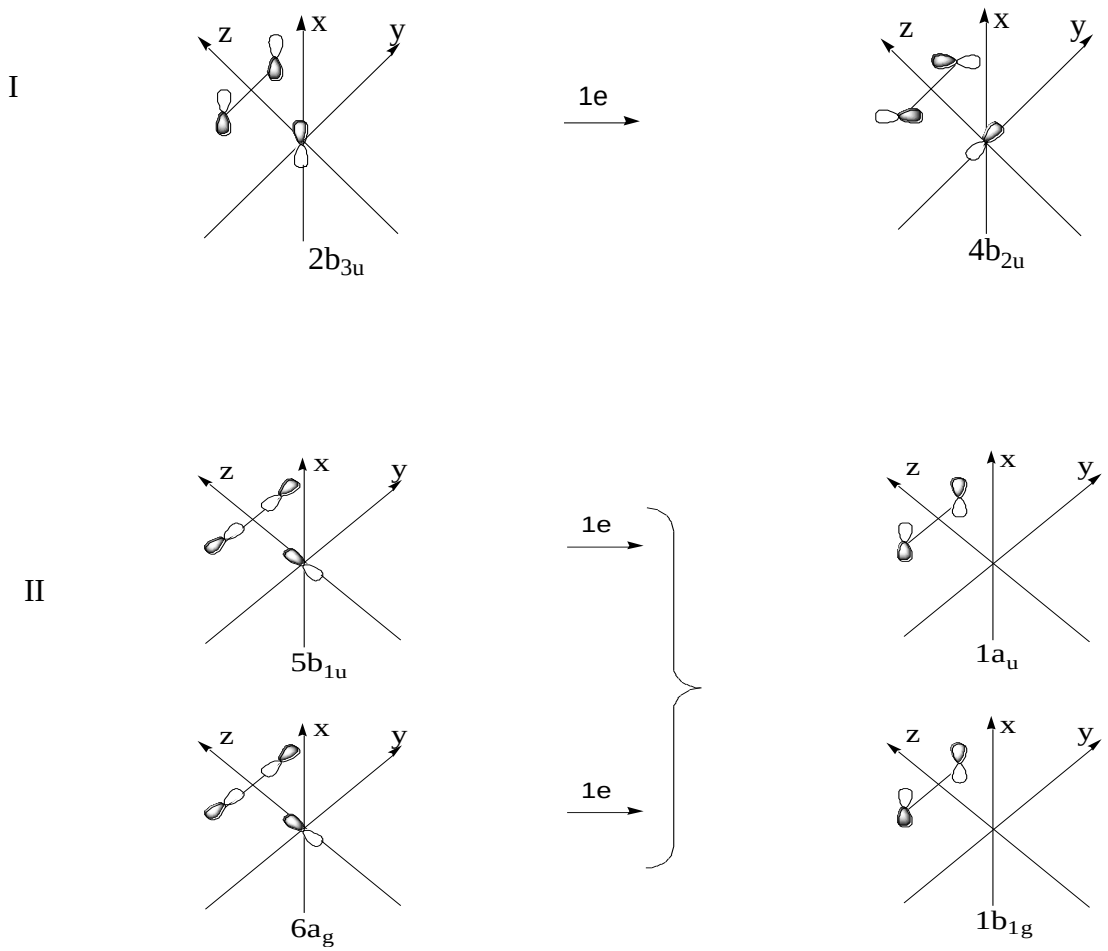

Figure 9. The leading excitations for the 1 $^{1,3}B_{1g}$ excited state of C_2N_4.

Unlike the B_{1g} states, the electronic structures for the 1^1B_{2g} and 1^3B_{2g} states are similar. The leading configuration of both states can be described as the one-electron

excitation $3b_{3g}$ =>$1b_{1g}$ relative to the closed-shell reference (Figure 10). The amplitude of this configuration in the 1^1B_{2g} state is 0.626, and it is 0.597 in the 1^3B_{2g} state. This configuration corresponds to excitation from the antisymmetric, banana-type, three-centered N–C–N bonding orbital to a π-antibonding N–N orbital. The excitation leads to the elongation of the N–N and C–N bonds, with the shortening of the C–C bond (Tables 2 and 4) and retention of the CN_2 ring moiety. The analogous excitations are responsible for transitions from the 1^1A_1 ground state to the 1^1B_1 and 1^3B_1 excited states of F_2CN_2. The curious shortening of the C–C bond is related to loss of C–C π-antibonding character in excitation from the $3b_{3g}$ orbital. GVVPT2 calculations for the 1^3B_{2g} state of C_2N_4 predict that the N–N bonds increase by +0.012 Å and the C–C bond decreases by 0.024 Å relative to the ground state. This is similar to (but smaller than) the corresponding changes in F_2CN_2: increment of +0.031 Å (GVVPT2/cc-pVDZ), +0.038 Å (experimental) [2] in the N–N bond length.

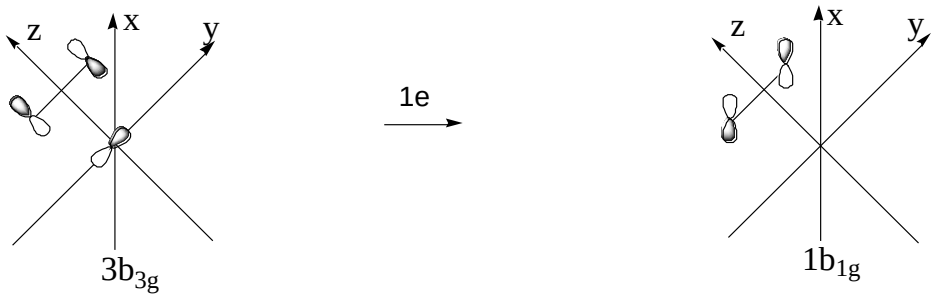

Figure 10. The leading excitations for the $1\ ^{1,3}B_{2g}$ excited state of C_2N_4.

Table 4. GVVPT2/cc-pVDZ-optimized geometries of the excited states of C_2N_4.

	2^1A_g	1^1B_{1g}	1^3B_{1g}	1^1B_{2g}	1^3B_{2g}	1^1B_{3g}	1^3B_{3g}	1^1B_{2u}	1^3B_{2u}	1^1B_{3u}	1^3B_{3u}
R_{CC} (Å)	1.926	1.338	1.303	1.269	1.279	1.409	1.409	1.393	1.360	1.276	1.279
R_{CN} (Å)	1.769	1.467	1.421	1.449	1.447	1.412	1.367	1.379	1.370	1.465	1.447
R_{NN} (Å)	1.427	1.328	1.376	1.282	1.294	1.388	1.388	1.402	1.382	1.286	1.295
∠NCN(deg)	47.6	53.8	57.9	52.5	53.1	58.9	59.5	61.1	60.6	52.04	53.1
∠CNN(deg)	66.2	63.1	61.0	63.7	63.4	60.6	61.0	59.5	59.7	64.0	63.4

For the 1^1B_{3g} and 1^3B_{3g} excited states of C_2N_4, the leading configurations mainly involve the $2b_{3u}$ => $1a_u$ one electron excitation relative to the ground state (Figure 11). The amplitudes for these configurations are 0.625 for the singlet state and 0.621 for the triplet state. The corresponding electronic excitations in F_2CN_2 are responsible for transitions from 1^1A^1 to the 1^1B_2 and 1^3B_2 excited the triplet states. The excitation is from a π-bonding N–N orbital to a π-antibonding N–N orbital, leading to an increase in R_{NN} by +0.106 Å for both states. These large increases in the N–N bond length also result in a large increase in the N–C–N angle (+5.8° for the singlet, +6.4° for triplet) with respect to the ground state.

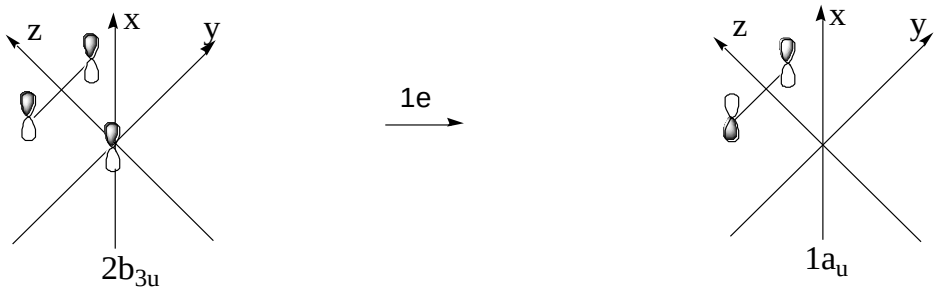

Figure 11. The leading excitations for the $1\ ^{1,3}B_{3g}$ excited state of C_2N_4.

Qualitatively, the excitations involved in the 1^1B_{2u} and 1^3B_{2u} excited states of C_2N_4 are similar and have the same nature as those in the 1^1B_{3g} and 1^3B_{3g} states: an excitation from a π-bonding N–N orbital to a π-antibonding N–N orbital. The leading configurations of the 1^1B_{2u} and 1^3B_{2u} states can be described as the $2b_{3u}$ => $1b_{1g}$ single excitation relative to the ground state reference (Figure 12). The $1b_{1g}$ orbital is a symmetric combination of π-antibonding N–N orbitals, while the $1a_u$ orbital (of importance in the 1^1B_{3g} and 1^3B_{3g} states) is the antisymmetric combination. The

amplitude for the $2b_{3u}$ => $1b_{1g}$ configuration is 0.645 for the singlet state and 0.618 for the triplet. This excitation leads to an increase in R_{NN} by +0.120 Å for the singlet (1^1B_{2u}) and +0.100 Å for the triplet (1^3B_{2u}) excited states. The N–C–N angle is also increased during these excitations: for the singlet state by +8.0° and by +7.5° for the triplet state (1^3B_{2u}).

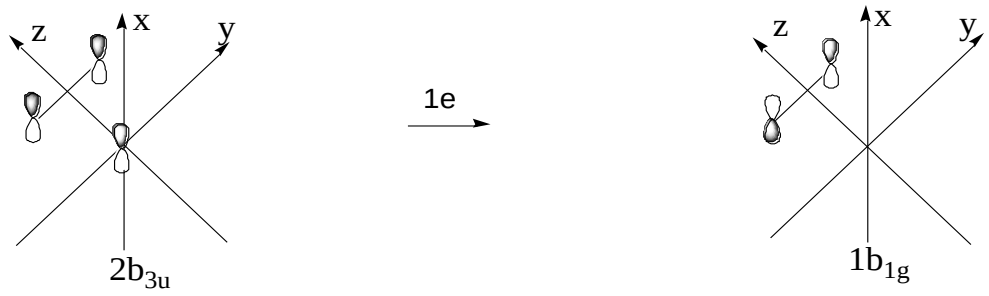

Figure 12. The leading excitations for the $1\ ^{1,3}B_{2u}$ excited state of C_2N_4.

The leading configurations of both the 1^1B_{3u} and 1^3B_{3u} excited states are qualitatively described in terms of the $3b_{3g}$ => $1a_u$ single excitation relative to the closed-shell reference (Figure 13). This is analogous to electronic transition from 1^1A_1 to 1^1B_1 and 1^3B_1 states in the F_2CN_2 molecule. The excitation is from the antisymmetric, banana-type, three-centered N–C–N bonding orbital to a π-antibonding N–N orbital. The amplitude of the configuration is 0.621 for the singlet (1^1B_{3u}) and 0.594 for the triplet state (1^3B_{3u}). The excitation is similar to that for the 1^1B_{2g} and 1^3B_{2g} excited states discussed above, except that the $1a_u$ orbital is the antisymmetric combination of π-antibonding N–N orbitals while the $1b_{1g}$ orbital is the symmetric combination. As with the B_{3u} states, there is an elongation of the N–N bond (by 0.004 Å in the present case) and an identical decrease in the C–C bond (by 0.024 Å).

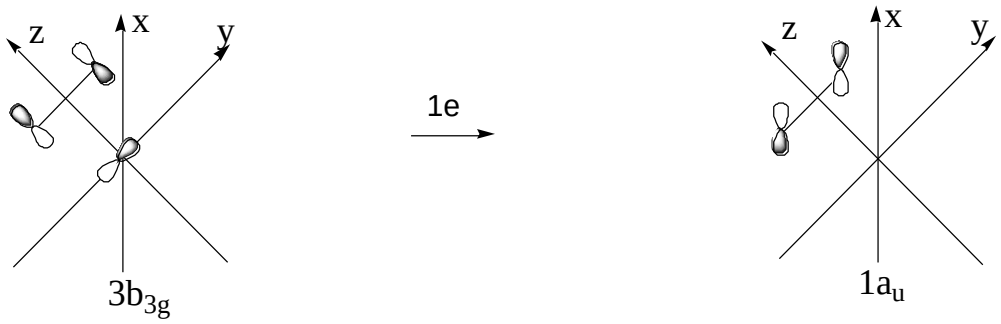

Figure 13. The leading excitations for the 1 $^{1,3}B_{3u}$ excited state of C_2N_4.

The second singlet state of the same symmetry as the ground state (2^1A_g) is highly multiconfigurational with the following leading configurations: the closed-shell configuration with amplitude of 0.364; a two-electron excitation from $2b_{3u}$ to $1b_{1g}$ with amplitude of 0.196; and another two-electron excitation from $2b_{3u}$ to $1a_u$ with amplitude of 0.134, relative to the ground state reference (Figure 14). The excitations are from a π-bonding N–N orbital to π-antibonding N–N orbitals. As expected, this excitation leads to a significant increase in the N–N bond (of 0.145 Å), but also, unlike all other excited states discussed, a very large increase in the C–C bond (of 0.623 Å).

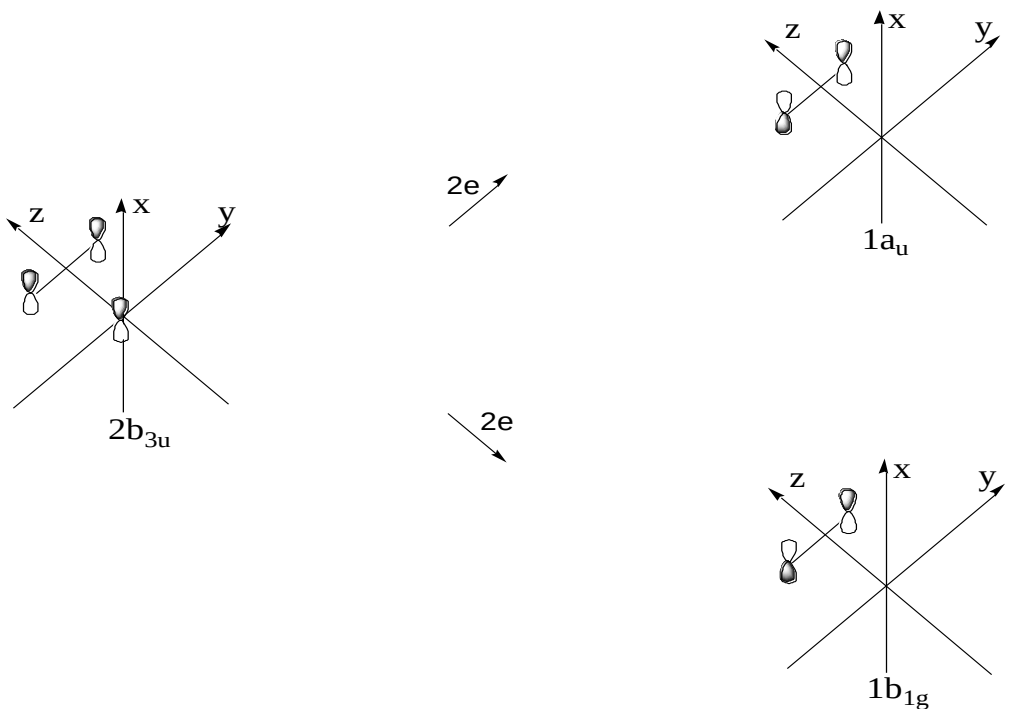

Figure 14. The leading excitations for the 2 ^1A_g excited state of C_2N_4.

In Figure 15, the vertical and adiabatic excitation energies of the low–lying excited states of C_2N_4 with respect to the ground state, calculated using the GVVPT2/cc-pVDZ level of theory, are shown. The lowest energy vertical excitation is to the 1^3B_{2g} triplet state, which is not symmetry-allowed because of both spin and dipole selection rules, and has an energy of 2.33 eV, followed by the spin forbidden but dipole allowed transition to 1^3B_{3u} with an excitation energy of 2.37 eV. The lowest-energy spin and dipole symmetry-allowed excitation is to 1^1B_{2u} at an energy of 2.57 eV (wavelength of 482.4 nm), followed by a spin allowed but dipole forbidden transfer to 1^1B_{3g} with an excitation energy of 2.66 eV. A pair of spin-forbidden transitions to 1^3B_{2u} and $1^3B_{3g,}$ with excitation energies of 2.71 eV and 2.75 eV, respectively, are the next lowest

transitions. The excitation energy of 1^1B_{2g} is 3.03 eV and of 1^1B_{3u} is 3.07 eV. The 1^1B_{1g} and 1^3B_{1g} states are predicted to have yet higher excitation energies of 5.75 eV and 5.66 eV, respectively.

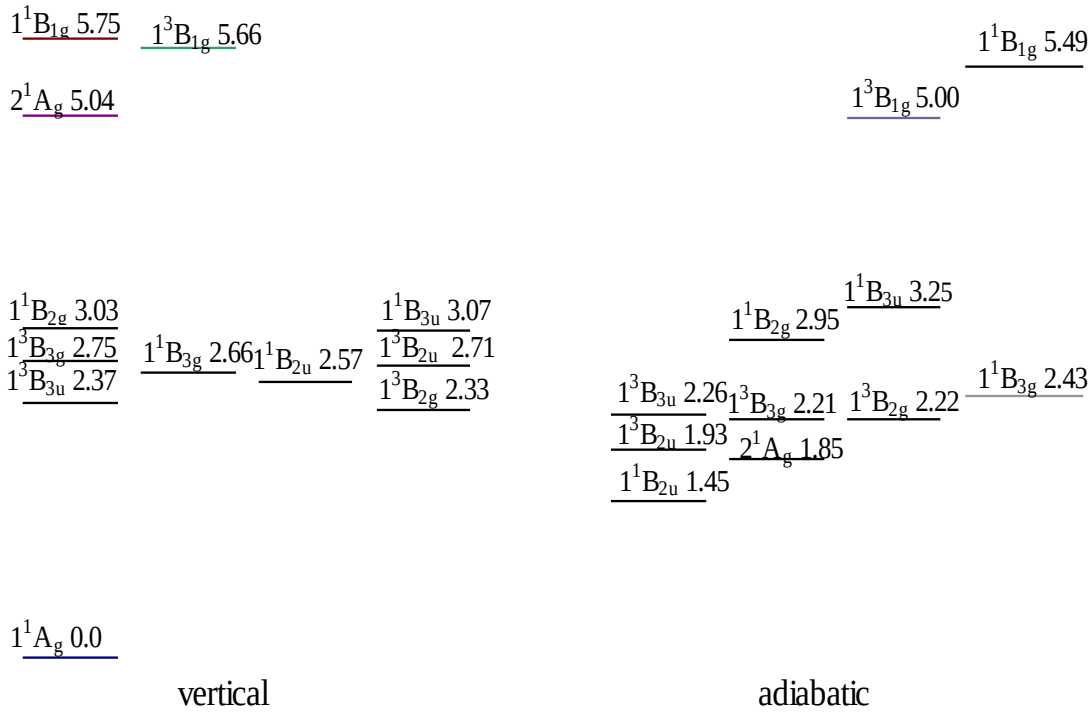

Figure 15. Vertical and adiabatic excitation energies (eV) of low-lying excited states of C_2N_4, calculated at the GVVPT2/cc-pVDZ level of theory.

EOM-CCSD//CCSD calculations were performed for all singlet excited states. The low-lying transition characteristic of diazirine rings (i.e., from the antisymmetric, banana-type, three centered N—C—N bonding orbital to a π-antibonding N—N orbital), which gives the 1^1B_{2g} and 1^1B_{3u} states in C_2N_4, is predicted to occur at 3.97 and 4.02 eV, respectively. This may be compared to the value of 4.27 eV in CH_2N_2 that was recently calculated by Fedorov et al. [131] Furthermore, a dipole strength of 0.072 and an

oscillator strength of 0.00711 were calculated for the 1^1B_{3u} state of C_2N_4, which is to be compared to the CH_2N_2 calculations of Fedorov et al. that obtained 0.037 and 0.004 respectively [131].

Because Rydberg orbitals could have an effect on excitation energies, additional, more accurate, calculations were performed using GVVPT2 with the aug-cc-pVTZ basis. The results of these calculations are given in Table 5, which also provides the results using the cc-pVDZ basis and the change in predicted excitation energies. The relative energies of most of the excited states are stabilized (by an average of 0.38 eV) with the use of the larger basis. However, there are some exceptions: both singlet and triplet B_{3u} states are stabilized less than the ground state, as is the lowest $^1B_{1g}$ state. (N.B. The lowest triplet B_{1g} has a very minor stabilization of 0.07 eV.) Although there is some change in the predicted order of excited states between the cc-pVDZ and aug-cc-pVTZ results, especially in the relatively dense region between 2 and 3 eV, the order of allowed transitions from the ground state (i.e., to 1^1B_{2u} and 1^1B_{3u}) is unchanged.

Adiabatic excitation energies were calculated from the corresponding optimized geometries of each low-lying excited state. From GVVPT2/cc-pVDZ calculations, the 1^1B_{2u} state has the lowest adiabatic excitation energy of 1.45 eV, followed by the 2^1A_g excited state. The large differences between the vertical and adiabatic excitation energies are not surprising considering that the equilibrium geometries of the excited states are significantly different from that of the ground state. The relaxation energies of the excited states relative to the vertical excitation energies from the 1^1A_g equilibrium geometry are: 1^1B_{1g} is stabilized by 0.26 eV, 1^1B_{2g} by 0.08 eV, 1^3B_{2g} by 0.11 eV, 1^1B_{3g} by 0.23 eV, 1^3B_{3g} by 0.54 eV, 1^1B_{2u} by 1.12 eV, 1^3B_{2u} by 0.78 eV, 1^3B_{3u} by 0.11 eV, and

2^1A_g by 3.19 eV. The greatest change is seen for 2^1A_g (3.19 eV) followed by 1^1B_{2u} (1.12 eV). The excess internal energies of all other states are below 1.0 eV.

Table 5. Comparison of cc-pVDZ and aug-cc-pVTZ GVVPT2 vertical excitation energies (eV) of low-lying excitation states of C_2N_4.

State	aug-cc-pVTZ	cc-pVDZ	difference
1^3B_{2g}	1.99	2.33	-0.34
1^3B_{2u}	2.11	2.71	-0.60
1^3B_{3g}	2.21	2.75	-0.54
1^1B_{2u}	2.30	2.57	-0.27
1^1B_{3g}	2.41	2.66	-0.25
1^3B_{3u}	2.45	2.37	+0.08
1^1B_{2g}	2.59	3.03	-0.44
1^1B_{3u}	3.14	3.07	+0.07
2^1A_g	4.54	5.04	-0.50
1^3B_{1g}	5.59	5.66	-0.07
1^1B_{1g}	5.78	5.75	-0.03

Vertical emission energies from all the excited state minima relative to the 1^1A_g ground state surface have been calculated. The transitions that are both spin and dipole allowed are those from the 1^1B_{2u} and 1^1B_{3u} excited states, occurring at 1.33 eV and 2.85 eV respectively. The remaining transitions are: 1^1B_{1g} emits with 5.50 eV, 1^3B_{1g} with 4.40 eV , 2^1A_g with 3.30 eV, 1^1B_{2g} with 2.78 eV, 1^3B_{3u} with 2.28 eV, 1^3B_{2g} with 2.23 eV, 1^3B_{2u} with 1.79 eV, 1^1B_{3g} with 1.55 eV, and 1^3B_{3g} with 1.50 eV. These values are smaller than the corresponding vertical transition absorptions by 0.25 eV for the 1^1B_{1g},

1.26 eV for 1^3B_{1g}, 0.25 eV for 1^1B_{2g}, 0.10 eV for 1^3B_{2g}, 1.11 eV for 1^1B_{3g}, 1.25 eV for 1^3B_{3g}, 1.24 eV for 1^1B_{2u}, 0.92 eV for 1^3B_{2u}, 0.22 eV for 1^1B_{3u}, 0.09 eV for 1^3B_{3u}, and 1.74 eV for 2^1A_g. This suggests that the ground state potential energy surface (PES) has a smaller low–energy domain than does those of the excited states; a similar observation was made for F_2CN_2 [2].

Summary

GVVPT2 calculations using the cc-pVDZ basis set have been used to investigate the equilibrium geometries, adiabatic energy differences and absorption and emission energies of several low-lying electronic states of [3,3']bidiazirinylidene (C_2N_4). Additional calculations using the aug-cc-pVTZ basis were performed to assess basis effects on absorption energies. GVVPT2 results for the ground state of C_2N_4 were found to be similar to those of difluorodiazirine (F_2CN_2), which has also been investigated experimentally. It was observed that the GVVPT2 method addressed all the states of interest without encountering mathematical or computational difficulties. Additionally, MP2, MCSCF, QCISD, CCSD and CCSD(T) calculations were performed for the ground state, with results being qualitatively similar to GVVPT2 with the greatest differences occurring for the N–N bond lengths. GVVPT2 N–N bond lengths were greater than those predicted by QCISD (0.016 Å), CCSD (0.017 Å), MCSCF (0.031 Å) and CCSD(T) (0.004 Å) and shorter than predicted by MP2 (0.008 Å), consistent with an earlier study of the related molecule F_2CN_2 [2]. As in the earlier study, particularly good agreement was noted between GVVPT2 and CCSD(T). The results of these calculations show that a balanced treatment of nondynamic and dynamic correlation effects is important for a correct description C_2N_4. Geometry optimization at the GVVPT2/cc-pVTZ level showed

trends similar to that previously observed for F_2CN_2: shorter N–N and C–N bond lengths when compared to the calculation using a smaller basis set (cc-pVDZ). Frequency calculations for this molecule at the SCF, MP2 and MCSCF levels of theory are also similar to those obtained experimentally for F_2CN_2. The NN symmetric and asymmetric stretching frequencies at 1470 cm^{-1} and 1562 cm^{-1} of C_2N_4 are similar to the NN stretching mode of F_2CN_2 with a frequency of 1650 cm^{-1}, which is characteristic of a N=N double bond. The B_{2u} and B_{3g} symmetric and asymmetric CN stretching frequencies of 934.4 cm^{-1} and 995.5 cm^{-1} are similar to the B_2 asymmetric CN stretching frequency in F_2CN_2 at 1091 cm^{-1}. This similarity in their vibrational spectra supports the expectation that they should have electronically and geometrically similar CN_2 rings.

All the calculations of the low-lying excited states confirm the expectation, based on earlier studies of diazirine, of retaining the CN_2 ring when excitation occurs but with the resulting elongation of the N–N bond length compared to that of the ground state geometry. It was found that the 1^1B_{2g} and 1^3B_{2g} states can be described qualitatively by a single excitation within the ring fragments from an N–C–N banana-type bond to a π-antibonding N–N orbital. This electronic transition corresponds to the transition from the 1^1A_1 to the 1^1B_1 and 1^3B_1 excited states in F_2CN_2. The 1^1B_{3u} and 1^3B_{3u} states also correspond to the same transition in F_2CN_2. The average excitation energy to $^{1,3}B_1$ in F_2CN_2 is 2.8 eV at the GVVPT2/cc-pVDZ level, whereas the average excitation energy of the corresponding states in C_2N_4 (i.e., $^{1,3}B_{2g}$ and $^{1,3}B_{3u}$) is 2.7 eV. Because EOM-CCSD calculations give an average value that is somewhat larger (i.e., 4.0 eV for the average of $^1B_{2g}$ and $^1B_{3u}$, further study seems warranted.

The 1^1B_{3g} and 1^3B_{3g} states are both described by a one electron transition within

the ring fragments from a π-bonding N–N orbital to a π-antibonding N–N orbital, which corresponds to the transition from the ground state to the 1^1B_2 and 1^3B_2 excited states in F_2CN_2. The 1^1B_{2u} and 1^3B_{2u} states correspond to the same transition in F_2CN_2, and differ from the 1^1B_{3g} and 1^3B_{3g} states of C_2N_4 in that the symmetric combination of antibonding orbitals is involved rather than the antisymmetric. Most excited states are predicted to be produced with less than 1 eV of excess internal energy (i.e., difference between vertical and adiabatic energies) except for the 2^1A_g (3.19 eV) and 1^1B_{2u} (1.12 eV) states, which is of particular interest since excitations to the latter is spin- and dipole-allowed.

A comparison of geometric parameters, harmonic frequencies and electronic excitation spectrum of the 1^1A_{1g} ground state of C_2N_4 to that of the $^1A_1$ state of F_2CN_2 suggests that C_2N_4 could also be synthesized and characterized. Moreover, the low-lying electronic excitations of C_2N_4, as with F_2CN_2, are located in the CN_2 ring moiety and lead to retention of the ring structure. These common characteristics, and a computed one dimensional approximate dissociation path to $N_2 + C_2N_2$ (barrier ≤ 130 kcal/mol; $\Delta E \leq$ 30.4 kcal/mol), suggest that C_2N_4 may be metastable with respect to its dissociation products $C_2 + 2N_2$. [3,3']bidiazirinylidene, arguably the simplest molecule with multiple CN_2 rings, could be the prototype for new investigations of novel molecules.

GROUND AND LOW-LYING EXCITED ELECTRONIC STATES OF [3,3']BIDIAZIRINYLIDENE (C_2N_4) in C_{2v} symmetry

Introduction

Studies on [3,3']bidiazirinylidene (C_2N_4) continued in which the restriction to D_{2h} symmetry was relaxed to C_{2V} symmetry (Figure 2, Chapter 1). In C_{2v} symmetry, this derivative of diazirine consists of two CN_2 rings of potentially different bond lengths and angles. It is still expected to be high-lying with respect to its dissociation products [2, 15]. To the best of our knowledge, the ground- and low-lying excited electronic states of this [3,3']bidiazirinylidene (C_2N_4) with this symmetry have not yet been characterized either experimentally or theoretically.

The theoretical investigation of this molecule and particularly its excited electronic states is a vital computational challenge and, like other diazirine derivatives, requires high-level methods that can allow a balanced treatment of dynamical and nondynamical electron correlation. A variant of multireference perturbation theory, the second-order generalized Van Vleck perturbation theory (GVVPT2) [1], has proved to be accurate in describing the ground and excited electronic states of closely related polyatomic molecules, like difluorodiazirine (F_2CN_2) [2], difluorodioxirane (CF_2O_2) [136] and a previous investigation of [3,3']bidiazirinylidene when only states of D_{2h} symmetry were considered [134]. The GVVPT2 method has also been shown to describe well other particularly difficult excited state electronic structures, such as disulfur monoxide (S_2O) [137] and the azabenzenes [138], for which balanced treatments of dynamical and nondynamical correlation effects is also a need. Its results are in close agreement to those of coupled cluster with single and double excitations (CCSD) [72], or even CCSD(T) [4], when CCSD is applicable, and GVVPT2 is more widely applicable

than single reference CCSD. For many problems, GVVPT2 is a reliable alternative to the significantly more computationally intensive multireference configuration interaction with single and double excitations (MRCISD) method.

In this latter part of Chapter III, the C_{2v} symmetry 1^1A_1 ground state of C_2N_4 has been investigated at the GVVPT2 level of theory using the cc–pVDZ basis set [139] as implemented in the local electronic structure suite named as UNDMOL. Several low-lying excited states of C_{2v} symmetry (2^1A_1, 1^1A_2, 1^3A_2, 1^1B_1, 1^3B_1, 1^1B_2, and 1^3B_2) were also studied at the GVVPT2/cc-pVDZ level of theory. Based on previous work for this molecule in D_{2h} symmetry [134], and other three-membered ring compounds, low-lying excited states are expected to be produced by excitations located in the CN_2 fragments with the retention of the diazirine ring moiety but leading to elongation of the C–N and/or N–N bond lengths. The energies of the ground and low-lying excited states are expected to be equal or lower than those of C_2N_4 in the D_{2h} symmetry, because of possible relaxation in symmetry constraints. Further insight into the states is acquired by studying harmonic frequencies of the equilibrium geometries of the ground and low-lying excited states in C_{2v} symmetry. The studies of the ground-state geometry were also performed at other levels of theory: second-order Møller-Plesset perturbation theory (MP2); coupled cluster with single and double excitations (CCSD); and quadratic configuration interaction with single and double excitations (QCISD) [4]. These calculations were performed using the Gaussian 03 program [141]. CCSD(T) [4] calculations on the ground state and additional calculations to characterize the excited states using EOM-CCSD [50, 142, 143] were done using GAMESS [144, 145].

This part of Chapter III is divided into three additional sections. In Section 2, an overview of computational features, including a detailed account of an incomplete model space constructed using the macroconfiguration approach [96], is done. Section 3 presents the results of our study and a discussion that includes a comparison of features of C_2N_4 in C_{2v} symmetry relative to that in D_{2h} symmetry and to those of difluorodiazirine, for which both experimental and theoretical results are available. A final section summarizes the work.

Computational details

All spin and space symmetry allowed configurations generated by single and double excitations from a HF-like reference are included in the model spaces used in this study. The model space was created from excitation from the 15 highest occupied orbitals to the 9 lowest unoccupied valence orbitals. From preliminary single reference studies of the 1^1A_1 ground state, construction of groups of orbitals for MCSCF and subsequent GVVPT2 calculations were done as follows: the fifteen highest occupied orbitals were divided into three subgroups (G_1, G_2 and G_3) involving eight, five and two orbitals, respectively. The first subgroup G_1 includes the eight lowest orbitals: G_1 = ($5a_1$, $6a_1$, $7a_1$, $3b_2$, $4b_2$, $8a_1$, $9a_1$, $1b_1$). The second subgroup, G_2, involves the next five valence orbitals: G_2 = ($10a_1$, $2b_1$, $11a_1$, $5b_2$, $6b_2$). And the third subgroup, G_3, involves the highest lying valence orbital and the lowest virtual orbital: G_3= ($3b_1$, $1a_2$). The nine lowest virtual orbitals are also divided into two subgroups (V_1 and V_2) involving five and four orbitals, respectively: V_1 = ($12a_1$, $13a_1$, $2a_2$, $4b_1$, $7b_2$) and V_2 = ($14a_1$, $8b_2$, $9b_2$, $10b_2$). Figure 16 shows the orbitals that have proven to be qualitatively significant for the low-lying excited states. On the basis of this partitioning of the high–lying

occupied and low–lying unoccupied orbitals, thirty five macroconfigurations describing single and double excitations from G_1, G_2 and G_3 to V_1 and V_2 were created.

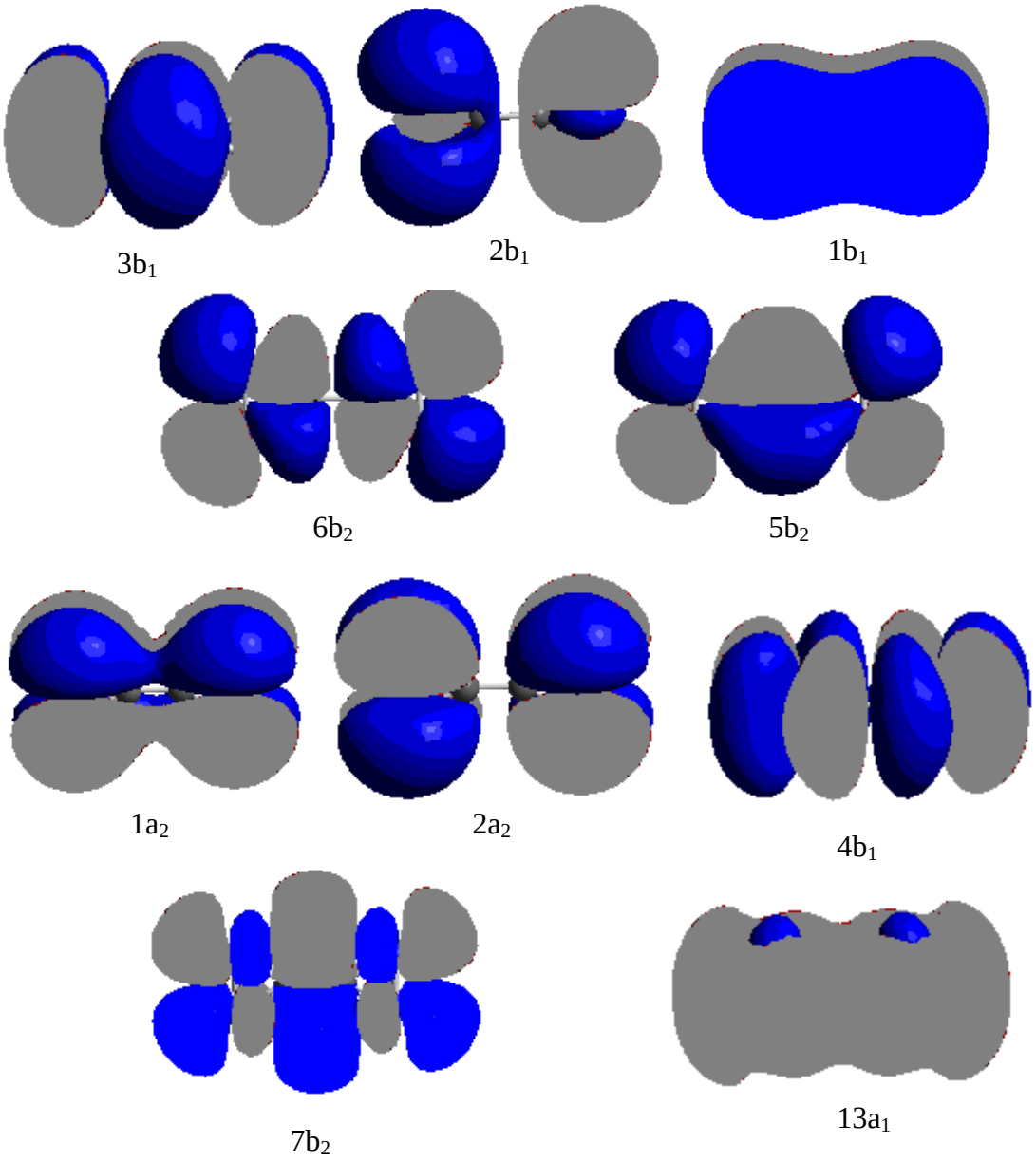

Figure 16. [3,3’] bidiazirinylidene in C_{2v} symmetry 3-D plots of orbitals of groups G_2 and some of V_1.

The list of macroconfigurations determining the incomplete model space used includes: the closed–shell macroconfiguration describing the ground state,

$(G_1)^{16}\,(G_2)^{10}\,(G_3)^{2}\,(V_1)^{0}\,(V_2)^{0}$,

macroconfigurations describing all single excitations from G_1, G_2 or G_3 to V_1 or V_2,

$(G_1)^{16}\,(G_2)^{10}\,(G_3)^{1}\,(V_1)^{1}\,(V_2)^{0}$, $(G_1)^{16}\,(G_2)^{9}\,(G_3)^{2}\,(V_1)^{0}\,(V_2)^{1}$,

$(G_1)^{16}\,(G_2)^{10}\,(G_3)^{1}\,(V_1)^{0}\,(V_2)^{1}$, $(G_1)^{16}\,(G_2)^{9}\,(G_3)^{1}\,(V_1)^{2}\,(V_2)^{0}$,

$(G_1)^{16}\,(G_2)^{9}\,(G_3)^{3}\,(V_1)^{0}\,(V_2)^{0}$, $(G_1)^{16}\,(G_2)^{9}\,(G_3)^{2}\,(V_1)^{1}\,(V_2)^{0}$, and

macroconfigurations describing all double excitations from G_1 ,G_2 and/or G_3 to V_1 and/or V_2,

$(G_1)^{16}\,(G_2)^{10}\,(G_3)^{0}\,(V_1)^{2}\,(V_2)^{0}$, $(G_1)^{16}\,(G_2)^{10}\,(G_3)^{0}\,(V_1)^{1}\,(V_2)^{1}$,

$(G_1)^{15}\,(G_2)^{10}\,(G_3)^{3}\,(V_1)^{0}\,(V_2)^{0}$, $(G_1)^{16}\,(G_2)^{10}\,(G_3)^{0}\,(V_1)^{0}\,(V_2)^{2}$,

$(G_1)^{15}\,(G_2)^{10}\,(G_3)^{2}\,(V_1)^{1}(V_2)^{0}$, $(G_1)^{16}\,(G_2)^{9}\,(G_3)^{1}\,(V_1)^{1}\,(V_2)^{1}$,

$(G_1)^{15}\,(G_2)^{10}\,(G_3)^{2}\,(V_1)^{0}\,(V_2)^{1}$, $(G_1)^{16}\,(G_2)^{9}\,(G_3)^{1}\,(V_1)^{0}\,(V_2)^{2}$,

$(G_1)^{15}\,(G_2)^{10}\,(G_3)^{1}\,(V_1)^{2}\,(V_2)^{0}$, $(G_1)^{16}\,(G_2)^{8}\,(G_3)^{4}\,(V_1)^{0}\,(V_2)^{0}$,

$(G_1)^{15}\,(G_2)^{9}\,(G_3)^{4}\,(V_1)^{0}\,(V_2)^{0}$, $(G_1)^{16}\,(G_2)^{8}\,(G_3)^{3}\,(V_1)^{1}\,(V_2)^{0}$,

$(G_1)^{15}\,(G_2)^{9}\,(G_3)^{3}\,(V_1)^{1}\,(V_2)^{0}$, $(G_1)^{16}\,(G_2)^{8}\,(G_3)^{3}\,(V_1)^{0}\,(V_2)^{1}$,

$(G_1)^{15}\,(G_2)^{9}\,(G_3)^{3}\,(V_1)^{0}\,(V_2)^{1}$, $(G_1)^{16}\,(G_2)^{8}\,(G_3)^{2}\,(V_1)^{2}\,(V_2)^{0}$,

$(G_1)^{15}\,(G_2)^{9}\,(G_3)^{2}\,(V_1)^{2}\,(V_2)^{0}$, $(G_1)^{16}\,(G_2)^{8}\,(G_3)^{2}\,(V_1)^{1}\,(V_2)^{1}$,

$(G_1)^{15}\,(G_2)^{9}\,(G_3)^{2}\,(V_1)^{1}\,(V_2)^{1}$, $(G_1)^{16}\,(G_2)^{8}\,(G_3)^{2}\,(V_1)^{0}\,(V_2)^{2}$,

$(G_1)^{15}\,(G_2)^{9}\,(G_3)^{2}\,(V_1)^{0}\,(V_2)^{2}$, $(G_1)^{15}\,(G_2)^{10}\,(G_3)^{1}\,(V_1)^{0}\,(V_2)^{2}$,

$(G_1)^{14}\,(G_2)^{10}\,(G_3)^{4}\,(V_1)^{0}\,(V_2)^{0}$, $(G_1)^{15}\,(G_2)^{10}\,(G_3)^{1}\,(V_1)^{1}\,(V_2)^{1}$,

$(G_1)^{14}\,(G_2)^{10}\,(G_3)^{3}\,(V_1)^{1}\,(V_2)^{0}$, $(G_1)^{14}\,(G_2)^{10}\,(G_3)^{3}\,(V_1)^{0}\,(V_2)^{1}$,

$(G_1)^{14}\,(G_2)^{10}\,(G_3)^{2}\,(V_1)^{2}\,(V_2)^{0}$, $(G_1)^{14}\,(G_2)^{10}\,(G_3)^{2}\,(V_1)^{1}\,(V_2)^{1}$,

$(G_1)^{14}\,(G_2)^{10}\,(G_3)^{2}\,(V_1)^{0}\,(V_2)^{2}$.

The ground state has $^1A_1$ symmetry and its model space is spanned by 9943 configuration state functions (CSFs) created by 4396 configurations. The external space is spanned by 1,293,102,969 CSFs (1,181,175,072 configurations) for the cc-pVDZ basis set. The dimensions of the model space for excited states were as follows: for the $^1A_2$ and $^3A_2$ states, their model spaces were spanned by 8161 CSFs and 12881 CSFs respectively (created by 3441 configurations); for the $^1B_1$ excited state the model space were spanned by 3444 CSFs (created by 1426 configurations); for the $^3B_1$ state the model space were spanned by 6446 CSFs (created by 1762 configurations), the model spaces for both 1^1B_2 and 1^3B_2 states were spanned by 9807 CSFs and 15299 CSFs respectively (created by 4315 configurations). The external space dimension for the triplet excited states increased significantly (for example, 2.3 billion CSFs), but those for the singlet excited states remained approximately the same as that of the ground state (approximately 1.3 billion CSFs). The dimension of the external space of C_2N_4 in C_{2v} symmetry is much larger than that for the D_{2h} symmetry. Our current GUGA-based GVVPT2 program [135], can perform the calculations in reasonable time; e.g., a typical

GVVPT2 calculation takes 27.5 minute for 1.4 billion total CSFs and 4396 model CSFs on a 2.0 GHz dual-core AMD Opteron processor 2212.

Table 6. Comparison of optimized geometries of the ground state of C_2N_4 in C_{2v} symmetry.

cc-pVDZ						
	MP2	MCSCF	CCSD	QCISD	CCSD(T)	GVVPT2
R_{CC} (Å)	1.300	1.297	1.301	1.302	1.270	1.297
$R_{CN(1)}$ (Å) $R_{CN(2)}$ (Å)	1.433	1.422 1.420	1.429	1.429	1.438 1.438	1.422 1.435
$R_{NN(1)}$ (Å) $R_{NN(2)}$ (Å)	1.290	1.265 1.253	1.264	1.266	1.285 1.285	1.265 1.281
∠NCN (°)	53.5	52.8 52.3	52.5	52.6	53.1	52.8 53.0
∠CNN (°)	63.3	63.6 63.8	63.7	63.7	63.5	63.6 63.5

Table 7. Comparison of optimized geometries of the ground state of C_2N_4 in C_{2v} symmetry to that in D_{2h} symmetry and F_2CN_2.

	GVVPT2/cc-pVDZ		
	C_2N_4		F_2CN_2[a]
	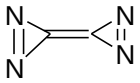 C_{2v}	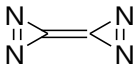 D_{2h}	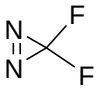 C_{2v}
R_{CC} (Å)	1.297	1.303	-
$R_{CN(1)}$ (Å) $R_{CN(2)}$ (Å)	1.422 1.435	1.433	1.421
$R_{NN(1)}$ (Å) $R_{NN(2)}$ (Å)	1.265 1.281	1.282	1.288
$\angle NCN_{(1)}$ (°) $\angle NCN_{(2)}$ (°)	52.8 53.0	53.1	53.9

[a] Ref. [2].

Electronic and molecular structures

GVVPT2 calculations for the ground state of [3,3']bidiazirinylidene show that the leading configuration is $\cdots (4b_2)^2(10a_1)^2(11a_1)^2(2b_1)^2(5b_2)^2(6b_2)^2(3b_1)^2\cdots$ with an amplitude of 0.851. This amplitude is smaller than it is for the MCSCF calculation (i.e., leading configuration: 0.92), similar results were obtained for the excited states, demonstrating the effect of dynamic electron correlation on the reference configurations. The next most important configuration can be described as a $3b_1^2 \Rightarrow 1a_2^2$ two-electron excitation relative to the closed shell reference. Qualitatively the excitation is from a π-

bonding N–N orbital to a π-antibonding orbital, having amplitude of 0.159. Insight into the short C–C and N–N bonds compared to those of D_{2h} symmetry (Table 2 in Ref. 134) stems from the large contribution of these configurations. The considerable multiconfigurational nature of zero-order wavefunctions corroborates the expectation that the [3,3']bidiazirinylidene molecule, particularly in C_{2v} symmetry, is a difficult problem that requires a good method to describe dynamic and nondynamic electron correlation.

Optimization of the geometry of the ground state of C_2N_4 molecule in C_{2v} symmetry was performed with the model space described in Section 2 at the GVVPT2 level of theory and at other levels of theory, MP2, CCSD, CCSD(T) and QCISD, using the cc-pVDZ basis set. The optimized structural parameters for the ground state of the C_2N_4 molecule obtained at the GVVPT2 level were compared to those for the other methods. Five parameters were obtained after the GVVPT2 calculations were performed as opposed to three parameters optimized for C_2N_4 at MP2, CCSD, CCSD(T) and QCISD levels of theory at D_{2h} symmetry [134]. The GVVPT2 results show close agreement to those for CCSD, CCSD(T), QCISD, and MP2 levels of theory (Table 6). The R_{CC} bond length is about 0.004 Å and 0.005 Å shorter than those for the CCSD and QCISD methods respectively, 0.003 Å shorter than that for the MP2 method, and 0.027 Å longer than that of CCSD(T); the $R_{CN(1)}$ bond length is 0.007 Å shorter than those using CCSD and QCISD, 0.011 Å and 0.016 Å shorter than that for the MP2 and CCSD(T) result respectively, but the $R_{CN(2)}$ bond length is 0.006 Å longer than those using CCSD and QCISD, and 0.002 Å longer than that for the MP2, but 0.003 Å shorter than the CCSD(T) result. For the $R_{NN(1)}$ bond length, the GVVPT2 result is 0.001 Å, 0.025 Å and 0.020 Å shorter than those for QCISD, MP2, and CCSD(T) results respectively, but it is 0.001 Å

longer than that for CCSD; the $R_{NN(2)}$ bond length is 0.017 Å and 0.015 Å longer than that for CCSD and QCISD respectively, but 0.009 Å and 0.004 Å shorter than that for the MP2 and CCSD(T) results respectively. The $\angle$NCN(1) angle predicted by GVVPT2 differs by only 0.3° and 0.2° and the $\angle$NCN(2) angle is 0.5° and 0.4° larger than that for the CCSD and QCISD methods, but, as shown in Table 6, the $\angle$NCN(1) angle differ by 0.7° and 0.3° and the $\angle$NCN(2) angle is 0.5° and 0.1° smaller than that of MP2 and CCSD(T) results respectively. The $\angle$CNN (1 and 2) angles are 0.1 and 0.2 smaller than those of CCSD and QCISD, and are 0.3° and 0.2° larger than that of MP2, and 0.1° larger than that for CCSD(T).

Experimental results for C_2N_4 are not available. To further understand the results of the calculations, the optimized parameters for C_2N_4 in this symmetry are compared to those of this same molecule in D_{2h} symmetry (see Table 1 in Ref. 134), and to those of F_2CN_2 which has been investigated both experimentally and theoretically (see Table 1 in Ref. 2). R_{CC}, R_{CN} and R_{NN} bond lengths and the $\angle$NCN angle obtained at the GVVPT2 level using the cc-pVDZ basis sets for the C_2N_4 molecule in C_{2v} symmetry are close to those obtained in D_{2h} symmetry (which agree with those for F_2CN_2), as shown in Table 7. R_{CC}, $R_{CN(1)}$ and $R_{NN(1)}$ bond lengths for C_2N_4 in C_{2v} symmetry are only 0.006 Å, 0.011 Å and 0.017 Å shorter and the $R_{CN(2)}$ and $R_{NN(2)}$ bond lengths are 0.002 Å and 0.001 Å longer than those using D_{2h} symmetry, respectively. The $\angle$NCN(1) and $\angle$NCN(2) angles of C_2N_4 in C_{2v} are 0.3° and 0.1° smaller than that for D_{2h} symmetry. These results show that the electronic structure of the [3,3']bidiazirinylidene molecule, when allowed to relax to C_{2v} symmetry, is very similar to the results in D_{2h} symmetry, as expected.

Frequency calculations of the C_2N_4 molecule at the MCSCF level of theory with the cc-pVDZ basis for the ground and the low-lying excited states are given in Table 8. [3,3']bidiazirinylidene molecule is seen to be a minimum at this level of theory.

Table 8. Vibrational frequencies (cm^{-1}) of the ground and low-lying excited states of C_2N_4 in the C_{2v} at the MCSCF/cc-pVDZ levels of theory.

vibration	1^1A_1	1^1A_2	1^3A_2	1^1B_1	1^3B_1	1^1B_2	1^3B_2
υ_1 (B_2)	228.2	168.7	157.0	265.8	1.42	147.1	199.0
υ_2 (B_1)	293.2	279.2	247.5	314.0	2.87	217.8	267.1
υ_3 (B_1)	357.4	282.2	314.8	365.7	318.1	293.6	316.5
υ_4 (A_2)	412.6	403.1	442.2	458.8	330.1	327.8	446.7
υ_5 (B_2)	509.5	446.6	532.0	512.1	482.4	437.1	535.8
υ_6 (A_1)	616.0	575.0	563.8	573.1	565.3	525.9	537.9
υ_7 (B_2)	939.6	704.9	803.1	790.4	623.6	606.8	747.4
υ_8(B_2)	1006	1023	904.6	862.2	917.1	888.7	920.8
υ_9 (A_1)	1150	1247	1064	1024	1042	1102	1053
υ_{10} (A_1)	1477	1303	1266	1270	1658	1238	1278
υ_{11}(A_1)	1611	1642	1518	1718	1698	1581	1504
υ_{12}(A_1)	2117	2125	1871	2155	2038	1903	1840

In the 1^1A_2 excited state, there are three major configurations relating this state to the closed-shell reference. They can be described as a two-electron excitation $6b_2\ 3b_1$ => $1a_2\ 2a_2$ with amplitude of 0.803, and two three-electron excitations $1b_1\ 6b_2\ 3b_1$ => $1a_2\ 2a_2\ 4b_1$, and $5b_2\ 6b_2\ 3b_1$ => $1a_2\ 2a_2\ 7b_2$ having amplitudes 0.159 and 0.102 respectively (Figure 17). These correspond to excitations from antisymmetric, banana-type, three-

centered N–C–N bonding orbitals ($5b_2$ and $6b_2$) and π-bonding N–N orbitals ($1b_1$ and $3b_1$) to two π-antibonding N–N orbitals ($1a_2$ and $2a_2$), and one antisymmetric, banana-type, three-centered N–C–N antibonding orbital ($7b_2$). The result is elongation of the $R_{CC(1)}$, $R_{NN(1)}$ and $R_{NN(2)}$ bond lengths by +0.048 Å, +0.212 Å and +0.011 Å respectively. The $R_{CN(1)}$ and $R_{CN(2)}$ bond lengths are shortened by 0.097 Å and 0.032 Å (Table 9).

The triplet state (1^3A_2) is more highly multiconfigurational than the singlet state. It has five dominant configurations relating this state to the ground state. Three of the excitations can be described in terms of the $6b_2\ 3b_1 \Rightarrow 1a_2\ 13a_1$ two-electron excitation. They differ only with respect to their electron spins. Their amplitudes are 0.628, 0.423 and 0.184 for the first, second and third leading configurations. The fourth and fifth leading configurations and their amplitudes are

$5b_2\ 6b_2\ 3b_1 \Rightarrow 1a_2\ 4b_1\ 13a_1$ (0.134)

$2b_1\ 6b_2\ 3b_1 \Rightarrow 1a_2\ 2a_2\ 13a_1$ (0.105),

and can be described as three-electron excitations. All five major configurations correspond to excitations from antisymmetric, banana-type, three-centered N–C–N bonding orbitals ($5b_2$ and $6b_2$) and π-bonding N–N orbitals ($2b_1$ and $3b_1$) to π-antibonding C–N and N–N orbitals ($1a_2$, $2a_2$ and $13a_1$) (Figure 17). The effect of these excitations is elongation of the $R_{CC(1)}$, $R_{NN(1)}$ and $R_{NN(2)}$ bond lengths by +0.076 Å, +0.288 Å and +0.023 Å respectively and shortening of the $R_{CN(1)}$ and $R_{CN(2)}$ bond lengths by 0.078 Å and 0.036 Å. These excitations also lead to a great increase in one of the N–C–N angles (+15° and +1.8° for angles 1 and 2 for the singlet, +17.8° and 2.5° for the angles 1 and 2 for the triplet) with respect to the ground state (Table 9).

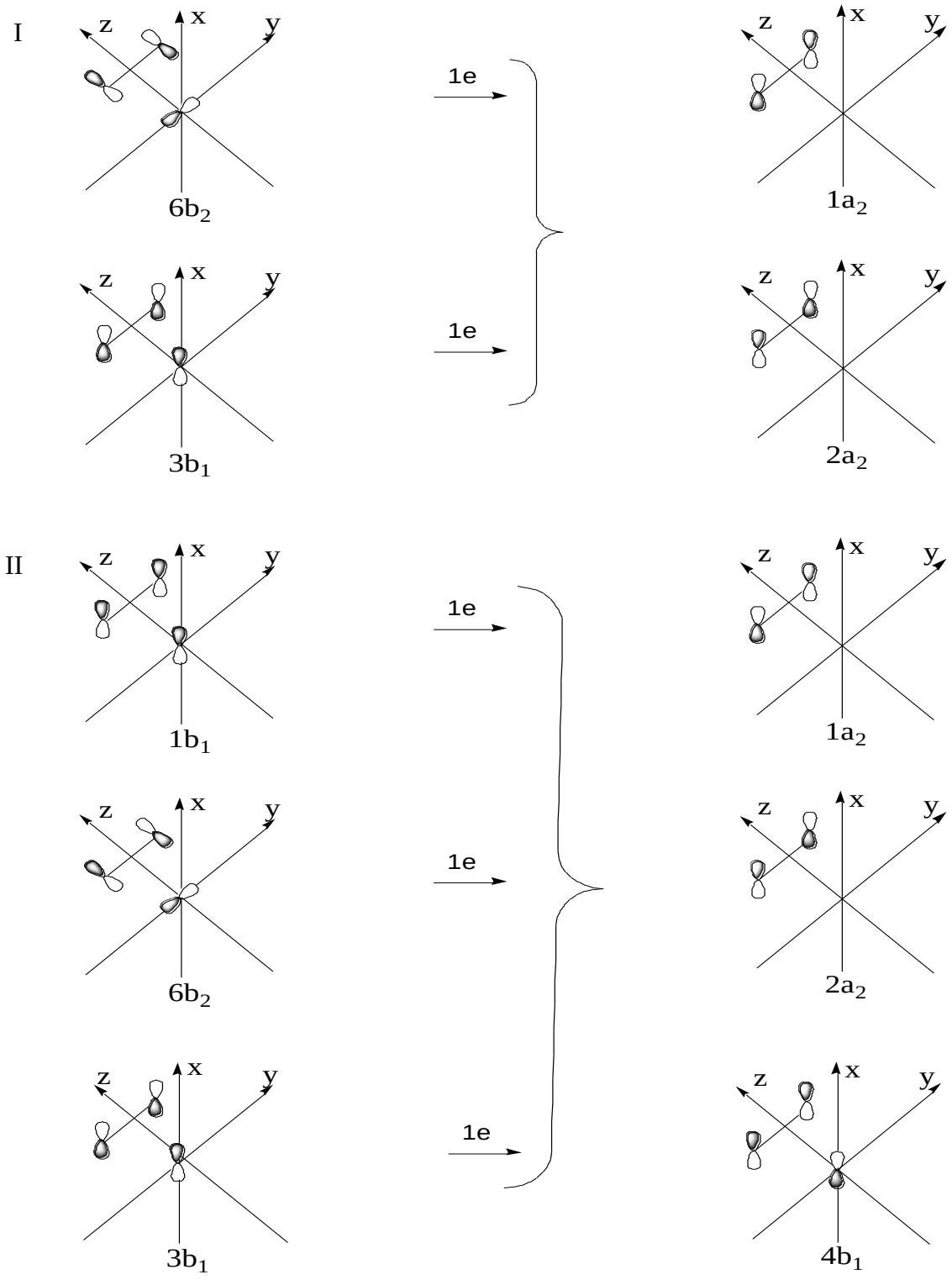

Figure 17. The leading excitations for the $1^{1,3}A_2$ excited states of C_2N_4

Figure 17. cont.

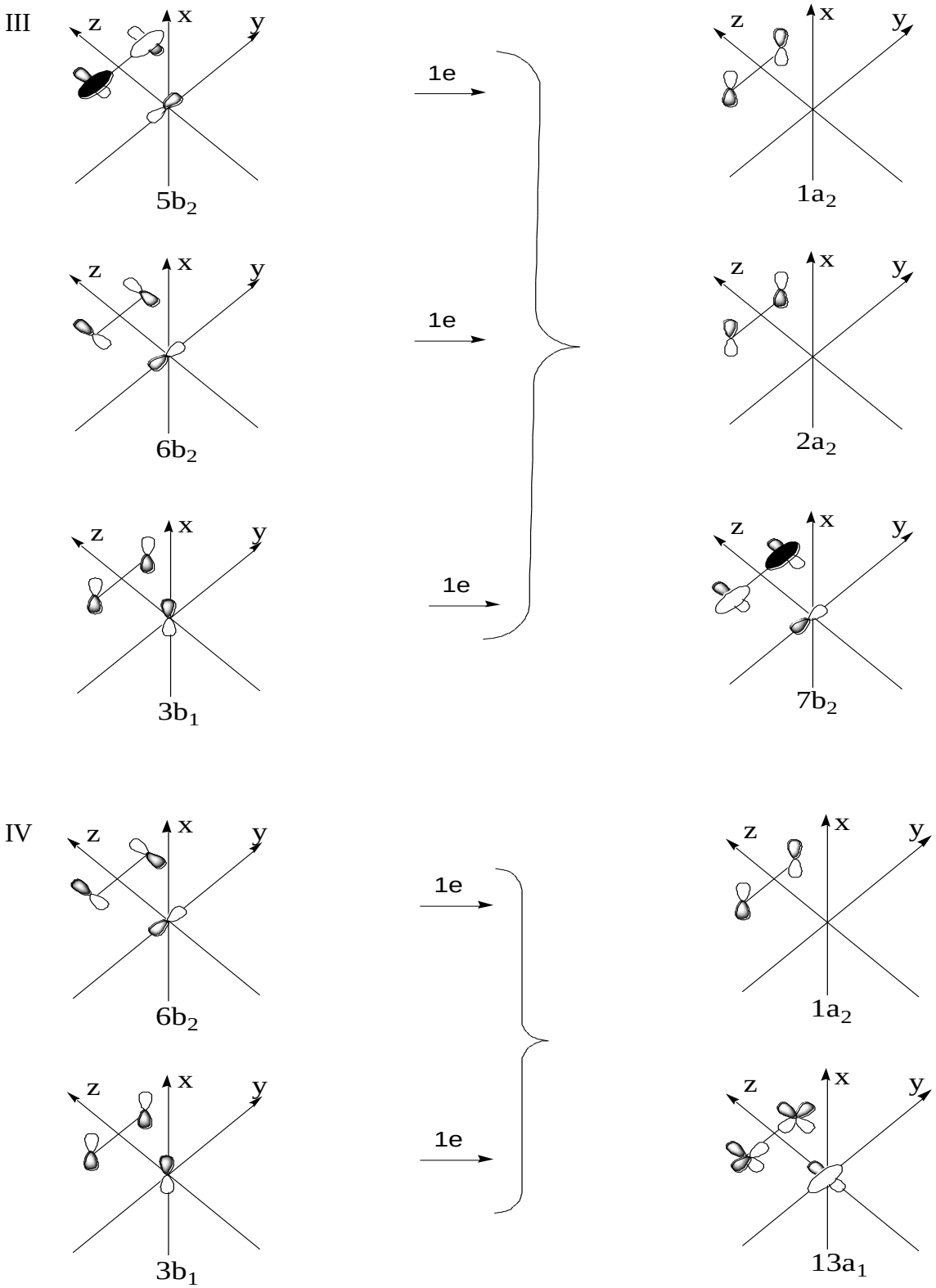

Figure 17. cont.

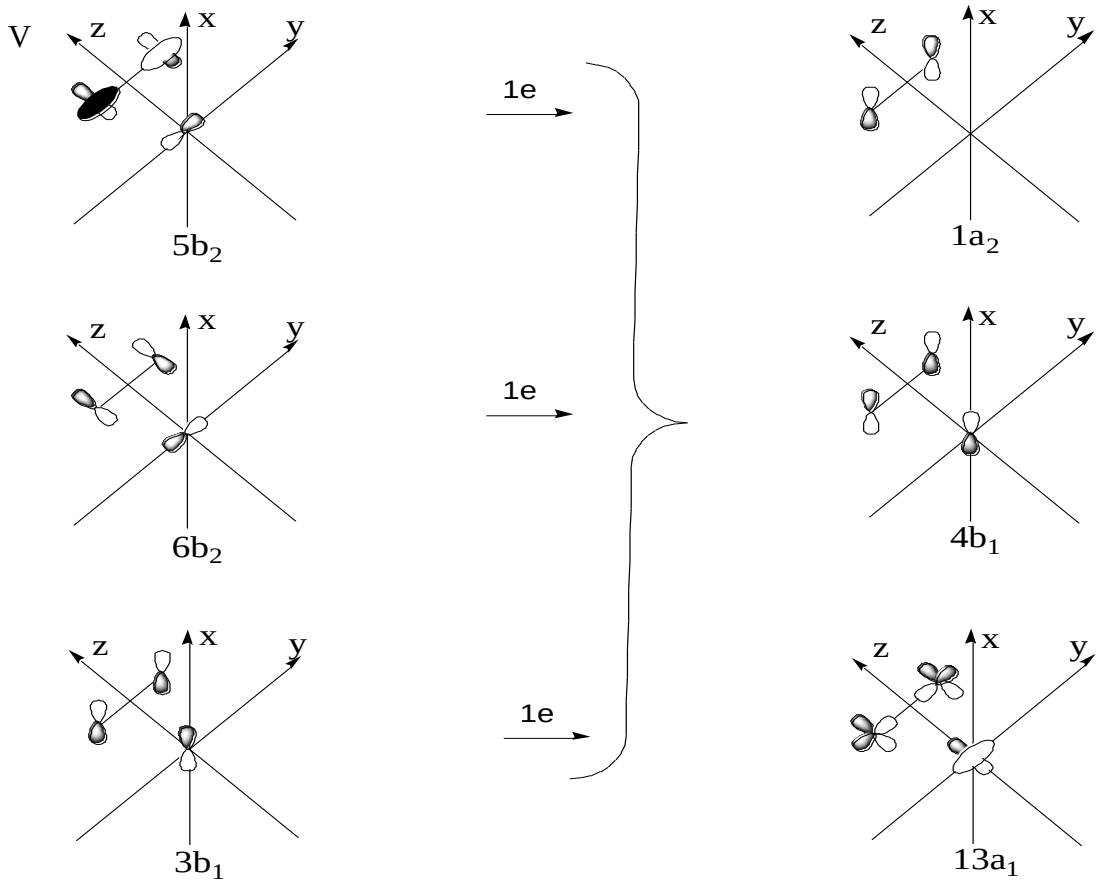

Table 9. GVVPT2/cc-pVDZ-optimized geometries of the excited states of C_2N_4 in C_{2v} symmetry.

	2^1A_2	1^1B_1	1^3B_1	1^1B_2	1^3B_2	1^1A_2	1^3A_2	1^1A_1
R_{CC} (Å)	1.391	1.279	1.270	1.414	1.370	1.345	1.373	1. 297
$R_{CN(1)}$ (Å)	1.361	1.462	1.494	1.417	1.415	1.325	1.344	1.422
$R_{CN(2)}$ (Å)	1.360	1.452	1.466	1.323	1.346	1.403	1.399	1.435
$R_{NN(1)}$ (Å)	1.488	1.317	1.257	1.296	1.295	1.477	1.553	1. 265
$R_{NN(2)}$ (Å)	1.486	1.220	1.343	1.577	1.603	1.292	1.304	1.281
∠NCN(1)(°)	56.9	49.7	49.7	54.5	54.5	67.8	70.6	52.8
∠NCN(2)(°)	56.9	53.6	54.5	72.4	73.1	54.9	55.6	53.1
∠CNN(1)(°)	66.3	65.3	65.1	62.8	62.8	56.1	54.7	63.6
∠CNN(2)(°)	66.2	63.2	62.8	53.8	53.5	62.6	62.2	63.5

Unlike the situation for the A_1 and A_2 states, the leading configuration of the singlet and triplet B_1 states are the same. Both have two leading configurations relating them to the ground state. They can be described as the one-electron excitation $6b_2 \Rightarrow 1a_2$ and the three-electron excitations $6b_2\ 3b_1^2 \Rightarrow 1a_2\ 2a_2^2$ (Figure 18). The amplitudes of these leading configurations for the 1^1B_1 state are 0.839 and 0.118 and for the 1^3B_1 state are 0.842 and 0.121. These excitations are from the antisymmetric, banana-type, three-centered N–C–N bonding orbital ($6b_2$) and π-bonding N–N orbital ($3b_1$) to π-antibonding N–N orbitals ($1a_2$ and $2a_2$). Both 1^1B_1 and 1^3B_1 excitations lead to the elongation of one of the N–N bonds and shortening of the other N–N bond. The C–N bonds all increased in length but both excitations lead to shortening of the C–C bond (Table 9). This observation is in agreement with experimental and theoretical results obtained for the electronic transition from the 1^1A_1 to the 1^1B_1 and 1^3B_1 excited states of the F_2CN_2

molecule [2]. GVVPT2 calculations for C_2N_4 in the 1^3B_1 state predict that the N–N bond length increases by +0.062 Å and the C–C bond decreases by 0.027 Å relative to the ground state. This is quite similar to the corresponding changes in F_2CN_2: increment of +0.031 Å (GVVPT2/ccpVDZ), +0.038 Å (experimental) [2] in the N–N bond length. The result is also in agreement to that obtained for C_2N_4 in the D_{2h} symmetry [134].

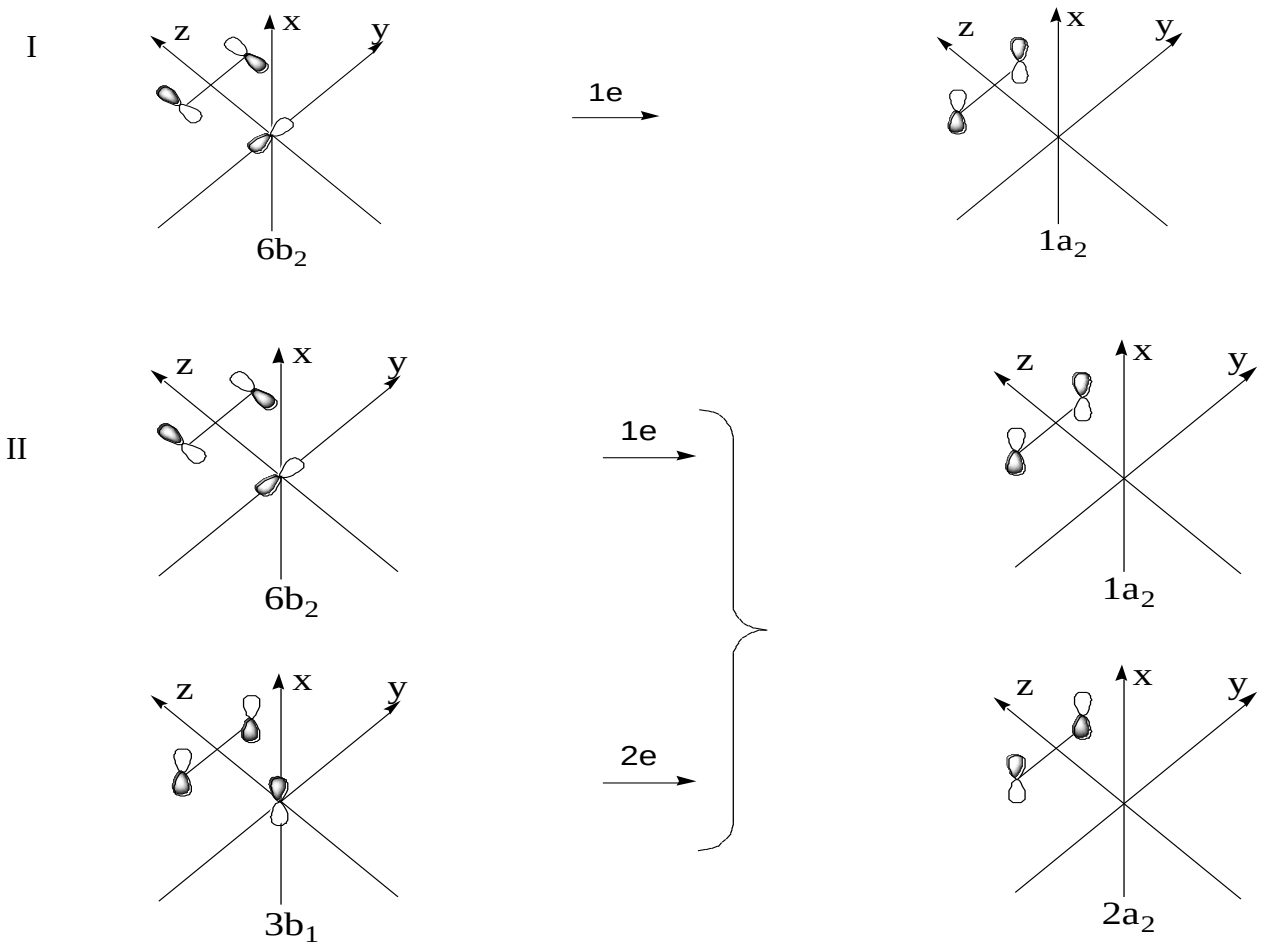

Figure 17. The leading excitations for the 1 $^{1,3}B_1$ excited state of C_2N_4.

The 1^1B_2 and 1^3B_2 excited states of C_2N_4 are not as multiconfigurational as the other states. Their leading configuration can be described as a $3b_1$ => $1a_2$ single excitation, relative to the closed-shell reference (Figure 19). The amplitudes for these excitations are 0.858 for the singlet state (1^1B_2) and 0.863 for the triplet state. Qualitatively, this is an excitation from a π-bonding N–N orbital ($3b_1$) to a π-antibonding N–N orbital ($1a_2$), leading to increases in both R_{NN} bonds by +0.031 Å and +0.296 Å for the 1^1B_2 state and +0.030 Å and +0.322 Å for the 1^3B_2 state (Table 9). Corresponding electronic transitions for the F_2CN_2 molecule are from the 1^1A_1 to the 1^1B_2 and 1^3B_2 excited states [2]. These large increases in the N–N bond length also results in a large increase in the N–C–N angles (+1.7° and 19.3° for the singlet, +1.7° and 20.0° for triplet) with respect to the ground state. Similar results were obtained for this molecule in the D_{2h} symmetry [134].

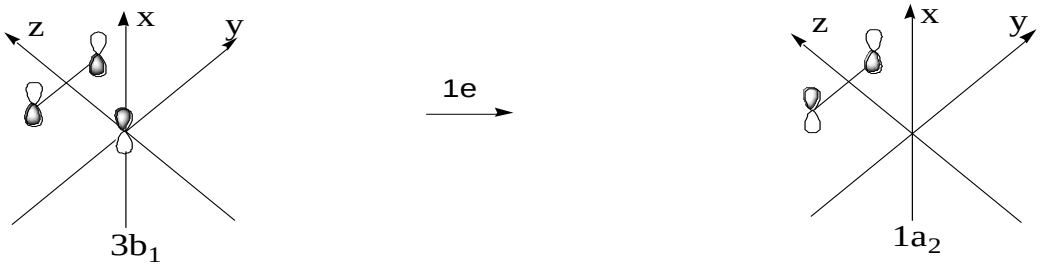

Figure 18. The leading excitations for the $1\ ^{1,3}B_2$ excited state of C_2N_4.

The 2^1A_1 excited state is highly multiconfigurational. The leading configurations of this state are: the closed-shell reference configuration with amplitude 0.288 and three two-electron excitations $3b_1^2$ => $1a_2^2$ with amplitude 0.713, $3b_1^2$ => $2a_2^2$ with amplitude 0.325 and $2b_1\ 3b_1$ => $1a_2\ 2a_2$ having amplitude 0.131 (Figure 20). This corresponds to

excitation from the weakly π-bonding N–N orbitals ($2b_1$ and $3b^2_1$) to the π-antibonding N–N orbital ($1a_2$ and $2a_2$). The effect of these excitations is elongation of the $R_{CC(1)}$, $R_{NN(1)}$ and $R_{NN(2)}$ bond lengths by +0.094 Å, +0.223 Å and +0.205 Å respectively and the shortening of the $R_{CN(1)}$ and $R_{CN(2)}$ bond lengths by 0.061 Å and 0.075 Å (Table 9).

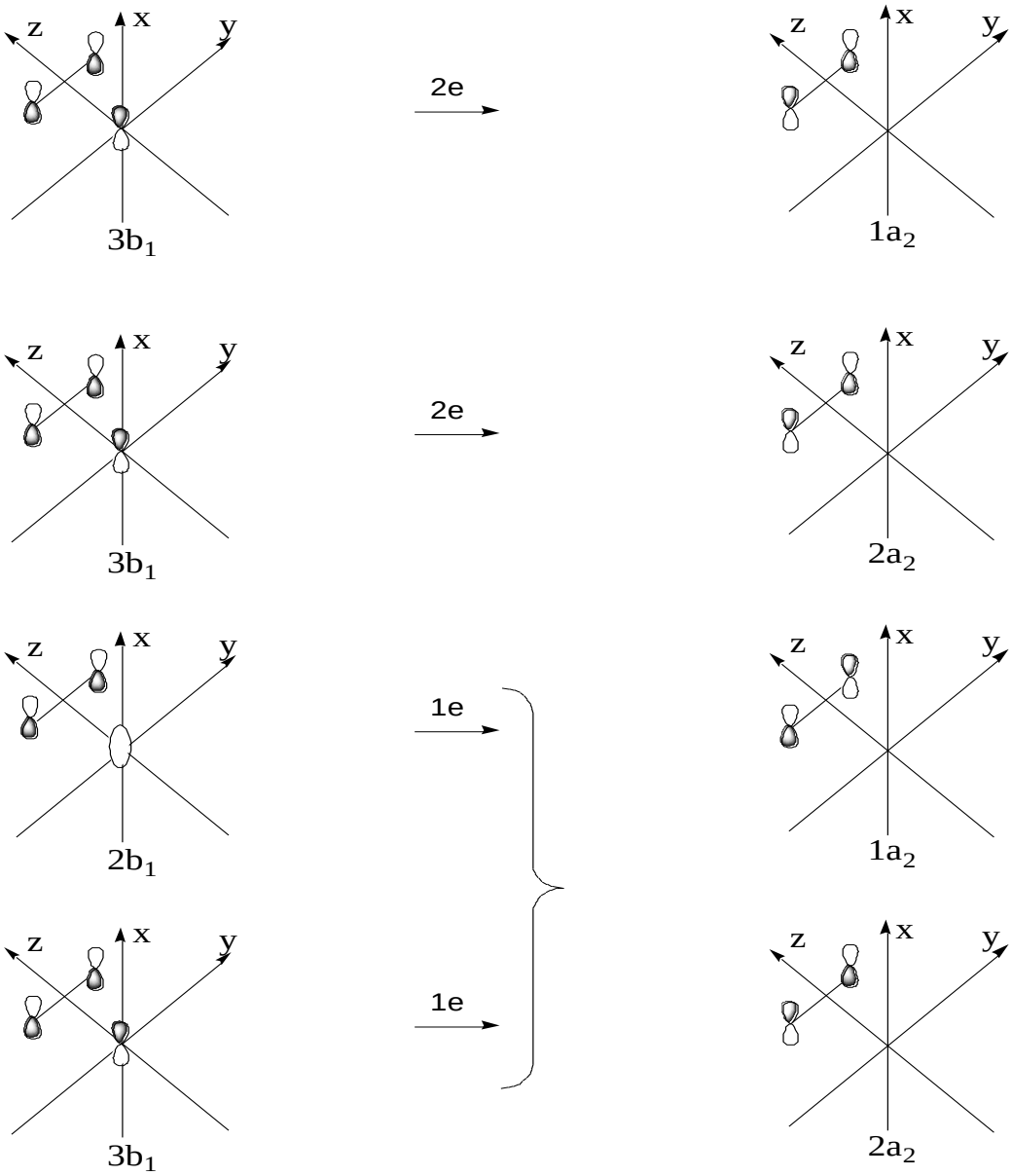

Figure 19. The leading excitation for the 2 $^1A_1$ excited state of C_2N_4.

The GVVPT2/cc-pVDZ level of theory was used to calculate the vertical and adiabatic excitation energies of C_2N_4. In Figure 21, vertical and adiabatic excitation energies of the low-lying excited states with respect to the ground state are given. The calculations show that the vertical excitation to the 1^3B_2 triplet state has the lowest energy (2.54 eV). This excitation is a spin-symmetry forbidden but dipole-allowed transition. The next state is the 1^1B_2 excited state, having excitation energy of 3.01 eV. This low-lying excited state is a spin- and dipole-allowed transition. This is followed by a spin-forbidden but dipole symmetry-allowed excitation to 1^3B_1 at energy of 3.42 eV, followed by a spin- and dipole-allowed transfer to 1^1B_1, with excitation energy of 4.25 eV. A pair of transitions, spin- and dipole-forbidden and spin-allowed transitions to 1^3A_2 and 2^1A_1, with excitation energy of 5.33 eV and 5.57 eV, respectively, is the next lowest transitions. The state with the highest transition is predicted to be the 1^1A_2 having an excitation energies of 6.04 eV.

Vertical excitations using EOM-CCSD//CCSD were performed for all singlet-excited states. The low-lying transition to the 1^1B_1 is predicted to be at 3.97 eV and that to the 1^1B_2 is at 4.26 eV of C_2N_4. These transitions are those characteristic of the diazirine ring (i.e., from the antisymmetric, banana-type, three-centered N–C–N bonding orbital and π-bonding N–N orbital to π-antibonding N–N orbitals). Fedorov et al. [131] recently obtained a vertical excitation energy of 4.27 eV for CH_2N_2, which is comparable to that of the 1^1B_2 state of C_2N_4. Furthermore, a dipole strength of 0.080 and an oscillator strength of 0.0083 were computed for the 1^1B_2 state of C_2N_4; these are comparable to those calculated by Federov et al. [131] i.e., 0.037 and 0.004, respectively for CH_2N_2.

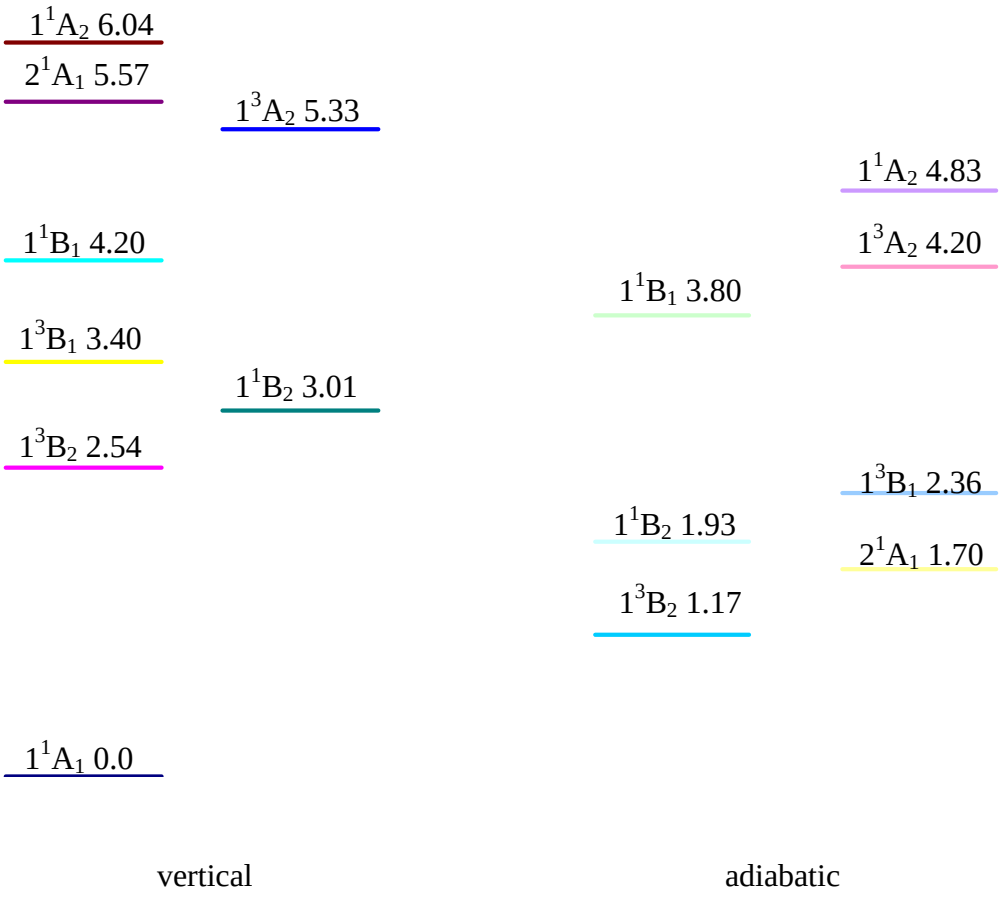

Figure 20. Vertical and adiabatic excitation energies (eV) of low-lying excited states of C_2N_4, calculated at the GVVPT2/cc-pVDZ level of theory.

Optimized geometries were obtained for each low-lying excited state using GVVPT2/cc-pVDZ calculations. Adiabatic excitation energies were calculated from the corresponding optimized geometries. The state with the lowest adiabatic excitation energy is the 1^3B_2 excited state having an adiabatic excitation energy of 1.17 eV, followed by the 2^1A_1 state having adiabatic excitation energy of 1.70 eV. The adiabatic excitation energies for the 1^1B_2, 1^3B_1, 1^1B_1, 1^3A_2, and 1^1A_2 are shown in Table 9.

Differences between the vertical and adiabatic excitation energies are due to substantial differences between the equilibrium geometries of the excited and the ground state geometries. The relaxation energies of the excited states relative to the vertical excitation energy from the 1^1A_1 equilibrium geometry are: 1^1A_2 is stabilized by 1.21 eV, 1^3A_2 by 1.12 eV, 1^1B_1 by 0.39 eV, 1^3B_1 by 1.05 eV, 1^1B_2 by 1.07 eV, 1^3B_2 by 1.37 eV and 2^1A_1 by 3.87 eV. The greatest change is seen for 2^1A_2 (3.87 eV) followed by 1^3B_2 (1.37 eV).

From all the excited state minima, vertical emission energies relative to the 1^1A_1 ground state surface are: 1^1A_2 emits with 4.78 eV, 1^3A_2 with 4.14 eV, 1^1B_1 with 3.84 eV, 1^3B_1 with 2.35 eV, 1^1B_2 with 1.88 eV, 2^1A_2 with 1.42 eV and 1^3B_2 with 1.05 eV. These values are smaller than the corresponding vertical absorption transitions by 1.26 eV for the 1^1A_2, 1.19 eV for 1^3A_2, 0.04 eV for 1^1B_1, 1.07 eV for 1^3B_1, 1.13 eV for 1^1B_2, 1.48 eV for 1^3B_2, and 7.00 eV for 2^1A_1. This suggests that, with respect to the excited states, the ground state potential energy surface (PES) has a narrower low-energy domain.

The adiabatic excitation energies of the low-lying excited states of the C_2N_4 molecule in C_{2v} symmetry in relation to symmetry-related groups of this molecule in D_{2h} symmetry are expected to be lower. This is because, in C_{2v} symmetry, the geometry can be relaxed and the relaxation is expected to be larger for high-energy species, such as excited electronic states, than for the ground state. This expectation is met for some low-lying excited states: 1^1A_2 state is lower than $^1B_{1g}$ state by 0.797 eV; the 1^3A_2 state is lower than $^3B_{1g}$ state by 0.830 eV; the 1^3B_2 state is lower than $^3B_{2u}$ state by 0.815 eV; and the 2^1A_1 state is lower than 2^1A_g by 0.204 eV. But for the 1^1B_2 state relative to the $^1B_{2u}$ state, the 1^1B_1 state relative to $^1B_{3u}$ and the 1^3B_1 state relative to the $^3B_{3u}$ state, this

lowering was not observed. The abnormality is likely caused by the presence of multiple isomers on the lower symmetry surface.

Summary

The equilibrium geometries and absorption and emission energy calculations of low-lying excited states of [3,3']bidiazirinylidene (C_2N_4) in C_{2v} symmetry, relative to the ground state, have been performed at the GVVPT2 level of theory using the cc-pVDZ basis set. The GVVPT2 method has proven to be capable of dealing with all the states of interest without experiencing mathematical or computational difficulties, although C_2N_4 in this symmetry is highly multiconfigurational. GVVPT2 results are consistent with those of CCSD, QCISD and MP2. The seeming success of MP2, despite the substantial multiconfigurational nature of the zero-order wave function of this molecule in C_{2v} symmetry should be thought of as a result of fortuitous cancellation of errors. GVVPT2 results for the ground state of [3,3']bidiazirinylidene are similar to those in D_{2h} symmetry and also to those of difluorodiazirine (F_2CN_2), which has been investigated experimentally. Frequency calculations for this molecule at the MCSCF levels of theory for the ground state and all low-lying excited states show that they are at least local minima. The CN_2 ring is retained when excitation occurs but with resulting elongation of the N–N and/or C–N bond lengths compared to that of the ground state geometry. It was found that the 1^1B_2 and 1^3B_2 states can be described by the $3b_1 \Rightarrow 1a_2$ single excitation, which is spin allowed for the 1^1B_2 and spin forbidden for the 1^3B_2 transition in the ring moiety. The B_2 states are the only states that were found to have just one leading configuration, all the other states are highly multiconfigurational. For the 1^1B_1 and 1^3B_1 states the electronic transitions consist of one and three electron transitions $6b_2 \Rightarrow 1a_2$

and $6b_2\ 3b_1^2 \Rightarrow 1a_2\ 2a_2^2$. The energies of the excitations were 3.80 eV (spin and dipole allowed) and 2.36 eV (spin-forbidden but dipole allowed) transitions. These electronic excitations correspond to transitions from 1^1A_1 to the 1^1B_1 and 1^3B_1 excited states in the F_2CN_2. The results showed that C_2N_4 is more highly multiconfigurational in C_{2v} symmetry than it is in D_{2h} symmetry.

CHAPTER IV

MULTIREFERENCE PERTURBATION THEORY STUDIES OF THE LOWEST SINGLET AND TRIPLET ELECTRONIC STATES OF TETRAMETHYLENEETHANE DIRADICAL

Introduction

Diradicals are important intermediates in a number of thermal and photochemical reactions [147, 148]. They also provide insight into spin-spin-coupling phenomena. The properties of these diradicals are strongly affected by the relative energies of the low-lying singlet and triplet states. Specifically this determines the observed magnetic properties and the reactivity of the ground state of the diradical compound.

The relative ordering of the low–lying singlet and triplet states of diradicals is not easily observed experimentally or predicted theoretically, especially if their energy differences are small, which is the case with tetramethyleneethane, a disjoint diradical. Tetramethyleneethane is thought to be the central intermediate in the dimerization of allene to form 1,2-dimethylenecyclobutane [147] and in the thermal rearrangement of this compound [148]. The building block of many compounds with ferromagnetic and electrical conductivity properties is found to be tetramethyleneethane; [149-151] also it is observed to be incorporated into many ring systems [152]. The ground electronic state of tetramethyleneethane has been a subject of debate since Dowd (1970) [27] recorded the electron paramagnetic resonance (EPR) spectrum of this diradical [27, 153] and stated that its ground state is a triplet. Based on a

Curie-Weiss plot, the observation of a straight line suggested that the ground state is a triplet or that the triplet and singlet states are degenerate [20]. Results obtained for tetramethyleneethane from early *ab initio* studies contradict this experimental result. Theoretical studies showed that the singlet state lies below the triplet state by more than 1 kcal/mol [33, 154]. Moreover, Clifford et al. [16] in 1998 recorded the gas–phase negative ion photoelectron (NIPE) spectra of TME^- and obtained results that contradicted those obtained previously from the earlier matrix isolation EPR studies. They found that the energy of the singlet state of TME is 2.0 kcal/mol below that of the triplet state. Clifford et al. [16] suggested that Dowd's observation was because the matrix locked the TME into the triplet equilibrium structure, which is a position in which the singlet is above the triplet state in energy. Spin–restricted open–shell Kohn–Sham (ROKS) and spin–restricted ensemble–reference Kohn–Sham (REKS) methods where used by Filatov and Shaik [34] to study the triplet and singlet states of TME, respectively [34]. Their results showed that the singlet state of TME is lower in energy by about 3 kcal/mol than the triplet state. The minimum geometry for the singlet state was found to have D_{2d} symmetry and the triplet had D_2 symmetry (torsion angle 50.1°). Spin–orbit coupling matrix elements were also calculated by Filatov and Shaik between the $^3B_1$ and ^1A states and were found to be very small. Pittner et al. [20] did theoretical studies on tetramethyleneethane using the TDCCSD and BWCCSD methods. Their results likewise showed that the singlet state is lower in energy than the triplet state.

In this chapter, the second–order generalized Van Vleck perturbation theory (GVVPT2) [1] variant of multireference perturbation theory is used to describe this diradical. Because GVVPT2 analytical gradients have only been recently derived, and

production-level computer programs are not yet operational, other methods were used in conjunction with the GVVPT2 method for geometry optimization. Geometry optimizations were done at B3LYP and CASSCF(6,6) levels of theory, with the use of cc-pVDZ (correlation consistent polarized valence double zeta) basis sets. The Gaussian 03 suite of programs [141] was used to perform B3LYP and CASSCF(6,6) optimizations. The local suite referred to as UNDMOL was used in this study for GVVPT2 calculations.

A concise review of the computational methods is presented in the following section, emphasizing features pertinent to this study. Section 2 also describes other computational details, which include a description of the model space used for both the singlet and triplet state, constructed using the macroconfiguration approach [96]. In Section 3, the results of the relative stability of the low-lying triplet and singlet states with respect to torsion angle are presented and discussed.

Computational details

The symmetry of the compound was D_2 for both B3LYP and CASSCF(6,6) levels of theory, but the current implementation of UNDMOL only allowed the use of C_1 symmetry for the GVVPT2 calculations. An incomplete active space for model space was used in this study, including all spin and space symmetry allowed CSFs generated by single and double excitations from the three highest occupied orbitals to the three lowest unoccupied valence orbitals. Excitations were also allowed from the 13 core orbitals. Initial orbitals were obtained at a specific geometry from RHF calculations. Subsequent initial orbitals for other geometries were obtained from MCSCF orbitals at adjacent geometries. Although a CASSCF reference can be described by a single

macroconfiguration, it is computationally advantageous to divide it into multiple macroconfigurations.

The list of macroconfigurations determining the complete model space used includes: the closed-shell macroconfiguration describing the ground state,

$(n_0)^6 (v_0)^0$

and macroconfigurations describing the other excitations,

$(n_0)^5 (v_0)^1$

$(n_0)^4 (v_0)^2$

$(n_0)^3 (v_0)^3$

$(n_0)^2 (v_0)^4$

$(n_0)^1 (v_0)^5$

$(n_0)^0 (v_0)^6$

without any space symmetry restriction, the singlet state was spanned by 175 CSFs (created by 141 configurations) and the triplet state was spanned by 189 CSFs (created by 139 configurations). The dimensions of the corresponding external spaces of both the singlet and the triplet states at the cc-pVDZ level were 423,941,364 CSFs (created by 73,396,125 configurations) and 788,956,146 CSFs (created by 73,396,125 configurations) respectively. Our current GUGA-based GVVPT2 program [135] can perform the described calculation in reasonable time; e.g. a typical GVVPT2 calculation

takes 21 minutes for the singlet state (i.e., 423 million external and 175 model CSFs) on a 2.0 GHz dual-core AMD Opteron processor 2212.

Geometry optimization calculations for tetramethyleneethane were done at the B3LYP level of theory using both the ordinary and augmented cc-pVDZ and cc-pVTZ, i.e., the aug-cc-pVDZ and aug-cc-pVTZ, basis sets in order to determine the most cost effective basis set to use for this study. The results obtained when unaugmented basis sets (cc-pVDZ and cc-pVTZ) were used are not very different from those using the augmented counterparts (aug-cc-pVDZ and aug-cc-pVTZ). However, the use of augmented basis sets results in higher computational costs (cc-pVDZ takes 2 minutes 59.8 seconds, while the augumented cc-pVDZ takes 18 minutes 26.5 seconds and cc-pVTZ takes 34 minutes 2.3 seconds and the augmented cc-pVTZ takes 240 minutes 11.8 seconds). Specifically, the standard deviation (STDEV) is 0.0019 h (1.2 kcal/mol) (Table 10). Based on this observation, the less expensive basis set cc-pVDZ was used for all other calculations.

Table 10. Energies in Hartree for TME at the B3LYP level of theory for the triplet and singlet states for different basis sets.

Basis set	ES	ET	ΔE
cc-pVDZ	-233.3079619	-233.3317654	0.0238035
cc-pVTZ	-233.3877828	-233.4086412	0.0208584
aug-cc-pVDZ	-233.3284794	-233.3484102	0.0199308
aug-cc-pVTZ	-233.3918072	-233.4112957	0.0194885
STDEV			0.001941287 (1.2 kcal/mol)

To investigate the dependence of the energies of the singlet and triplet states on the torsion angle, optimized geometries of the compounds were obtained for different torsion angles at the B3LYP/cc-pVDZ (Table 11) and CASSCF(6,6)/cc-pVDZ (Table 12) levels of theory. At the B3LYP level of theory, for all torsion angles the triplet state was lower in energy than the singlet state. The minimum point for the singlet state was 0° (E_h = -233.307962 h) and that for the triplet state was 45° (E_h = -233.3368629 h). GVVPT2 studies on B3LYP optimized geometries showed that at some torsion angles (0°-27.5° and 78.5°-90°) the singlet state is the lowest-lying state while at other angles (27.5°-78.5°), the triplet state is the lowest-lying state (Figure 22). At the GVVPT2 level of theory for B3LYP optimized structures, the minimum for the singlet state was 90° (E_h = -232.5690632 h), and the minimum for the triplet state is at 45° (E_h = -232.5683043 h), Table 13 and Figure 23.

The CASSCF(6,6) geometry optimization on TME showed that the singlet state is the lowest state at all torsion angles. The minimum energy for the singlet state at the CASSCF level of theory occurs at 55° and that for the triplet state is at 50° (Figure 24). GVVPT2 studies on CASSCF(6,6) optimized structures gave a torsion angle of 90° as the minimum energy point for the singlet state and 45° as that for the triplet state (Figure 25). Because of the dependence of GVVPT2 single point energy results on the B3LYP and the CASSCF(6,6) optimized structure, and the fact that in B3LYP optimized structures at torsion angles of 55°, the energy difference between the singlet and the triplet state is about 3.95 kcal/mol with the triplet lower in energy than the singlet, GVVPT2 optimization calculations will be done at torsion angles 30°, 60°, and 90° in the future.

Table 11. Energies and energy difference for B3LYP/cc-pVDZ optimized structures of singlet (ES) and triplet states (ET).

Torsion angle/degree	ES	ET	(ES-ET).
0	-233.3079619	-233.3317655	0.023804
5	-233.3078257	-233.3319662	0.024140
10	-233.3073933	-233.3325094	0.025116
15	-233.3066272	-233.3332777	0.026650
20	-233.3054935	-233.3341433	0.028650
25	-233.3039567	-233.3349902	0.031034
30	-233.3019946	-233.3357308	0.033736
35	-233.2996113	-233.3363058	0.036694
40	-233.2968396	-233.3366849	0.039845
45	-233.2937343	-233.3368626	0.043128
50	-233.2903623	-233.3368516	0.046489
55	-233.2868064	-233.3366843	0.049878
60	-233.2831826	-233.3364042	0.053222
65	-233.2796335	-233.3360646	0.056431
70	-233.276341	-233.3357166	0.059376
75	-233.2735013	-233.3353951	0.061894
80	-233.2713027	-233.3351363	0.063834
85	-233.2699044	-233.3349721	0.065068
90	-233.2692597	-233.3349166	0.065657

Table 12. Energies and energy difference for CASSCF(6,6)/cc-pVDZ optimized structures for the singlet (ES) and the triplet states (ET).

Torsion angles/degree	ES	ET	(ES - ET)
0	-231.8316174	-231.8256171	-0.006000
5	-231.8316933	-231.8258087	-0.005885
10	-231.8318919	-231.826334	-0.005558
15	-231.8321511	-231.8270808	-0.005070
20	-231.8324144	-231.8279284	-0.004486
25	-231.8326457	-231.8287733	-0.003872
30	-231.83283	-231.8295366	-0.003293
35	-231.8329663	-231.8301644	-0.002802
40	-231.8330607	-231.8306267	-0.002434
45	-231.8331208	-231.8309148	-0.002206
50	-231.833152	-231.8310392	-0.002113
55	-231.8331585	-231.8310249	-0.002134
60	-231.8331438	-231.830907	-0.002237
65	-231.8331127	-231.8307248	-0.002388
70	-231.8330712	-231.8305169	-0.002554
75	-231.8330269	-231.8303173	-0.002710
80	-231.8329876	-231.8301542	-0.002833
85	-231.8329607	-231.8300479	-0.002913
90	-231.8329512	-231.8300111	-0.002940

Table 13. Energies and energy difference for GVVPT2/cc-pVDZ calculations on B3LYP optimized structures for the singlet (ES) and the triplet states (ET).

Torsion angle/degree	ES	ET	(ES - ET)
0	-232.5680167	-232.5633628	-0.004654
5	-232.5680655	-232.5634323	-0.004633
10	-232.5681042	-232.5640173	-0.004087
15	-232.568045	-232.5648189	-0.003226
20	-232.5678006	-232.565696	-0.002105
25	-232.5673133	-232.5665375	-0.000776
30	-232.5665787	-232.5672593	0.000681
35	-232.5656286	-232.567809	0.002180
40	-232.5645474	-232.5681586	0.003611
45	-232.5634754	-232.5683043	0.004829
50	-232.5624428	-232.568262	0.005819
55	-232.5617685	-232.5680691	0.006301
60	-232.5616113	-232.5677704	0.006159
65	-232.5622191	-232.5674157	0.005197
70	-232.5634892	-232.5670529	0.003564
75	-232.5653349	-232.5667241	0.001389
80	-232.5672307	-232.5664635	-0.000767
85	-232.5686439	-232.5662995	-0.002344
90	-232.5690632	-232.5662429	-0.002820

Table 14. Energies and energy difference for GVVPT2/cc-pVDZ calculations on CASSCF(6,6) optimized structures for the singlet (ES) and the triplet states (ET).

Torsion angle/degree	ES	ET	(ES – ET)
0	-232.5687261	-232.5628669	-0.005859
5	-232.5687741	-232.562946	-0.005828
10	-232.5689252	-232.5635155	-0.005410
15	-232.5690894	-232.5648189	-0.004270
20	-232.5692172	-232.5651609	-0.004056
25	-232.5692939	-232.5659891	-0.003305
30	-232.5693314	-232.5667026	-0.002629
35	-232.5693565	-232.567247	-0.002109
40	-232.5693968	-232.5675948	-0.001802
45	-232.5694688	-232.5677421	-0.001727
50	-232.5695736	-232.5677059	-0.001868
55	-232.5696998	-232.5675203	-0.002180
60	-232.56983	-232.5672296	-0.002600
65	-232.5699479	-232.5668827	-0.003065
70	-232.5700433	-232.5665269	-0.003516
75	-232.5701126	-232.5662043	-0.003908
80	-232.5701572	-232.5659487	-0.004208
85	-232.5701812	-232.5657851	-0.004396
90	-232.5701888	-232.5657281	-0.004461

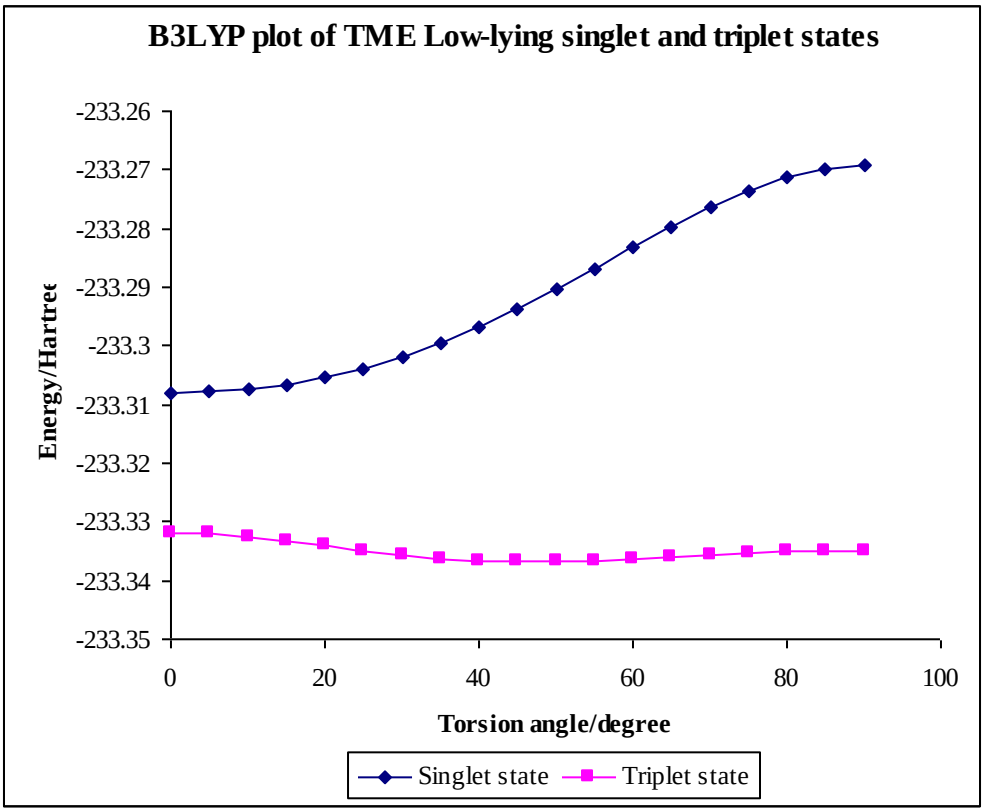

Figure 21. Plot of the partial optimization of tetramethyleneethane vs. torsion angle at B3LYP/cc-pVDZ level of theory.

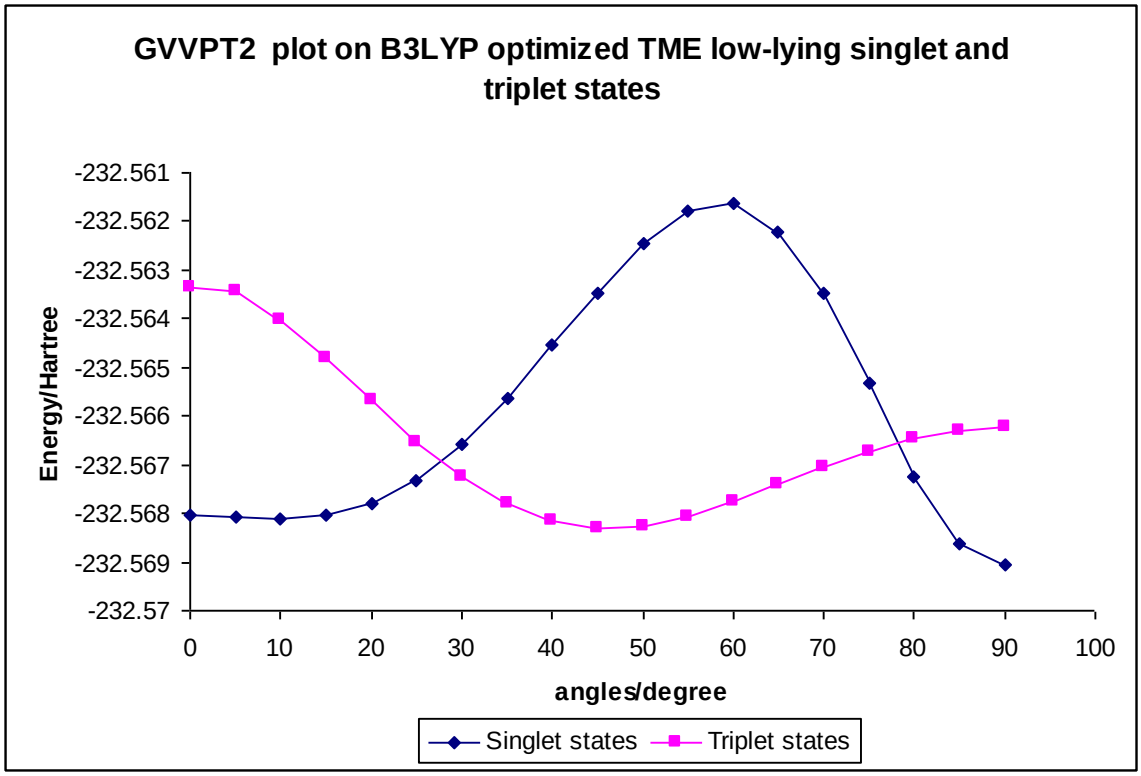

Figure 22. Plot of the partial optimization of tetramethyleneethane vs. torsion angle at GVVPT2/cc-pVDZ level of theory on B3LYP optimized structures.

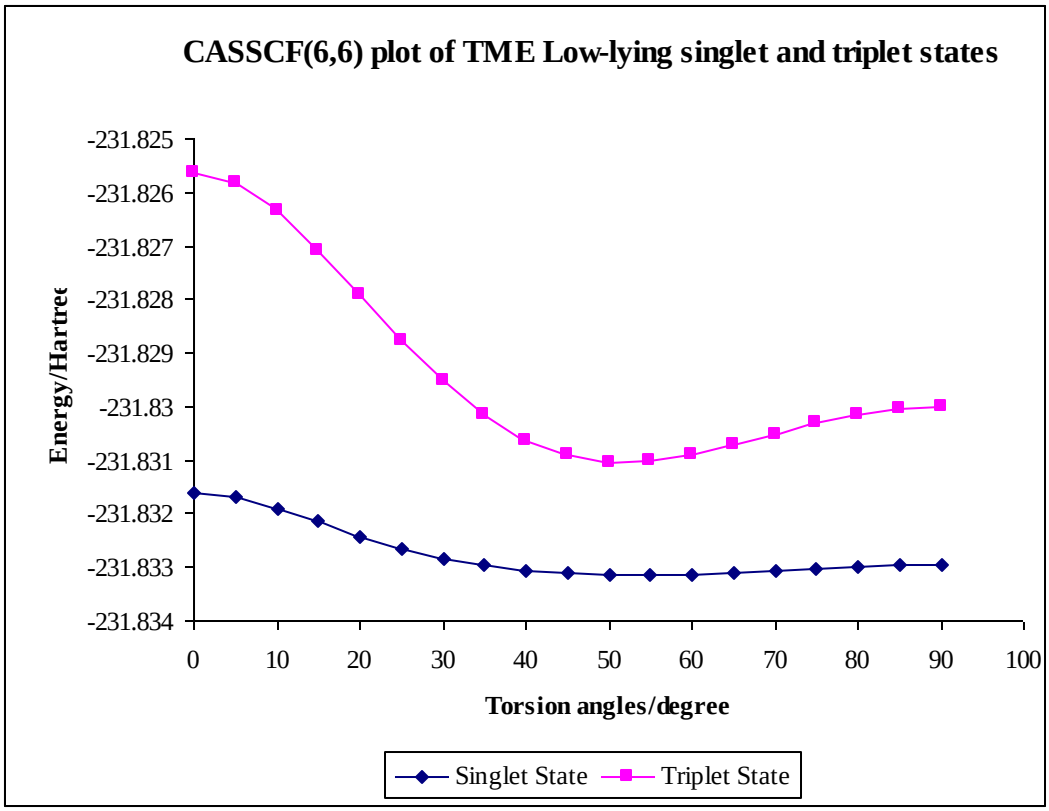

Figure 23. Plot of the partial optimization of tetramethyleneethane vs. torsion angle at CASSCF(6,6)/cc-pVDZ level of theory.

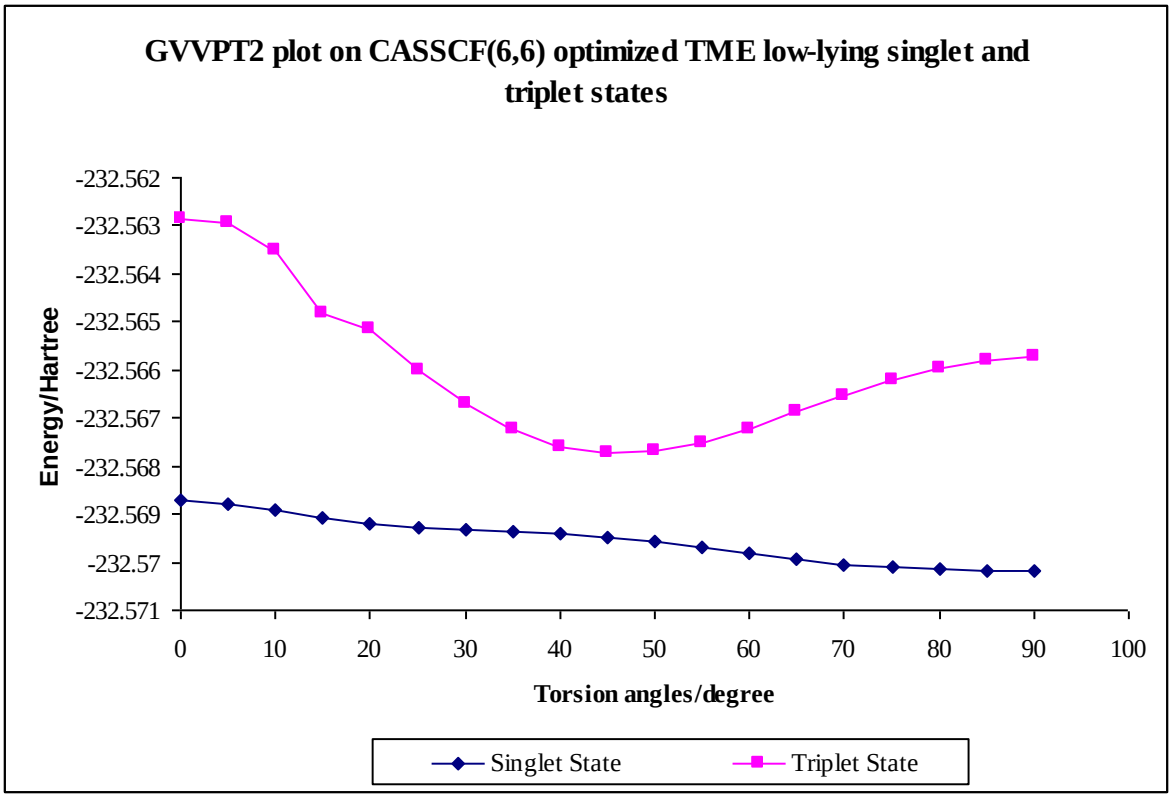

Figure 24. Plot of the partial optimization of tetramethyleneethane vs. torsion angle at GVVPT2/cc-pVDZ level of theory on CASSCF(6,6) optimized structures.

Summary

Single point energy calculations at the GVVPT2 level of theory with the use of the cc-pVDZ basis set on B3LYP optimized structures show that the ground state of TME is dependent on geometry. For torsion angles 0° – 25° and 80° – 90°, it was observed that the singlet state is the lowest energy state but at all other torsion angles the ground state electronic structure was the triplet state. The singlet TME had a minimum at 90° (-232.234742 Hartree) and the minimum geometry for the triplet state was found to be 45° (-232.238500 Hartree) (Figure 23). GVVPT2 single point

energy calculation on CASSCF(6,6) optimized geometries showed that the singlet state energy is the ground state is always lower than the triplet (Figure 25).

CHAPTER V

THEORETICAL STUDY OF ARSENIC OXIDES

Introduction

The discharge, deposition, and control of toxic trace elements emitted during coal combustion are of environmental interest. Trace elements are by definition present in small or very small concentrations. Moreover, the concentrations of trace elements, and their speciation, vary over time. Effective remediation of the elements is facilitated by as full as possible understanding of their thermodynamic stabilities and kinetic reactivities. Arsenic is one of the trace elements found in fly ash and hot flue gases [44, 155-157]. The forms in which arsenic is mostly likely to occur in flue gas during coal combustion is elemental (As) or as oxides [155, 158].

The oxidation states in which arsenic is found are: -3, +3, and +5. Arsenic in the +3 oxidation state and in the inorganic form is its most toxic form [157]. The organs which are most affected by arsenic are: the gastrointestinal tract, circulatory system, liver, kidney and the skin [41]. Excess arsenic in drinking water from underground wells causes serious outbreaks of ill health, as reported in Bangladesh [55]. Besides all the other effects of arsenic in the environment and health, arsenic, especially in the form of As_2O_3, has been thought to deactivate the catalyst used in selective catalytic reduction (SCR) units. Deactivation of SCR will lead to poor catalytic performance, and increase the cost of NO_x control [157, 159].

The structures and oxidation states of the monoxides of arsenic have been studied experimentally, and to some extent, theoretically. Anderson et al. [160] analyzed the emission spectra of the ground state ($^2\Pi$) of AsO, and its bond length was observed to be 1.623 Å [160]. Kushawaha et al. [161] also investigated the electronic spectrum of AsO and observed bands in the regions 6550 – 5800 Å and 5150 – 4140 Å. Essig et al. [162] measured the infrared spectrum of AsO and accurately determined a set of molecular parameters e.g., frequency which was 966.6 cm^{-1}. Knight et al. [163] did electron spin resonance (ESR) studies on AsO_2 molecule in neon matrix and found that As isotropic hyperfine interactions (A_{iso}) parameter was 937 MHz. Theoretical studies of some of the monomeric arsenic oxides have also been done [49, 163-167], but an understanding of the mechanisms of their formation have not been thoroughly investigated. Direct experimental measurements are difficult because often their occurrences are at high temperatures and in complex environments. The dimeric arsenic oxides have not been studied, to the best of our knowledge, either experimentally or theoretical.

The theoretical studies of these oxides require high-level methods that will provide a balanced treatment of dynamic and nondynamic electron correlation. The present work makes use of the GVVPT2 method, with cc-pVDZ [139] and cc-pVTZ [139] basis sets, to study the structures of the monomeric arsenic oxides. Optimized geometries for monomeric and isomers of dimeric oxides were also obtained using the B3LYP/6-311G* method. The optimized parameters for the monomeric arsenic oxides from both the GVVPT2/cc-pVTZ and B3LYP/6-311G* methods were compared, in order to validate the use of DFT for geometry optimization of plausible dimers. At the optimized geometries obtained at the B3LYP level of theory, single point energy

calculations were done at the CR–CCSD(T) [50-52] level of theory to compute accurate energies of the isomers and some barriers. Harmonic frequencies of the equilibrium and transition-state structures were computed to verify the type of stationary point (i.e., minimum or transition state) and to assist in the vibrational spectroscopy. A local electronic structure software suite (i.e., UNDMOL) was used to perform GVVPT2 calculations. B3LYP optimization calculations were done using the Gaussian 03 program [141]. GAMESS US was used for the CR-CCSD(T) [52] calculations.

There are four sections in this chapter. Section 2 contains a detailed description of the reference space used for this study. Other computational details are also included in that section. In Section 3, the results are presented and are discussed in relation to the stability of the arsenic oxides. Finally, Section 4 summarizes the work.

Computational details

The geometries of the monomeric arsenic oxides were obtained using GVVPT2 with an energy-based optimization. In this study, a complete active space for MCSCF (i.e., CASSCF) was used to obtain the orbitals for the GVVPT2 study. The model space is denoted as follows, *(m|n)*, where *m* is the number of orbitals and *n* is the number electrons. In a complete active space, all possible configurations are allowed.

The largest pertinent molecular point group symmetry that is currently available in UNDMOL is C_{2v}, which was used for studying the monomeric arsenic oxides: AsO, AsO_2, and AsO_3. The active space was chosen such that it includes the most important high occupancy molecular orbitals, G_1 (i.e., G_1 = HOMO, HOMO-1,…..) and the low occupation molecular orbitals, G_2 (i.e., G_2 = LUMO, LUMO+1, ….). For AsO, the set of

8 valence molecular orbitals (i.e., *2s* and *2p* orbitals of O, and the *4s* and *4p* orbitals of As) having seven electrons, were divided into two subgroups: $G_1 = (4b_2, 5b_1, 4b_1, 11a_1)$, and $G_2 = (5b_2, 6b_1, 13a_1, 12a_1)$. The AsO_2 molecule had 10 valence orbitals in its active space (i.e., the *2p* of each O, and the *4s* and *4p* of arsenic) divided into two subgroups as follows: $G_1 = (7b_2, 6b_2, 4b_1, 2a_2, 12a_1, 11a_1, 10a_1)$ and $G_2 = (8b_2, 5b_1, 13a_1)$, with of 13 active electrons. And AsO_3, with $G_1 = (8b_2, 7b_2, 6b_2, 5b_1, 4b_1, 2a_2, 14a_1, 13a_1, 12a_1)$ and $G_2 = (9b_2, 6b_1, 16a_1, 15a_1)$, had 17 active electrons. The above calculations can be performed by the current GUGA-based GVVPT2 program in UNDMOL [135] in a reasonable amount of time; as an example, 10 minutes is required to run a typical GVVPT2 calculation with a total of 53.4 million CSFs and 3498 model space CSFs on a 2.0 GHZ dual-core Opteron processor 2212.

Results and discussion

Monomeric Arsenic oxides

Arsenic monoxide (AsO)

The predictions of spectroscopic constants and experimental data for the ground state of AsO are listed in Table 15. As can be seen from Table 15, the cc-pVTZ basis set gives significantly better agreement with experimental values of spectroscopic constants, especially the equilibrium bond length, r_e, harmonic frequency, ω_e, and rotational constant, B_e, than the cc-pVDZ basis set at both theory levels (i.e., MCSCF and GVVPT2). GVVPT2 improves the quality of predicted values of r_e and B_e relative to experimental data as compared to MCSCF. The GVVPT2 predicted value of the dissociation energy D_e is 109.6 kcal/mol with the *(6|7)* active space, in contrast to the 84.7 kcal/mol predicted by MCSCF. Increasing the active space to *(8|7)* by adding two

a_1 orbitals did not lead to improvement of the result, but led to slightly poorer results for r_e and B_e with the use of the larger basis set. The AsO optimized structure was also obtained at the B3LYP/6-311G* level of theory and the parameters compared to those obtained at the GVVPT2(*6*|*7*)/cc-pVTZ level of theory, and found to be in close agreement. The r_e bond length of AsO at the GVVPT2 level is smaller than that obtained at the B3LYP level by 0.002 Å (Table 16). The formation of AsO from the reaction of As and O is predicted to be feasible at both the B3LYP and CR-CCSD(T) level of theories. The calculated energies of reactions are -47.9 kcal/mol as obtained at the B3LYP level, and -34.2 kcal/mol and -47.5 kcal/mol at the CR-CCSD(T) level of theory with the use of cc-pVDZ and cc-pVTZ basis sets respectively (Table 15).

Table 15. Some thermodynamic constants for the ground state of AsO.

Method	r_e(Å)	ω_e(cm^{-1})	B_e(cm^{-1})	D_e (kcal/mol)
MCSCF(6|7)/cc-pVDZ	1.661	906.3	0.4635	74.9
MCSCF(6|7)/cc-pVTZ	1.637	956.5	0.4770	84.7
MCSCF(8|7)/cc-pVTZ	1.640	952.1	0.4754	88.3
GVVPT2(6|7)/cc-pVDZ	1.657	917.5	0.4655	91.1
GVVPT2(6|7)/cc-pVTZ	1.630	982.9	0.4815	109.6
GVVPT2(8|7)/cc-pVTZ	1.641	954.6	0.4747	107.5
Exp.[a,b]	1.6236	967.08 (965.90)	0.48482 (0.48552)	

[a] Ref. [168].

[b] The values for the $^2\Pi_{1/2}$ and $^2\Pi_{3/2}$ states with the latter in parenthesis.

Table 16. Comparison of B3LYP/6-311G* structures to that of GVVPT2/cc-pVTZ.

	Parameters	B3LYP	GVVPT2
AsO	r_{e_1}(Å)	1.632	1.630
AsO_2	r_{e_1}(Å)	1.647	1.634
	θ (Degrees)	126.2	129.1
AsO_3	r_{e_1}(Å)	1.613	1.606
	r_{e_2}(Å)	1.669	1.662
	θ (Degrees)	102.3	100.2

Arsenic dioxide (AsO_2)

AsO_2 was optimized at both the GVVPT2 level of theory using the cc-pVTZ basis set and the B3LYP DFT level of theory using the 6-311G* basis set. The lowest doublet states of all four irreducible representations of C_{2v} symmetry, i.e., $^2A_1$, $^2A_2$, $^2B_1$, and $^2B_2$ states, were optimized at the GVVPT2 level of theory; only the geometry of the $^2A_1$ state was obtained at the B3LYP level. The r_e bond length for the two methods agree well. The r_e obtained at the GVVPT2(10|13)/cc-pVTZ is smaller than that of B3LYP/6-311G* by 0.013 Å and the angle θ by 2.9˚, as shown in Table 16. These results can be compared with previous theoretical study by Knight et al. [163] for the $^2A_1$ state using MP2/DZP. The bond length r_e obtained by Knight et al. [163] is shorter by 0.004 Å and 0.017 Å to those calculated at the GVVPT2 and B3LYP level of theories respectively (Table 17). Harmonic frequencies of the ground states of AsO_2 were calculated at the MCSCF, GVVPT2 and B3LYP methods, and are shown in Table 18. The MCSCF, GVVPT2 and

B3LYP results for the symmetric stretch and bend differ by a small amount in the range of 5 – 28 cm^{-1}. In contrast, the asymmetric stretching vibration (ω_3) of AsO_2 has a difference of 236.4 cm^{-1}. This is symptomatic of an imbalance in the number of orbitals of each symmetric type, as was noted by Theis et al. [169]. The formation of AsO_2 from the reaction of AsO and O is predicted to be feasible by the MCSCF method, with a reaction enthalpy -54.1 kcal/mol, by the GVVPT2 method with a reaction enthalpy of -50.7 kcal/mol (Table 20), by the B3LYP method with a reaction energy of -22.0 kcal/mol, and also by the CR-CCSD(T) method with reaction energies of -17.9 kcal/mol and -26.8 kcal/mol using the cc-pVDZ and cc-pVTZ basis sets respectively (Table 29).

Table 17. Optimized geometries and experimental values for AsO_2 and AsO_3 at the GVVPT2/cc-pVTZ level of theory.

Oxides	Symmetry	Active space	r_1(Å)	r_2(Å)	θ (degree)
AsO_2	$^2A_1$	(7|9)	1.623		121.0
	$^2A_1$	(10|13)	1.634		129.1
	$^2A_1$[a]		1.630		135
	$^2A_2$	(7|9)	1.693		100.4
	$^2A_2$	(10|13)	1.703		104.3
	$^2B_1$	(7|9)	1.741		102.7
	$^2B_1$	(10|13)	1.744		107.7
	$^2B_2$	(7|9)	1.662		91.1
	$^2B_2$	(10|13)	1.687		93.7
	$^2B_2$[b]		1.682		92.3
AsO_3	$^2A_1$	(7|7)	1.643	1.587	115.4
	$^2A_1$	(12|17)	1.675	1.618	119.9
	$^2A_2$	(7|7)	1.674	1.575	109.6
	$^2A_2$	(12|17)	-	-	-
	$^2B_1$	(7|7)	1.596	1.738	137.5
	$^2B_1$	(12|17)	1.616	1.726	130.1
	$^2B_2$	(7|7)	1.630	1.569	103.9
	$^2B_2$	(12|17)	1.662	1.606	100.2

[a] Optimized by MP2 with the DZP basis set, from Ref. [163].

[b] Optimized by B3LYP with the aug-cc-pVTZ basis set, from Ref. [166].

Table 18. Harmonic frequencies (cm^{-1}) of AsO_2.

Oxides	Symmetry	Method	$\omega_1(a_1)$	$\omega_2(a_1)$	$\omega_3(b_2)$
AsO_2	$^2A_1$	MCSCF	873.3	255.9	870.2
	$^2A_1$	GVVPT2	890.7	275.5	1043.7
	$^2A_1$	B3LYP	858.1	271.9	807.3

Arsenic trioxide (AsO_3)

The optimized parameters obtained from this work on the geometry at both the GVVPT2/cc-pVTZ level with the (10|13) active space and B3LYP/6-311G* are compared in Table 16, and they are in close agreement. Experimental results for AsO_3 are not available. The r_{e1} and r_{e2} bond lengths for the B3LYP calculations are longer than those for the GVVPT2 calculation by 0.007 Å and the $\angle$OAsO angle by 2.1°. The symmetry of the ground state was predicted to be the $^2B_2$ electronic state. No other theoretical results are known for this molecule. The formation of AsO_3 from the oxidation of AsO and AsO_2 was predicted to be feasible at both the MCSCF and GVVPT2 levels of theory, with the largest exothermically being the oxidation of AsO. The reaction energies (the energy sum of the binding energies of the products minus that of reactants {Table 19}) are -60.5 kcal/mol and -6.4 kcal/mol at the MCSCF level of theory for the oxidation of AsO and AsO_2 respectively, and at the GVVPT2 level the energies are -65.2 kcal/mol and -14.5 kcal/mol respectively (Table 20). Using B3LYP, almost the same prediction was reached. The energies of reactions were -17.4 kcal/mol and 4.7 kcal/mol for the oxidation of AsO and AsO_2 respectively. At the CR-CCSD(T)

level of theory convergence was not attained for a single point energy calculation of the AsO_3 molecule (Table 29).

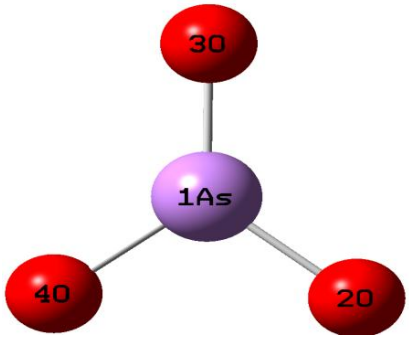

Figure 25. Arsenic trioxide (AsO_3).

Reaction enthalpies of the oxidation of monomeric arsenic oxides

The binding energies for the monomeric arsenic oxides and O_2 are given in Table 19. They were used to calculate reaction enthalpies (the energy sum of the products minus that of reactants) and the results are recorded in Table 20. The GVVPT2 method shows that the order of stability for the arsenic monoxides is as follows

$$AsO < AsO_2 < AsO_3$$

That is, the stability increases as the number of oxygen atoms bonded to the As atom increases. The same trend is observed for the MCSCF results, but not for B3LYP level of theory. At the B3LYP level, AsO is the most stable, followed by AsO_2 and least stable AsO_3 molecule (Table 29). AsO_3 molecule did not converge at the CR-CCSD(T) level of theory.

Table 19. Total binding energies (kcal/mol) of the arsenic monoxides.

Molecules	Symmetry	MCSCF	GVVPT2
O_2	$X\,^3\Sigma_g^-$	-88.2	-122.0
AsO	$X\,^2\Pi$	-84.7	-109.6
AsO_2	$^2A_1$	-182.9	-221.3
AsO_3	$^2B_2$	-233.4	-296.8

Table 20. Reaction enthalpies (kcal/mol) for the oxidation of As oxides.

Reaction	MCSCF	GVVPT2
$AsO(X\,^2\Pi) + ½\ O_2 \rightarrow AsO_2\ (^2A_1)$	-54.1	-50.7
$AsO(X\,^2\Pi) + O_2 \rightarrow AsO_3(^2B_2)$	-60.5	-65.2
$AsO_2(^2A_1) + ½\ O_2 \rightarrow AsO_3(^2B_2)$	-6.4	-14.5

Dimeric Arsenic Oxides

Computationally, it was expensive to perform calculations on the dimeric arsenic oxides using the multireference GVVPT2 method, since only an energy-only optimizer is available for production runs. Moreover, since the optimized parameters obtained using the B3LYP method agree well with those obtained using the GVVPT2 method for monomeric arsenic oxides, geometry optimization for the dimeric oxides was done at the B3LYP level of theory (using the 6-311G* basis set). This also corroborates the conclusions in the recent work by Mbote et al. [170] for which compounds optimized at

the B3LYP level of theory followed by GVVPT2 single point calculations gave good descriptions of molecules. On the optimized geometries, CR-CCSD(T) single point energy calculations were done using cc-pVDZ and cc-pVTZ basis sets to obtain accurate energies of the systems.

Diarsenic trioxides (As_2O_3)

On investigating the As_2O_3 molecule, at the B3LYP level of theory using the 6-311G* basis set, four minima and three transition states were observed: isomers 1, 2, 3, and 4, and transition states: TS12, TS23, and TS34 as shown in Figure 27. The harmonic frequencies, which confirm the stationary points as minima and saddle points, are shown in Tables 22. Isomer 1 is a cage structure, having equal bond lengths i.e., $R_{O1\text{-}As2}$, $R_{O1\text{-}As3}$, $R_{O4\text{-}As2}$, $R_{O4\text{-}As3}$, $R_{O5\text{-}As2}$, and $R_{O5\text{-}As3}$, are 1.866 Å long. The $R_{O1\text{-}As2}$, $R_{O4\text{-}As2}$, and $R_{O5\text{-}As3}$, of isomer 2, 3, and 4, and the transition states TS12, TS23 and TS34 are shorter than that of isomer 1 by 0.021 Å–0.254 Å. The $R_{O1\text{-}As3}$ bond length of isomer 2 and transition state TS12 are longer than that of isomer 1 by 0.266 Å–0.280 Å, but those of isomer 3, 4, and transition states TS23 and TS34 are shorter by 0.047 Å–0.049 Å. The $R_{O4\text{-}As3}$ bond length for isomer 2 and transition state TS12 are longer than that of isomer 1 by 0.266 Å–0.280 Å. But isomers 3, 4, and transition states TS23 and TS34 do not have a $R_{O4\text{-}As3}$ bond; there is no $R_{O5\text{-}As2}$ bond for any isomer or transition state besides isomer 1. The bond angles: $\angle O_5As_3O_1$, $\angle As_3O_1As_1$, and $\angle O_1As_2O_4$ of isomer 2, 3, 4, and transition states TS12, TS23, and TS34 are larger than that of isomer 1 by 10.4°–53.4°, as the $R_{O4\text{-}As3}$ and $R_{O5\text{-}As2}$ bonds break and the structure changes from a cage form to an open chain form (Table 23).

At the B3LYP level of theory, isomer 2 with C_s symmetry was the most stable with a relative energy to isomer 1 of -0.47 kcal/mol. The next stable isomer was isomer 1, then 3 with a relative energy of 0.19 kcal/mol, and isomer 4 was observed as the least stable. The barrier height between isomer 1 and 2, i.e., TS12, is about 12.4 kcal/mol, that between isomer 2 and 3, i.e., TS23, is 1.2 kcal/mol and that between isomer 3 and 4, TS34, is 0.89 kcal/mol. At the CR-CCSD(T) level of theory, with the use of both the cc-pVDZ and cc-pVTZ basis sets, isomer 1, which is the cage form with C_{2V} symmetry, became the most stable isomer. The next was isomer 4 with a relative energy of 2.6 kcal/mol and 2.0 kcal/mol for the cc-pVDZ and cc-pVTZ basis sets respectively. Then isomer 3 with a relative energy of 2.8 kcal/mol and 2.2 kcal/mol for the cc-pVDZ and cc-pVTZ basis. The least stable isomer was found to be isomer 2 (Table 21 and Figure 28). Transition state TS12 at the CR-CCSD(T) level of theory had an energy barrier of about 21.46 kcal/mol with the use of the cc-pVDZ basis and 18.17 kcal/mol with the cc-pVTZ basis, transition state TS23 had relative energies of 4.4 kcal/mol and 3.4 kcal/mol for the two basis set. The transition state between isomer 3 and 4 with the use of both basis sets was less than 4 kcal/mol (Table 21).

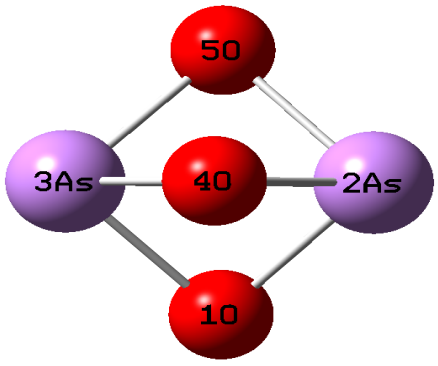

Figure 26. Diarsenic trioxide (As_2O_3).

Table 21. Relative energies of diarsenic trioxide (As_2O_3) isomers.

Molecule	Sym	6-311G*	cc-pVDZ	cc-pVTZ
		B3LYP	CR-CCSD(T)	
Isomer 1	C_{2v}	0.00	0.0	0.0
Isomer 2	C_s	-0.47	6.0	4.5
Isomer 3	C_2	0.19	2.8	2.2
Isomer 4	C_s	0.92	2.6	2.0
TS 12	C_1	12.4	21.5	18.2
TS 23	C_1	1.2	4.4	3.4
TS 34	C_1	0.89	3.4	2.5

Table 22. Vibrational frequencies of diarsenic trioxide (As_2O_3) isomers and transition states (in cm^{-1}) calculated using B3LYP/6-311G*.

Frequencies/As_2O_3	1 (C_{2v})	2 (C_s)	3 (C_1)	4 (C_s)	TS12	TS23	TS34
1	325.8	123.0	55.4	10.9	-225.9	-72.7	-18.5
2	329.5	139.3	67.5	79.4	164.3	69.8	56.8
3	405.6	203.3	70.4	114.9	338.5	128.3	105.5
4	408.0	239.2	279.5	223.2	351.0	284.6	274.1
5	424.4	328.0	329.6	299.4	362.8	325.1	305.1
6	587.1	464.8	429.7	491.4	466.0	504.3	465.8
7	624.9	781.6	690.9	691.3	713.9	668.5	693.5
8	626.5	845.8	987.7	975.5	770.2	935.5	976.4
9	720.1	1011.1	996.0	996.2	864.5	1003.9	998.0

Table 23. Optimized geometries of diarsenic trioxide (As_2O_3) isomers and transition states at the B3LYP/6-311G* level of theory.

Compound	1	2	3	4	TS12	TS23	TS34
$R_{O1\text{-}As2}$	1.866	1.700	1.819	1.845	1.738	1.770	1.841
$R_{O4\text{-}As2}$	1.866	1.700	1.619	1.617	1.738	1.642	1.616
$R_{O4\text{-}As3}$	1.866	2.146	-	-	2.032	-	-
$R_{O1\text{-}As3}$	1.866	2.146	1.819	1.802	2.032	1.894	1.797
$R_{O5\text{-}As2}$	1.866	-	-	-	-	-	-
$R_{O5\text{-}As3}$	1.866	1.612	1.619	1.671	1.649	1.613	1.625
$\angle O_5As_3O_1$	82.1	103.2	106.8	106.7	89.4	104.3	105.9
$\angle As_3O_1\ As_2$	81.4	96.3	134.8	129.7	86.1	113.8	130.8
$\angle O_1As_2O_4$	82.1	95.5	106.8	103.4	91.8	101.1	104.7

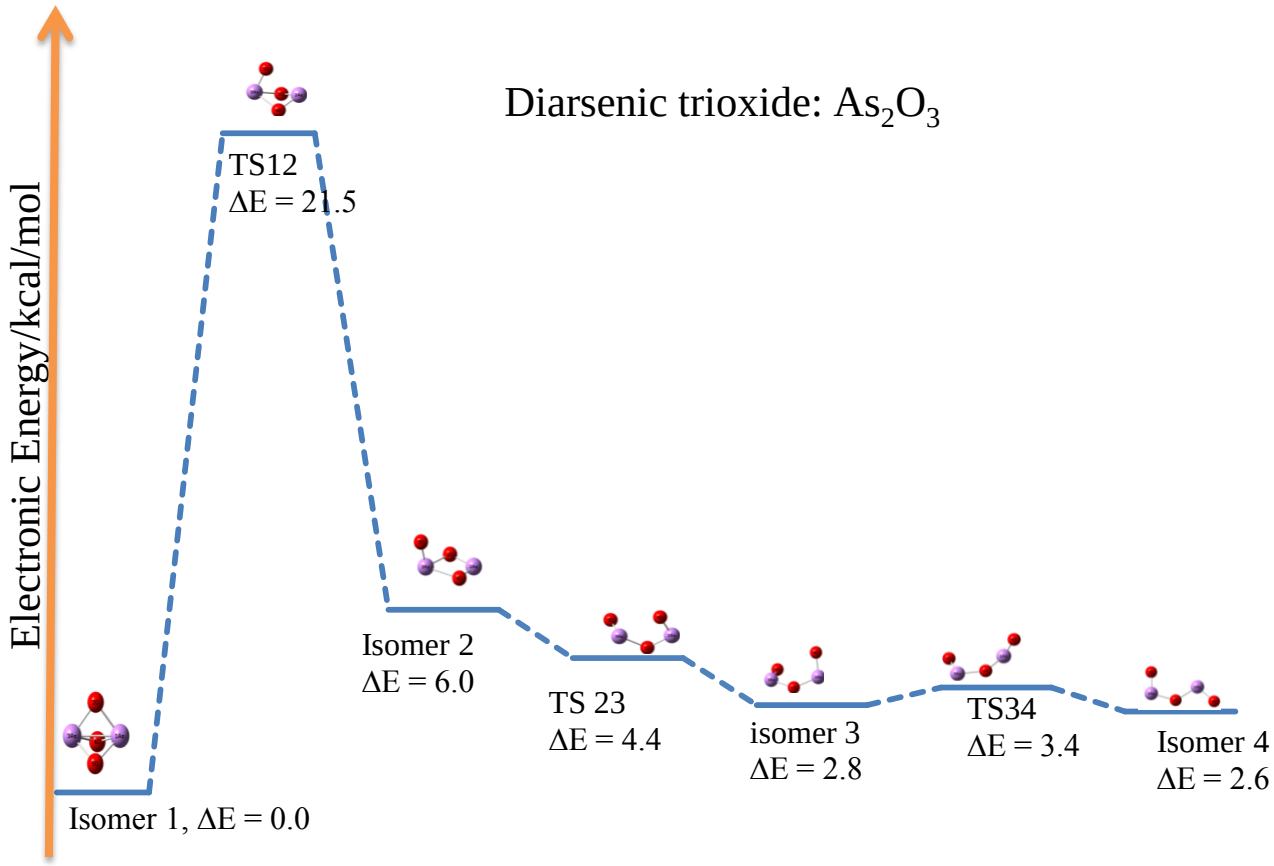

Figure 27. Relative energies in kcal/mol of diarsenic trioxide (As_2O_3) isomers and transition states using the CR-CCSD(T) method.

Diarsenic pentaoxide (As_2O_5)

B3LYP optimization of diarsenic pentaoxide (As_2O_5) (Figure 29) resulted in seven minima, isomer 1 with D_{3h} symmetry, isomer 3 with C_{2v} symmetry, isomers 2, 4, and 6, with C_s symmetry and isomers 5 and 7 with C_1 symmetry. The following transitions states were observed, TS13, between isomer 1 and 3 has C_s symmetry, TS24 and TS35 with C_s symmetry and TS67 with C_1 symmetry. The harmonic frequencies which confirm the stationary points minima and saddle point are shown in Table 27. The $R_{O2\text{-}As1}$ and $R_{O7\text{-}As6}$ bond of isomer 1 are equal and have a bond length of 1.603 Å long.

They are shorter than those of the other isomers and transition states by 0.002 Å–0.265 Å. The $R_{O3\text{-}As1}$ bond length of isomer 1 is longer than those in any other isomers and transition states by 0.003 Å–0.247 Å except for isomer 2. The $R_{O3\text{-}As1}$ bond length of isomer 2 is longer than that of isomer 1 by 0.047 Å. Isomer 5 does not have a $R_{O3\text{-}As1}$ bond. Isomers 2, 3, 4, 5, 6, and 7 and the transition states have their $R_{O4\text{-}As1}$, $R_{O5\text{-}As1}$, and $R_{O3\text{-}As6}$ bond lengths shorter than that of isomer 1 by 0.003 Å–0.246 Å, except the $R_{O4\text{-}As1}$, and $R_{O5\text{-}As1}$ bonds of isomer 4 which are longer by 0.119 Å. Isomer 4, TS13, TS35, and TS67 do not have a $R_{O3\text{-}As6}$ bond. Also isomers 5, 6, 7 and TS12 do not have a $R_{O4\text{-}As1}$ bond. The $R_{O5\text{-}As1}$ bond is absent in transition states TS12, TS35, and TS67. In looking at the $R_{O4\text{-}As6}$ and $R_{O5\text{-}As6}$ bond lengths of isomers 3, 5, and 6, and transition states TS12 and TS35, they are shorter than that of isomer 1 by 0.036 Å–0.224 Å. But the $R_{O4\text{-}As6}$ and $R_{O5\text{-}As6}$ bond lengths of isomers 2 and 4 and transition state TS67 are longer than that of isomer 1 by 0.049 Å–0.360 Å when the bond is present. The only isomers having the $R_{O7\text{-}As1}$ bond are isomers 2 and 4, and the bond lengths are shorter than that of isomer 1 by 0.079 Å–0.087 Å. The $\angle O_5As_1O_3$ bond angles of isomers 3, 5, 6, and 7 are all larger than that for isomer 1 by 7.8°–30.5° except that of isomer 2 which is less by 1.0°. The transition states did not possess a $\angle O_5As_1O_3$ bond angle (Tables 26 and 28).

The reference point for the As_2O_5 isomers and transition states was isomer 6. It had the lowest energy at the B3LYP level of theory, followed by isomer 3 with a relative energy of 4.2 kcal/mol, then isomer 5 with a relative energy of 5.9 kcal/mol; the next most stable is isomer 1 with a relative energy of 7.1 kcal/mol. Isomers 2, 4 and 7 have relative energies of 38.6 kcal/mol, 32.2 kcal/mol and 31.1 kcal/mol respectively. Transition states TS13, TS24, TS35, and TS67 have relative energies of 15.4 kcal/mol,

43.3 kcal/mol, 5.9 kcal/mol and 33.0 kcal/mol respectively. CR-CCSD(T) single point energy calculations, using cc-pVDZ and cc-pVTZ basis sets, were done on the B3LYP optimized structures, and the following result were obtained. Isomer 1 became the most stable with a relative energy of -12.0 kcal/mol and -19.1 kcal/mol respectively; the next most stable isomer was isomer 3 with a relative energy of -5.7 kcal/mol and -14.1 kcal/mol, then isomers 5, 2, 4, and 7 with relative energies as follows: isomer 5, -0.54 kcal/mol and -8.1 kcal/mol, isomer 2, 9.0 kcal/mol and 9.1 kcal/mol, isomer 4, 25.2 kcal/mol and 26.8 kcal/mol and isomer 7, 36.4 kcal/mol and 38.8 kcal/mol respectively. The relative energies of the transition states are as follows: TS13, 3.3 kcal/mol and -3.5 kcal/mol; TS35, -0.27 kcal/mol and -7.7 kcal/mol; TS24, 41.9 kcal/mol and 41.5 kcal/mol; and TS67, 38.6 kcal/mol and 40.6 kcal/mol respectively (Table 24).

The presence of multiple energetically close structures and the existence of low barriers between the minima for both diarsenic trioxide (As_2O_3) (e.g., isomers 3 and 4, with relative energies of 2.8 kcal/mol and 2.6 kcal/mol respectively and barrier height of 3.4 kcal/mol), and diarsenic pentaoxide (As_2O_5) (e.g., isomers 3 and 5, with relative energies of -5.7 kcal/mol and -0.54 kcal/mol respectively and having barrier height of -0.27 kcal/mol) suggests that mechanistic studies of these species should take into account their isomerizations. This is particularly important to consider when studies with elevated temperatures are performed, as e.g., would be relevant for some coal flue gas studies.

Reaction energies of dimeric arsenic oxides

The B3LYP energies were used to calculate the reaction energies of the oxidation of As and the monomeric arsenic oxides to produce dimeric arsenic oxides. The reaction

of the monomeric arsenic oxides to produce the dimeric oxides was also examined and predictions of the most stable oxide and plausible reactions were made. The obtained results are given in Table 29, and suggest that the formation of both As_2O_3 and As_2O_5 are favored from the monomeric oxides, but As_2O_3 (heat of reaction, -78.8 kcal/mol) tends to be slightly more stable than As_2O_5 (heat of reaction, -58.9 kcal/mol). At the CR-CCSD(T) level of theory, convergence for some of the monomeric oxides was not attained, so that we were unable to use this method to predict the stability of dimeric oxides.

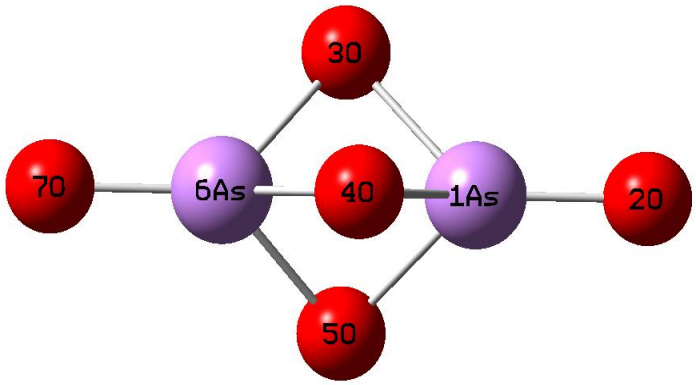

Figure 28. Diarsenic pentaoxide (As_2O_5).

Table 24. Relative energies of diarsenic pentaoxide (As_2O_5) optimized structures.

Molecule	Sym	6-311G*	cc-pVDZ	cc-pVTZ
		B3LYP	CR-CCSD(T)	
Isomer 1	D_{3h}	7.1	-12.0	-19.1
TS 13	C_s	15.4	3.3	-3.5
Isomer 3	C_{2v}	4.2	-5.7	-14.1
Isomer 4	C_s	32.2	25.2	26.8
TS 24	C_s	43.3	41.9	41.5
Isomer 2	C_s	38.6	9.0	9.1
Isomer 6	C_s	0.0	0.0	0.0
TS 67	C_1	33.0	38.6	40.6
Isomer 7	C_1	31.1	36.4	38.8
TS 53	C_s	5.9	-0.3	-7.7
Isomer 5	C_1	5.9	-0.5	-8.1

Table 25. Vibrational frequencies of diarsenic pentaoxide (As_2O_5) compounds obtained at the B3LYP/6-311G* level of theory.

Frequencies/ As_2O_5	1 (D_{3h})	3 (C_s)	4 (C_{2v})	5 (C_s)	6(C_1)	8 (C_s)	11
1	174.1	33.5	80.2	67.2	28.5	197.3	39.4
2	174.1	168.9	96.5	70.1	40.7	199.9	72.5
3	175.4	172.1	189.0	154.4	76.3	234.5	111.0
4	175.4	299.1	193.2	175.0	201.8	330.2	167.8
5	345.0	369.3	223.8	202.4	223.1	340.9	200.7
6	345.0	380.2	242.2	252.1	228.5	383.7	238.5
7	399.5	442.6	321.5	310.8	288.9	416.7	247.9
8	441.0	443.3	331.1	321.3	309.8	447.9	306.6
9	441.0	525.8	349.1	400.8	336.5	538.9	387.7
10	532.6	589.0	479.2	574.5	549.6	577.5	534.8
11	673.4	623.9	810.4	623.9	716.0	632.2	626.0
12	673.4	670.7	818.3	808.6	909.6	657.0	852.5
13	728.6	672.0	919.1	840.1	928.5	714.0	899.1
14	1004.0	747.9	1025.4	899.2	1038.1	846.4	1015.4
15	1025.2	862.6	1042.5	1036.6	1049.5	1014.9	1022.7

Table 26. Optimized geometries of diarsenic pentaoxide (As_2O_5) isomers at the B3LYP/6-311G* level of theory.

Isomers	1	3	4	5	6	8	11
$R_{O2\text{-}As1}$	1.603	1.757	1.611	1.765	1.611	1.868	1.630
$R_{O3\text{-}As1}$	1.852	1.899	1.611	3.608	1.822	1.849	1.795
$R_{O5\text{-}As1}$	1.852	1.812	2.071	1.677	1.611	1.849	1.612
$R_{O3\text{-}As6}$	1.852	1.818	3.647	1.604	1.771	1.816	-
$R_{O4\text{-}As6}$	1.852	1.901	1.693	2.212	1.623	1.836	1.912
$R_{O7\text{-}As6}$	1.603	-	1.604	-	1.609	1.606	1.611
$R_{O7\text{-}As1}$	-	1.777	-	1.765	-	-	-
$\angle O_5As_6O_3$	-	82.0	-	103.3	-	83.6	-
$\angle O_5As_1O_3$	83.6	82.2	105.8	-	110.6	91.3	114.0
$\angle As_1O_4\ As_6$	79.4	80.8	93.9	92.8	-	-	-
$\angle O_4As_6O_7$	129.7	-	93.9	-	139.5	119.8	99.6
$\angle O_4As_1O_7$	-	112.2	-	123.6	-	-	-
$\angle O_2As_1O_4\ As_6$	-	145.2	102.7	144.7	-	-	-
$\angle O_2As_1O_3\ As_6$	-	-	-	-	95.4	61.0	-10.2

Table 27. Vibrational frequencies of diarsenic pentaoxide (As_2O_5) transition states obtained at the B3LYP/6-311G* level of theory.

Frequencies/As_2O_5	TS 13	TS 35	TS 24	TS 67
1	-162.6	-188.1	-29.0	-106.5
2	105.5	114.5	52.2	100.9
3	160.1	137.6	88.8	126.1
4	193.6	140.3	200.0	166.7
5	237.7	319.2	222.3	189.6
6	317.7	345.5	229.6	206.7
7	368.5	372.9	289.6	261.0
8	369.7	397.9	312.5	322.4
9	401.4	429.2	341.3	373.4
10	476.4	587.4	563.1	431.1
11	751.1	626.3	707.6	658.5
12	754.9	756.4	904.2	813.6
13	841.3	767.4	927.0	867.5
14	1019.9	878.2	1035.2	1004.1
15	1033.6	884.1	1048.8	1018.2

Table 28. Optimize geometries of diarsenic pentaoxide (As_2O_5) transition states at the B3LYP/6-311G* level of theory.

Transition states	TS 13	TS 35	TS 24	TS 67
$R_{O2\text{-}As1}$	1.605	1.756	1.610	1.657
$R_{O3\text{-}As1}$	1.664	-	1.610	1.764
$R_{O3\text{-}As6}$	-	1.670	-	-
$R_{O4\text{-}As1}$	-	1.723	1.836	1.611
$R_{O5\text{-}As1}$	-	1.723	-	-
$R_{O5\text{-}As6}$	1.732	-	1.628	2.027
$R_{O4\text{-}As6}$	1.732	-	1.765	-
$R_{O7\text{-}As6}$	1.601	-	1.608	1.610
$R_{O7\text{-}As1}$	-	1.767	-	-
$\angle As_1As_6O_3$	-	65.9	-	-
$\angle O_2As_1O_3$	141.0	-	138.8	107.1
$\angle As_1O_4\ As_6$	-	-	111.8	-
$\angle O_5As_6O_7$	132.2	-	139.6	101.1
$\angle O_4As_1O_7$	-	119.3	-	-
$\angle O_2As_1As_6\ O_4$	66.1	114.4	-	-

Table 29. Arsenic oxides: reaction energies (kcal/mol).

Reaction	B3LYP	CR-CCSD(T)	
		cc-pVDZ	cc-pVTZ
$As\ (X\ ^4S) + \frac{1}{2} O_2\ (X\ ^3\Sigma^-) \rightarrow AsO\ (X\ ^2\Pi)$	-47.9	-34.2	-47.5
$AsO\ (X\ ^2\Pi) + \frac{1}{2} O_2\ (X\ ^3\Sigma^-) \rightarrow AsO_2\ (X\ ^2A_1)$	-22.0	-17.9	-26.8
$AsO\ (X\ ^2\Pi) + O_2\ (X\ ^3\Sigma^-) \rightarrow AsO_3\ (X\ ^2B_2)$	-17.4	-	-
$AsO_2\ (X\ ^2A_1) + \frac{1}{2} O_2\ (X\ ^3\Sigma^-) \rightarrow AsO_3\ (X\ ^2B_2)$	4.7	-	-
$AsO\ (X\ ^2\Pi) + AsO_2\ (X\ ^2A_1) \rightarrow As_2O_3\ (X\ ^1A')$	-78.8	-	-
$AsO_2\ (X\ ^2A_1) + AsO_3\ (X\ ^2B_2) \rightarrow As_2O_5\ (X\ ^1A_1')$	-58.9	-	-
$As_2O_3\ (X\ ^1A') + O_2\ (X\ ^3\Sigma^-) \rightarrow As_2O_5\ (X\ ^1A_1')$	2.5	-	-

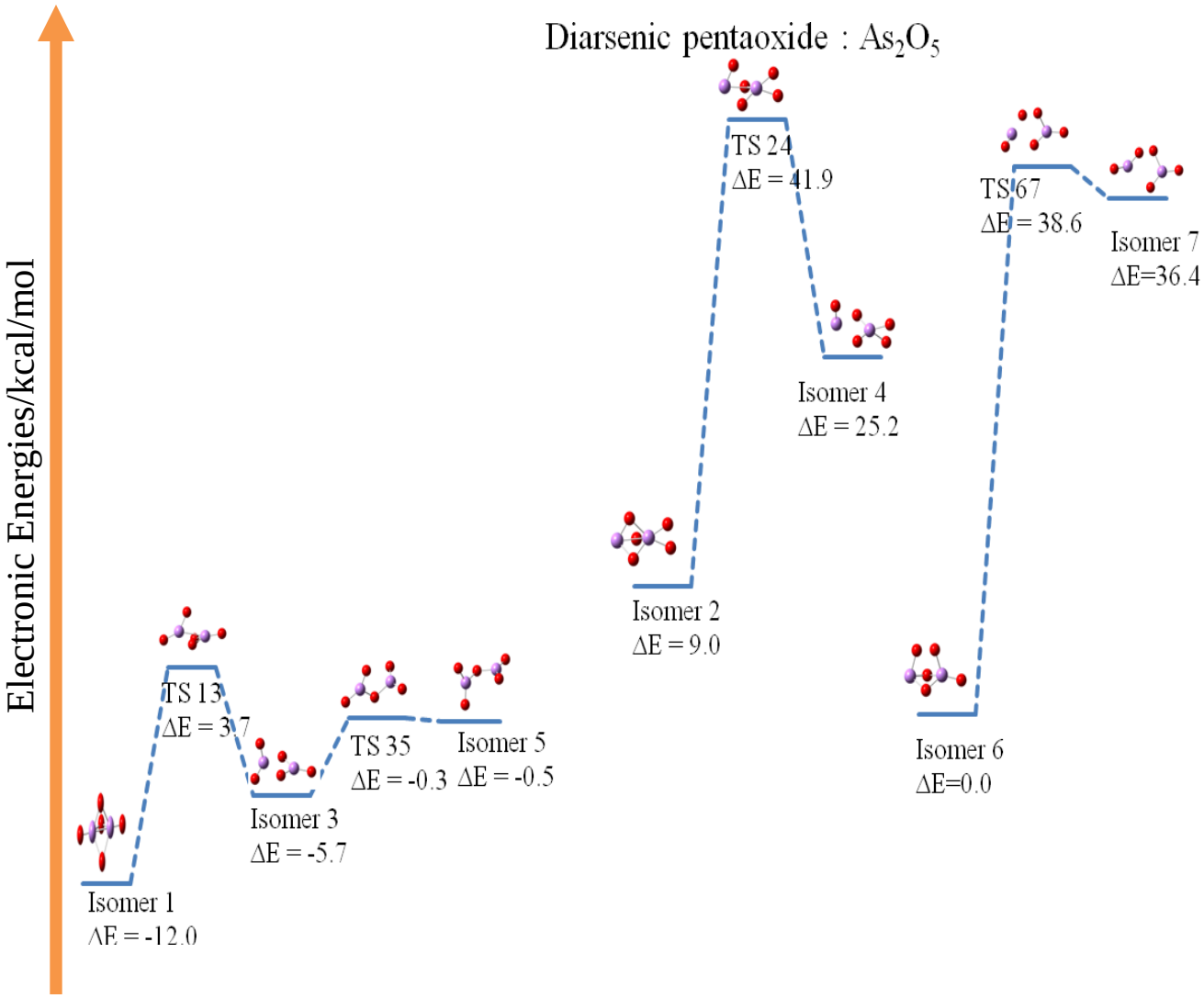

Figure 29. Relative energies of diarsenic pentaoxide (As_2O_5) compounds and transition states.

Summary

Spectroscopic constants predicted for AsO by GVVPT2/cc-pVTZ are in good agreement with those obtained experimentally. The equilibrium geometries for the electronic ground states for AsO_2 and AsO_3 were located. The corresponding dissociation limits, and the binding energies of the monomeric oxides, were calculated. The monomeric trioxide was predicted as the most stable monomeric oxide from

GVVPT2 studies with reaction enthalpy of -65.2 kcal/mol obtained from the oxidation of AsO. The dimeric oxides, As_2O_3 and As_2O_5 are favored over the monomeric arsenic oxides (i.e., the reaction energies are -78.8 kcal/mol for As_2O_3 and -58.9 for As_2O_5 at the B3LYP level of theory), with As_2O_3 predicted to be the most stable form, but by a small amount. The most stable As_2O_3 structure predicted from the CR-CCSD(T) studies with both the use of cc-pVDZ and cc-pVTZ basis was isomer 1, i.e., the cage form. The relative energies of all the other isomers were higher. The relative energies for isomer 2 were higher than that of isomer 1 by 6.0 kcal/mol and 4.5 kcal/mol when calculated with the cc-pvDZ and cc-pVTZ basis sets, that for isomer 3 were 2.8 kcal/mol and 2.2 kcal/mol higher and those for isomer 4 were 2.6 kcal/mol and 2.0 kcal/mol higher also. The predicted barrier height between isomer 1 and 2 is 21.5 kcal/mol and 18.2 kcal/mol with the use of cc-pVDZ and cc-pVTZ basis sets respectively. The barrier heights for isomers 2 and 3, and 3 and 4, were less than 5 kcal/mol. For diarsenic pentaoxide (As_2O_5), isomer 1 was predicted to be the most stable, having the lowest relative energies (-12.0 kcal/mol and -19.1 kcal/mol) with respect to reference isomer 6 using both the cc-pVDZ and cc-pVTZ basis sets. The predicted barrier height between isomers 1 and 3 is 3.7 kcal/mol and 2.5 kcal/mol for the two basis sets. These energy barriers can easily be surmounted, and partially so when these reactions occur at high temperatures. Thus the possibility of multiple reactions and reaction pathways are predicted.

CHAPTER VI

THEORETICAL STUDY OF SELENIUM OXIDES

Introduction

The collection, processing, and combustion of coal for the production of electricity are some of the largest means by which trace elements, including selenium, are released into the environment [41]. This has led to an increasing interest in the thermodynamic stabilities and kinetic reactivities of compounds, and especially oxides, of the emitted trace elements. In turn, such information can give insight into strategies to mitigate a particular trace element's effects on the environment, including human health. In particular, one desires as complete as possible understanding of the chemical forms, structures, and oxidation states of the trace element [54, 55, 171]. Selenium is one of the trace elements that is released in greatest abundance with flue gases during coal combustion because of its relatively high volatility compared to other trace elements [62, 172, 173]. Selenium is known to have the following oxidation numbers: -2, 0, +2, +4, and +6; [41, 62] and consequently supports a wide variety of bonding environments. Although selenium is an essential trace element, because it protects the cell membrane and can act as an antioxidant [55], high concentrations of selenium are known to be harmful. However, the margin between the essential quantity and the toxic is small for selenium [41, 55, 174]. Since the toxicity of selenium depends on its form and concentration, there is particular need to fully understand the species, oxidation states,

and relative abundances in which selenium exists in the environment. Selenium is released into the atmosphere as Se, SeO, and SeO_2 [41, 44, 60, 62]. The selenium oxides, SeO [175-177], SeO_2 [64, 178-180], and SeO_3 [63, 181, 182] have been studied experimentally, but theoretical studies are limited [49, 164, 183]. From consideration of sulfur chemistry, it can be expected that polymeric forms of the most abundant oxides exist and may be relevant in understanding the environmental chemistry [184-186]. However, to the best of our knowledge, little is known, either experimentally or theoretically, about the dimeric selenium oxides.

High-level theoretical methods that provide a balanced treatment of both dynamic and nondynamic electron correlation are expected to be needed for the characterization of especially the dimeric oxides. Because so little was known about the possible isomers of relevance to this study, a variety of electronic structure methods were used, with GVVPT2 used as appropriate. For both the monomeric and dimeric selenium oxides, optimized geometries (i.e., minima and transition states) were obtained at the B3LYP/6-311G* DFT level of theory [6, 7]. At these equilibrium geometries, CR-CCSD(T) calculations [50-53] with the use of cc-pVDZ and cc-pVTZ basis were performed to obtain accurate energies. Geometry optimizations were also performed on the monomeric oxides using GVVPT2 and compared with the B3LYP results. On the B3LYP optimized geometries, GVVPT2 calculations were done and the results compared to those obtained at the CR-CCSD(T) level of theory. Using GVVPT2 as the second step in a composite calculation was recently successfully used by Mbote et al. [170]. The optimized structures of both the isomers and the transition states of dimeric oxides had: C_2, C_{2v}, C_s, or only C_1 symmetry. For the prediction of the vibrational spectroscopy and

to confirm the curvature of the potential energy surfaces at the stationary points, harmonic frequency calculations were performed. A local electronic structure software suite (i.e., UNDMOL) was used to perform GVVPT2 calculations. Gaussian 03 [141] was used for B3LYP optimization, and GAMESS US [144, 145] was used for the CR-CCSD(T) studies.

There are four sections in this chapter. Section 2 is composed of a review of the GVVPT2 method and also a detailed description of the reference spaces used for this work. In Section 3, the results are presented and discussed. Finally, Section 4 provides a summary.

Computational details

The model spaces used for the GVVPT2 calculations in this study were of the MCSCF complete active space variety. The model space was denoted as follows, *(m|n)*, where *m* is the number of orbitals and *n* is the number of electrons. In a complete active space calculation, all possible configurations are allowed.

The monomeric selenium oxides, SeO, and SeO_2, were studied using C_{2v} symmetry, while SeO_3 was studied in C_{2v} and D_{3h} symmetry. The active spaces used consisted of the most important highest occupied molecular orbitals, G_1 (i.e., G_1 = {HOMO, HOMO-1, ……}) and the low-lying unoccupied molecular orbitals, G_2 (i.e., G_2 = {LUMO, LUMO+1…..}). Initial active spaces were derived from a simple valence picture, but needed to be expanded. For SeO, the set of 6 valence molecular orbitals (i.e., 2p orbitals of O, and the 4p orbitals of Se) having 8 electrons, were divided into two subgroups: $G_1 = (5b_2\ 4b_2\ 5b_1\ 4b_1\ 11a_1)$, and $G_2 = (12a_1)$. The SeO_2 molecule had in its

active space 10 valence orbitals (i.e., the 2p of each O, and 4s and 4p of selenium), which were divided in two subgroups as follows: G_1 = ($7b_2$ $6b_2$ $4b_1$ $2a_2$ $12a_1$ $11a_1$ $10a_1$), and G_2 = ($8b_2$ $5b_1$ $13a_1$), and 14 active electrons were distributed. For SeO_3, 13 active orbitals (i.e., the 2p of each O, and the 4s and 4p of Se) containing 18 electrons, were divided in two subgroups: G_1 = ($8b_2$ $7b_2$ $6b_2$ $5b_1$ $4b_1$ $2a_2$ $14a_1$ $13a_1$ $12a_1$) and G_2 = ($9b_2$ $6b_1$ $16a_1$ $15a_1$). The described calculations can be performed by the current GUGA-based GVVPT2 program in UNDMOL [135] in reasonable times; as an example, 2 min 16 sec is required to run a typical GVVPT2 calculation with a total of 21.2 million CSF's and 504 model space CSF on a 2.0 GHZ dual-core Opteron processor 2212.

Results and discussion

Monomeric selenium oxides

Selenium monoxide (SeO)

Molecular parameters and the spectroscopic constants calculated for SeO, which has a ground state symmetry of $^3A_2$, using the MCSCF and GVVPT2 method and the cc-pVDZ and cc-pVTZ basis sets and experimental data for the ground state are shown in Table 30. The cc-pVTZ gave results in closer agreement with experiment (e.g., the bond lengths r_e for MCSCF results are greater than the experimental by +0.019 Å and that of the GVVPT2 are less, by -0.010 Å), than did the cc-pVDZ basis (i.e., the MCSCF and the GVVPT2 results are greater than experimental by +0.051 Å and +0.022 Å, respectively, for the equilibrium bond length r_e), harmonic frequency ω_e, and rotational constant B_e at both levels of theory. GVVPT2 results are most significantly improved over MCSCF relative to the experimental results for r_e and B_e. The predicted value for the dissociation energy D_e, by the GVVPT2/cc-pVTZ method with the *(6|8)* model space is 104.3

kcal/mol as opposed to 70.0 kcal/mol for MCSCF. The r_e obtained at the B3LYP/6-311G* level of theory is longer than that at the GVVPT2/cc-pVTZ level of theory by 0.025 Å (Table 32), and is similar to the MCSCF result.

Table 30. Some thermodynamic constants for the ground state ($^3A_2$) of SeO.

Method	r_e (Å)	ω_e (cm^{-1})	D_e (kcal/mol)
MCSCF(6|8)/cc-pVDZ	1.699	803.9	62.5
MCSCF(6|8)/cc-pVTZ	1.667	855.3	70.0
GVVPT2(6|8)/cc-pVDZ	1.670	878.6	87.9
GVVPT2(6|8)/cc-pVTZ	1.638	947.7	104.3
Exp.[a,b]	1.648 (1.633)	914.69 (915.43)	

[a] Ref. [175, 176].

[b] The values for the $X_1\,^3\Sigma^-_{0+}$, and $X_2\,^3\Sigma^-_1$ states with the latter in parenthesis.

Selenium dioxide (SeO_2)

Since GVVPT2/cc-pVTZ gave results which agreed with experimental ones noticeably better than cc-pVDZ did for SeO, only the cc-pVTZ basis set was used for SeO_2 geometry optimization. The molecular symmetry was C_{2v} and the ground state wave function had $^1A_1$ symmetry. The r_1 (O—Se) bond length and the $\angle$OSeO bond angle agree well, probably fortuitously, with those of experiment (Table 31). The differences in r_1 bond length for the GVVPT2/cc-pVTZ method using the following model spaces (7|10), and (10|14) to that of experiment are about 0.001 Å and 0.004 Å,

respectively, and are both within the experimental error bar. The B3LYP/6-311G* results (cf. Table 32) agree with those of GVVPT2/cc-pVTZ using the (10|14) model space by approximately 0.01 Å. The MCSCF, GVVPT2 and CR-CCSD(T) methods predicted that the formation of SeO_2 from oxidation of SeO is favorable, having reaction energies of -73.3 kcal/mol, -63.1 kcal/mol and -31.1 kcal/mol respectively (Table 36 and 43). The MCSCF, GVVPT2 and B3LYP predicted harmonic frequencies for SeO_2 are in good agreement with experimental values for the vibrations of the ground state (Table 34).

Table 31. Optimized geometries and experimental values for selenium dioxide (SeO_2) at the GVVPT2/cc-pVTZ level of theory.

Oxides	Symmetry	Active space	r_1(Å)	r_2(Å)	θ (degree)
	$^1A_1$	(7|10)	1.608	-	113.2
	$^1A_1$	(10|14)	1.612	-	115.2
	$^1A_1$ (exp.)[a]		1.607±0.006	-	113.50±0.05

[a] From Ref. [64].

Table 32. Comparison of B3LYP/6-311G* structures to that of GVVPT2/cc-pVTZ of monomeric selenium oxides.

	Parameters	B3LYP	GVVPT2
SeO	r_1(Å)	1.663	1.638
SeO_2	r_1(Å)	1.622	1.612
	θ (Degrees)	115.1	115.2
SeO_3	r_1(Å)	1.6135	1.598
	r_2(Å)	1.6134	1.608
	θ (Degrees)	120.1	120.6

Table 33. Harmonic frequencies (cm^{-1}) of selenium dioxide (SeO_2).

Oxides	Symmetry	Method	$\omega_1(a_1)$	$\omega_2(a_1)$	ω_3 (b_2)
SeO_2	$^1A_1$	MCSCF	931.3	373.2	993.9
	$^1A_1$	GVVPT2	959.6	378.2	985.9
	$^1A_1$	B3LYP	924.6	358.3	965.4
	Exp.		920.0[a]	364.0[a]	968[a]

[a] From Ref. [180].

Selenium trioxide (SeO_3)

The predicted Se—O bond lengths for SeO_3 (Figure 31), 1.598 Å in D_{3h} symmetry, are shorter than the experimental value of r_1, 1.6878 Å [63] (Table 33). By relaxing one bond length and optimizing the molecular geometry in C_{2v} symmetry, the

obtained bond length was found to be close to the optimized one for the $^1A_1'$ electronic state to within 0.01 Å. Optimization at the B3LYP/6-311G* level of theory gave bond lengths which are in good agreement with GVVPT2/cc-pVTZ results, for both r_1 and r_2 bond lengths; they differ by 0.016 Å and 0.005 Å respectively. The ∠OSeO bond angle is less than that of GVVPT2 by -0.5°. The B3LYP/6-311G* bond lengths are shorter by -0.0743 Å than those obtained experimentally; they are shown in Table 32 and 33. Because of the close agreement of theoretical values and the disagreement with experiment, further calculations and experimental studies are needed to establish definitely the equilibrium geometry of monomeric SeO_3. The MCSCF, GVVPT2 and CR-CCSD(T) methods predicts that the formation of SeO_3 from the oxidation of SeO is favorable having reaction energies of -64.4 kcal/mol and -67.1 kcal/mol and -20.5 kcal/mol respectively. But the formation of SeO_3 from the oxidation of SeO_2 oxide is not favorable, based on predicting by the MCSCF and CR-CCSD(T) methods, having energies of reaction of +8.7 kcal/mol and +10.6 kcal/mol. The GVVPT2 method predicts this reaction energy to be very slightly exothermic, -4.0 kcal/mol (Table 36 and 43).

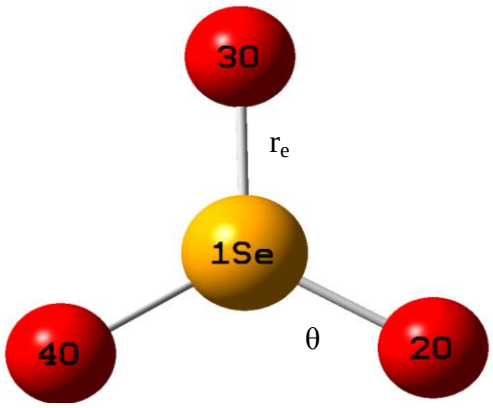

Figure 30. Selenium trioxide (SeO_3).

Table 34. Optimized geometries at GVVPT2/cc-pVTZ level of theory and experimental values for selenium trioxide (SeO_3).

Oxides	Symmetry	Active space	r_1(Å)	r_2(Å)	θ (degree)
SeO_3	$^1A_1$ (C_{2v})	(7|8)	1.586	1.557	121.3
	$^1A_1$ (C_{2v})	(12|18)	1.574	1.608	120.6
	$^1A_1'$ (D_{3h})	(12|18)	1.598		
	exp. (D_{3h})		1.6878±0.0002 [a]		
			1.69±0.01 [b]		

[a] The experimental value is for r_0, from Ref. [63].
[b] From Ref. [181].

Reaction enthalpies for the oxidation of monoxides and dioxides of selenium

The binding energies of the selenium oxides and O_2 are shown in Table 35. These results were used to calculate the reaction enthalpies given in Table 36. The order of stability predicted by the GVVPT2 method is as follows:

$$SeO_3 \gtrsim SeO_2 > SeO$$

I.e., SeO_3 was found to be more stable or having almost the same stability as SeO_2, and the least stable is seen to be SeO.

Table 35. Total binding energies (kcal/mol) of the monomeric selenium oxides.

Molecules	Symmetry	MCSCF	GVVPT2
O_2	$X\,^3\Sigma_g^-$	-88.2	-122.0
SeO	$X\,^3\Sigma^-$	-70.0	-104.3
SeO_2	$^1A_1$	-187.2	-228.4
SeO_3	$^1A_1'$	-222.6	-293.4

Table 36. Reaction enthalpies (kcal/mol) for the oxidation of monomeric selenium oxides.

Reaction	MCSCF	GVVPT2
$SeO(X\,^3\Sigma^-) + ½\ O_2 \rightarrow SeO_2\ (^1A_1)$	-73.1	-63.1
$SeO(X\,^3\Sigma^-) + O_2 \rightarrow SeO_3(^1A_1)$	-64.4	-67.1
$SeO_2(^1A_1) + ½\ O_2 \rightarrow SeO_3(^1A_1)$	8.7	-4.0

Dimeric Selenium Oxide

Based on the results for the monomeric selenium oxides, studies on dimeric oxides were done using the B3LYP variant of DFT with the 6-311G* basis set and CR-CCSD(T) with the use of cc-pVDZ and cc-pVTZ basis sets. B3LYP was used to optimize geometries. At the B3LYP optimized geometries, CR-CCSD(T) calculations were performed to obtain accurate energies.

Diselenium trioxide (Se_2O_3)

In the study of the diselenium trioxide (Se_2O_3) molecule (Figure 32), three minima were observed: isomers 1, 2, and 3, and two transition states: TS13 and TS23 (Figures 34 and Table 37); no cage structures were observed. The $R_{O4\text{-}Se2}$ and $R_{O5\text{-}Se3}$ bonds of Se_2O_3 isomers and transition states are longer than the r_e bond length of SeO_2 (i.e., 0.005 Å – 0.023 Å longer) and SeO_3 (0.009 Å – 0.045 Å longer) obtained at the B3LYP level of theory, but shorter than that of SeO (0.005 Å – 0.036 Å shorter). The $R_{O1\text{-}Se2}$ and $R_{O1\text{-}Se3}$ bond lengths are all longer than the r_e bond length of SeO, SeO_2 and SeO_3, (i.e., from 0.293 Å – 1.117 Å longer), but the $R_{O1\text{-}Se3}$ bond of TS13, is shorter by 0.007 Å to that of SeO. The $\angle O_5Se_3O_1$ and $\angle O_1Se_2O_4$ angles of Se_2O_3 are smaller than those of SeO_2 and SeO_3, except for the $\angle O_1Se_2O_4$ angle of TS13 which is 36.8° larger than that of SeO_2 and 30.8° larger than that of SeO_3 (Table 32 and 38).

The harmonic frequencies for Se_2O_3 (i.e., the modes dominated by Se_2—O_4 and Se_3—O_5 stretching, and O_4—Se_2—O_1 and O_5—Se_3—O_1 wagging frequencies), agree well with those of SeO_2. The frequencies of these isomers and their transition states, calculated at the B3LYP/6-311G* level, are shown in Table 39. Since the bond lengths and bond angles of the different structures are similar, (e.g., the $R_{O4\text{-}Se2}$ and $R_{O5\text{-}Se3}$ bond lengths of all the different structures differ by 0.005 Å and the $\angle O_5Se_3O_1$ angles by 7.0°) the possibility of isomerization was further examined using energy differences.

At the B3LYP level of theory, diselenium trioxide isomer 1, with C_2 symmetry, was the most stable, followed by isomer 3, having C_s symmetry and relative energy of 2.74 kcal/mol to isomer 1; the least stable was found to be isomer 2 with C_s symmetry, having a relative energy of 9.09 kcal/mol to isomer 1. However, at the CR-CCSD(T)

level of theory, with the use of the cc-pVDZ basis set, diselenium trioxide isomer 2 is the most stable having a relative energy of -2.31 kcal/mol to isomer 1, followed by isomer 1, and the least stable is isomer 3 with a relative energy of 2.22 kcal/mol to isomer 1. But with the cc-pVTZ basis, there is some rearrangement in the stabilities; diselenium trioxide isomer 1 is again predicted to be the most stable, and then, almost isoenergic, to isomer 2 having a relative energy to isomer 1 of 0.89 kcal/mol; isomer 3 was found to be the least stable with relative energy of 1.94 kcal/mol. The barrier height between isomer 1 and 3, TS13, and that between isomer 2 and 3, TS23, at the B3LYP level are 29.95 kcal/mol and 18.02 kcal/mol respectively. The barrier heights decreased with the use of the CR-CCSD(T) method. With the cc-pVDZ basis, the barrier heights were 26.19 kcal/mol and 7.17 kcal/mol and when the cc-pVTZ basis was used the barrier heights increased slightly to 28.75 kcal/mol and 12.28 kcal/mol (Table 37).

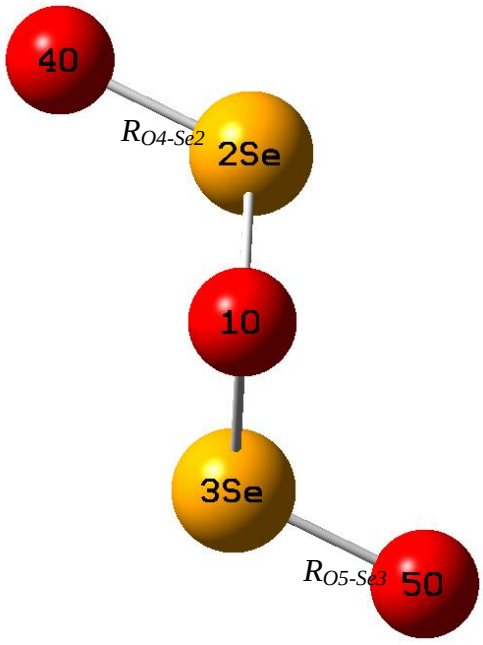

Figure 31. Diselenium trioxide (Se_2O_3).

Table 37. Relative energies of diselenium trioxides (Se_2O_3) isomers in kcal/mol.

	Sym	6-311G*	cc-pVDZ	cc-pVTZ
Molecule		B3LYP	CR-CCSD(T)	
isomer 2	C_s	9.09	-2.13	0.89
TS 23	C_1	18.02	7.17	12.28
isomer 3	C_s	2.74	2.22	1.94
TS 13	C_1	29.95	26.19	28.75
isomer 1	C_2	0.00	0.00	0.00

Table 38. Optimized geometries of diselenium trioxide (Se_2O_3) isomers and transition states at the B3LYP/6-311G* level of theory.

Isomer	1	2	3	TS13	TS23
$R_{O1\text{-}Se2}$	1.879	1.806	1.884	2.720	1.875
$R_{O4\text{-}Se2}$	1.627	1.658	1.626	1.638	1.641
$R_{O1\text{-}Se3}$	1.879	1.850	1.884	1.656	1.839
$R_{O5\text{-}Se3}$	1.627	1.631	1.626	1.649	1.632
$\angle O_5Se_3O_1$	109.03	103.63	110.0	109.8	106.8
$\angle Se_3O_1\,Se_2$	86.21	116.50	85.83	71.9	113.3
$\angle O_1Se_2O_4$	109.03	99.60	110.0	151.9	111.9

Table 39. Vibrational frequency of diselenium trioxide (Se_2O_3) isomers/transition states (in cm^{-1}) calculated using B3LYP/6-311G*.

Se_2O_3 Frequencies	1 (C_2)	2 (C_s)	3 (C_s)	TS13	TS23
1	125.28 (B)	69.394 (A')	109.24(A')	-174.64 (A)	-127.81 (A)
2	127.63 (A)	83.549 (A")	166.10 (A")	80.966 (A)	112.33 (A)
3	208.49 (A)	217.28 (A')	221.11 (A')	119.66 (A)	149.89 (A)
4	274.58 (A)	229.06 (A")	247.21 (A")	131.25 (A)	235.27 (A)
5	333.85 (B)	302.68 (A')	318.64 (A')	227.94 (A)	294.97 (A)
6	394.18 (B)	483.99 (A')	377.83(A")	349.38 (A)	387.31 (A)
7	623.77 (A)	570.84 (A')	608.48 (A')	841.70 (A)	531.33 (A)
8	924.93 (B)	860.17 (A')	922.46(A")	873.92 (A)	894.23 (A)
9	941.36 (A)	923.48 (A')	948.96 (A')	919.25 (A)	922.71 (A)

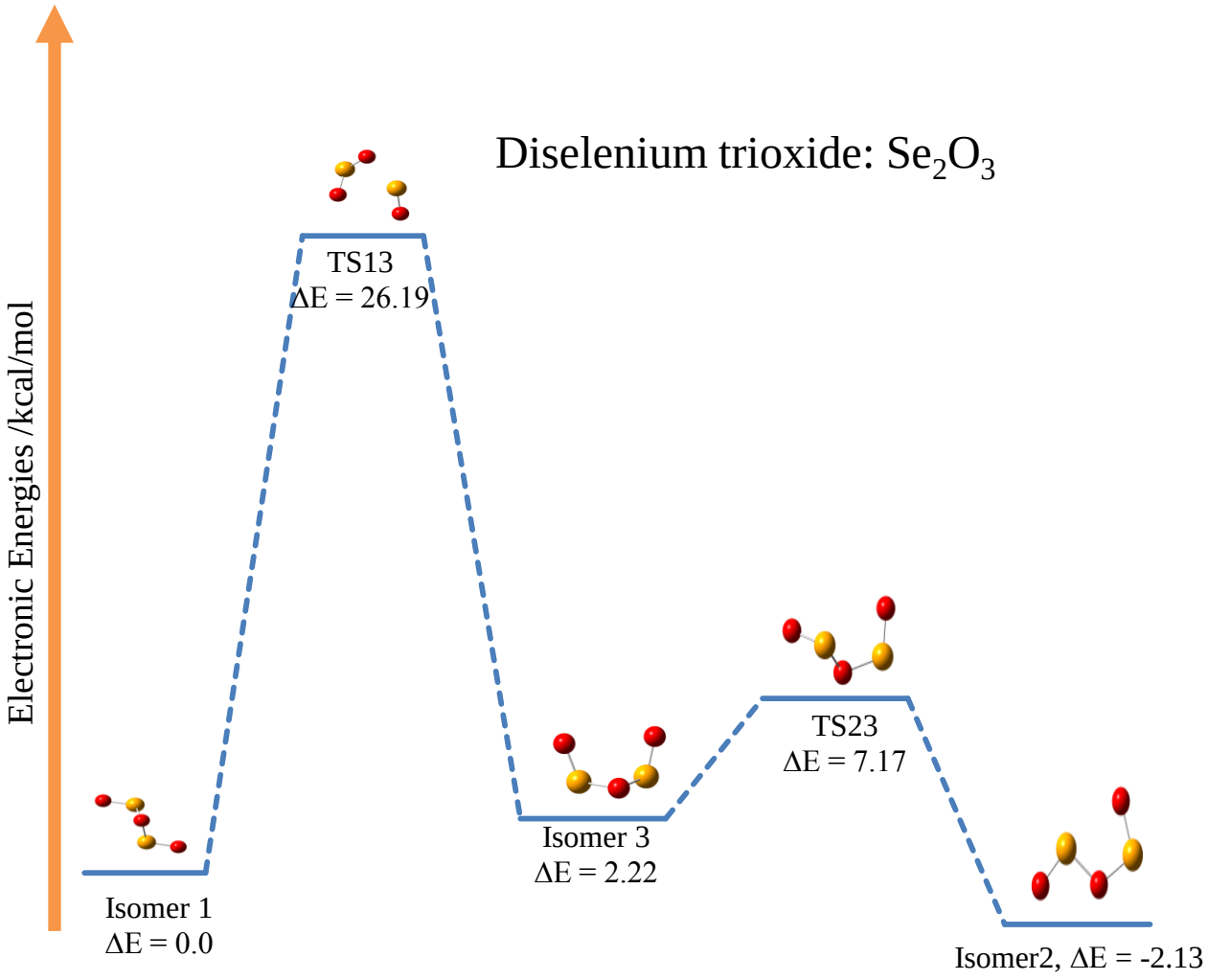

Figure 32. Relative energies of diselenium trioxide (Se_2O_3) isomers and transition states in kcal/mol.

Diselenium pentaoxide (Se_2O_5)

The study of diselenuim pentaoxide (Se_2O_5) (Figure 35), using CR-CCSD(T) with both cc-pVDZ and cc-pVTZ basis sets on the B3LYP/6-311G* optimized geometries, resulted in three minima: isomers 1, 2, and 3, and one transition state between isomers 1 and 2, TS12, with a relative barrier height of 0.56 kcal/mol and 0.12 kcal/mol for each of the two basis sets (Table 40). No transition state was isolated for the transition between diselenium pentaoxide isomer 3 and the others.

The $R_{O4\text{-}Se1}$ and $R_{O7\text{-}Se5}$ bonds lengths of Se_2O_5 isomers and the found transition state are shorter than the r_e bond length of: SeO (i.e., 0.056 Å – 0.058 Å shorter), SeO_2 (i.e., 0.015 Å – 0.017 Å shorter) and SeO_3 (0.0084 Å shorter), at the B3LYP level of theory. But the $R_{O2\text{-}Se1}$, $R_{O2\text{-}Se5}$, $R_{O3\text{-}Se1}$, and $R_{O6\text{-}Se5}$ bond lengths are longer than the r_e bond length of SeO (i.e., 0.261 Å – 0.179 Å longer), SeO_2 (i.e., 0.302 Å – 0.22 Å longer) and SeO_3, (i.e., 0.3106 Å – 0.2286 Å longer). The $\angle O_4Se_1O_3$ and $\angle O_6Se_5O_7$ angles of Se_2O_5 are smaller than those of SeO_2 and SeO_3 (Table 32 and 41). The expectation of isomerization is also plausible with Se_2O_5. The bond lengths and bond angles for the isomers are approximately the same (e.g., the $R_{O4\text{-}Se1}$ and R_{O7}-Se_5 bond lengths of all the isomers differ by 0.002 Å and the $\angle Se_1O_2Se_5$ bond angles differ only by 0.1°) (Table 41).

The harmonic frequencies for Se_2O_5 (i.e., the normal modes dominated by Se_1—O_4 and Se_5—O_7 stretching, and O_3—Se_1—O_4 and O_6—Se_5—O_7 wagging frequencies) agree well with those of SeO_2. The frequencies of these isomers and their transition state calculated at the B3LYP/6-311G* level are shown in Tables 42.

The predicted most stable structure of diselenium pentaoxide, isomer 2, has relative energies of -3.27 kcal/mol and -3.95 kcal/mol to isomer 1 for each of the two basis sets, respectively. The next most stable minimum, isomer 3, has relative energies of -1.16 kcal/mol and -0.94 kcal/mol; the least stable diselenium pentaoxide isomer is 1 (Table 40). Both Se_2O_3 and Se_2O_5 have isomers that are energetically close. The low barriers between the minima suggest that isomerization should be taken into consideration in mechanistic studies of these species. This is particularly significant

when these species are considered at elevated temperatures, such as in flue gases in coal combustion.

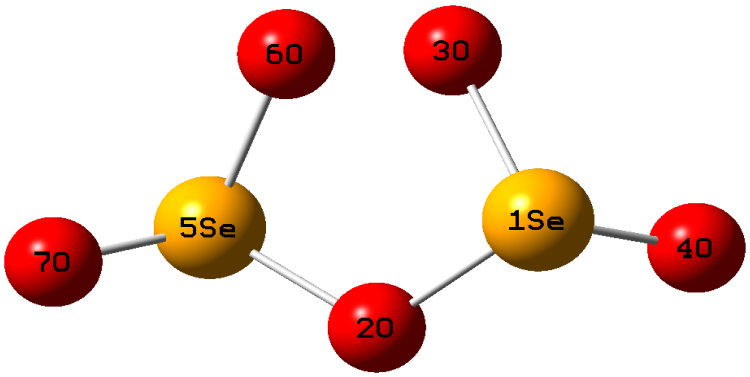

Figure 33. Diselenium pentaoxide (Se_2O_5).

Table 40. Relative energies of the diselenium pentaoxides (Se_2O_5) isomers.

		cc-pVDZ	cc-pVTZ
Molecule	B3LYP/6-311G*	CR-CCSD(T)	
isomer 1	0.00	0.00	0.00
TS 12	4.94	0.56	0.12
isomer 2	-1.49	-3.27	-3.95
isomer 3	0.05	-1.16	-0.94

Table 41. Optimized geometries of diselenium pentaoxide (Se_2O_5) isomers and transition states at the B3LYP/6-311G* level of theory.

Compounds	1	2	5	TS12
$R_{O4\text{-}Se1}$	1.606	1.607	1.605	1.606
$R_{O3\text{-}Se1}$	1.924	1.905	1.924	1.899
$R_{O2\text{-}Se1}$	1.858	1.851	1.867	1.842
$R_{O2\text{-}Se5}$	1.858	1.851	1.847	1.842
$R_{O6\text{-}Se5}$	1.924	1.905	1.918	1.899
$R_{O7\text{-}Se5}$	1.606	1.607	1.606	1.606
$\angle O_4Se_1O_3$	101.86	109.44	101.86	104.76
$\angle Se_1O_2\ Se_5$	117.98	118.43	117.44	122.22
$\angle O_6Se_5O_7$	101.86	109.44	108.94	104.76

Table 42. Frequencies of diselenium pentaoxide (Se_2O_5) minima obtained at the B3LYP/6-311G* level of theory.

Frequencies/Se_2O_5	1 (C_2)	2 (C_2)	5 (C_1)	TS12 (C_2)
1	49.543 (B)	69.64 (B)	74.988	-237.24
2	144.95 (A)	136.02(A)	142.70	14.865
3	210.30(A)	199.58(A)	212.74	174.70
4	227.50 (B)	247.43 (B)	252.43	211.30
5	238.83(A)	321.24(A)	266..37	236.32
6	304.43 (B)	322.34 (B)	319.36	315.55
7	339.13(A)	367.39(A)	349.13	327.80
8	340.71(A)	377.30 (B)	371.68	363.11
9	502.56 (B)	464.39(A)	467.05	455.46
10	505.17(A)	504.14 (B)	497.94	507.61
11	522.02(A)	523.15(A)	520.30	525.42
12	596.68(B)	597.04 (B)	592.37	612.99
13	903.83(A)	875.33(A)	896.70	890.12
14	980.40(B)	980.19 (B)	978.27	981.43
15	986.80 (B)	985.79 (B)	990.30	987.63

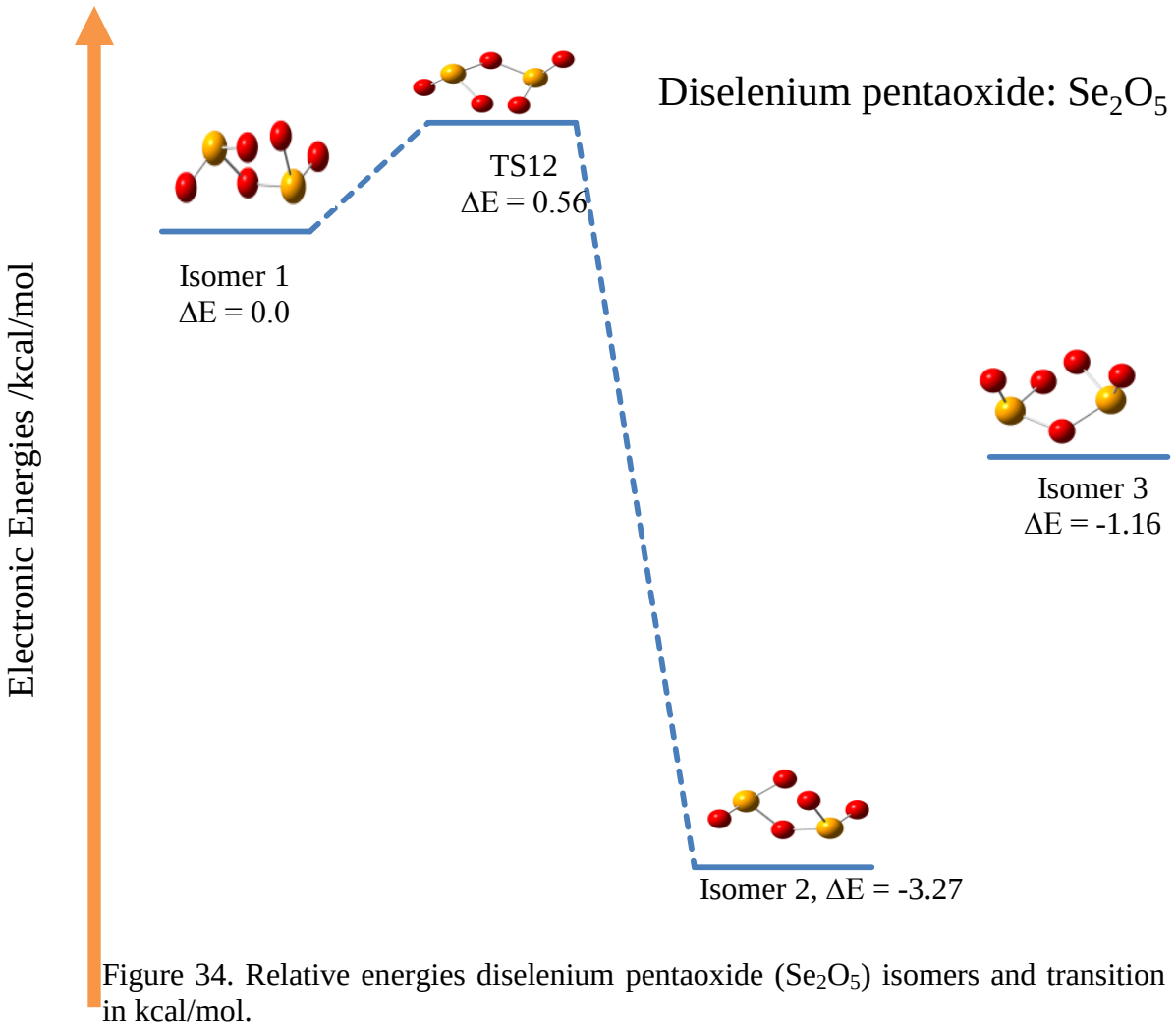

Figure 34. Relative energies diselenium pentaoxide (Se_2O_5) isomers and transition state in kcal/mol.

Reaction energies of selenium oxides

The reaction energies of oxidation for Se and the selenium monoxides using B3LYP and CR-CCSD(T) energies were used to predict the most stable oxide. At the B3LYP level of theory, the results shown in Table 43 suggest that the dimeric oxides can be formed from the monomeric oxides, with Se_2O_5 more likely to be formed as opposed to Se_2O_3. But at the CR-CCSD(T) level of theory their formation is not feasible.

Table 43. Reaction energies (kcal/mol) of selenuim oxides .

Reaction	B3LYP/6-311G*	CR-CCSD(T)	
		cc-pVDZ	cc-pVTZ
$Se\ (^3P_g) + \frac{1}{2} O_2\ (X\ ^3\Sigma^-) \rightarrow SeO\ (X\ ^3\Sigma^-)$	-38.4	-29.8	-40.6
$SeO\ (X\ ^3\Sigma^-) + \frac{1}{2} O_2\ (X\ ^3\Sigma^-) \rightarrow SeO_2\ (^1A_1)$	-24.3	-18.2	-31.1
$SeO\ (X\ ^3\Sigma^-) + O_2\ (X\ ^3\Sigma^-) \rightarrow SeO_3(^1A_1)$	-7.6	1.4	-20.4
$SeO_2\ (^1A_1) + \frac{1}{2}\ O_2\ (X\ ^3\Sigma^-) \rightarrow SeO_3\ (^1A_1)$	16.72	19.6	10.6
$SeO\ (X\ ^3\Sigma^-) + SeO_2\ (^1A_1) \rightarrow Se_2O_3\ (^1A_1)$	-10.01	-	-
$SeO_2\ (^1A_1) + SeO_3\ (X\ ^2B_2) \rightarrow Se_2O_5\ (^1A_1)$	-19.48	-	-
$Se_2O_3\ (^1A_1) + O_2\ (X\ ^3\Sigma^-) \rightarrow Se_2O_5\ (^1A_1)$	-17.05	-	-

Summary

The equilibrium geometries of SeO, SeO_2, and SeO_3 were predicted using the GVVPT2/cc-pVTZ method and those of SeO and SeO_2 are observed to be in agreement with experimentally obtained values. The relatively large deviations for SeO_3, which is also observed in B3LYP optimizations, suggest that either the electronic structure of SeO_3 is very complex, and requires MRCISD, or beyond, level calculations or that the experimental values need to be re-examined. Furthermore, the dissociation limits and binding energies for SeO_2 and SeO_3 were calculated. From the calculation, SeO_3 was observed to be the most stable, with SeO_2 being almost the same but slightly less, and then SeO. The most stable Se_2O_3 isomer predicted using CR-CCSD(T)/cc-pVDZ, was isomer 2 with relative energy of -2.13 kcal/mol to the reference isomer 1. For CR-CCSD(T)/cc-pVTZ, it was isomer 1 that was observed to the most stable isomer. The

barrier height between diselenium trioxide 1 and 2, TS12, and between diselenium trioxide isomers 2 and 3, TS23 was shown to be 28.75 kcal/mol and 12.28 kcal/mol with the use of the cc-pVTZ basis. For diselenium pentaoxide (Se_2O_5) the most stable structure, predicted by CR-CCSD(T)/cc-pVDZ and cc-pVTZ methods is isomer 2 followed by isomer 3 and the least stable, was isomer 1. The barrier height predicted between isomers 1 and 2 was relatively small, i.e., 0.56 and 0.12 kcal/mol for the two basis sets, revealing the possibility of isomerization.

CHAPTER VII

AN ALGORITHM DESIGN FOR SPIN-COMPONENT SCALED SECOND-ORDER MØLLER-PLESSET PERTURBATION THEORY

Introduction

The computation of correlation energy of a system at the MP2 level of theory requires the evaluation of the four-centered electron repulsion integrals (ERIs), which is a time-consuming procedure in general quantum chemical calculations. But in recent times, with the advances in computer technology alongside the improvements in quantum chemical algorithms, the computational cost of this process has been reduced to the extent that calculations on systems that could only be addressed by DFT a few years ago could now be considered by MP2 calculations. Consequently, assessment of the adequacy of calculations that scale as MP2 is timely.

Spin–Component-Scaled Second–Order Møller–Plesset Perturbation (SCS-MP2) theory

The HF wavefunction is the best possible wavefunction that can be expressed as a Slater determinant, and usually gives 99% of the total energy of the system. However, the 1% error in this calculation cannot be neglected, since it is comparable in size to the strength of chemical bonds. This error comes from the description of the HF wavefunction of electron–electron repulsion in an average sense without including the actual electron correlation. Consequently, higher levels of theory that could possibly correct this limitation in the calculation of electronic energies of molecules are required. There are several powerful techniques presently that can accurately account for the

correlation energy of many particle system with errors < 1 kcal/mol [187]; i.e., methods like coupled-cluster, especially with the R12 extension. However, the limitation to most of these techniques is cost [188-190]. Second-order Møller-Plesset perturbation theory (MP2) [191] is the simplest and least expensive *ab initio* method for including electron correlation effects in electronic structure calculations. However, MP2 is less robust than high-accuracy methods when applied to complicated correlation problems occurring in compounds like biradicals, transition states or metal-containing compounds. In addition MP2 needs large basis sets to obtain accurate results [76]. Grimme showed recently that the accuracy of standard MP2 results improve remarkably by separately scaling the opposite spin (αβ) and same-spin (αα + ββ) components of the MP2 correlation energy [69]. This method is termed Spin–component–scaled second–order Møller–Plesset perturbation theory (SCS–MP2). In this method, the correlation energy contributions from antiparallel-spin (αβ, "singlet") pairs of electrons are scaled by $C_{OS} = \frac{6}{5}$, and that for parallel–spin (αα, ββ, "triplet") pairs of electrons are scaled by $C_{SS} = \frac{1}{5} \text{to} \frac{2}{5}$. The reason for the variation is that low–level methods for electron correlation, like MP2, show a systematic energy bias towards unpaired electrons while the contributions from spin–paired electrons are underestimated.

The exact one–particle basis set correlation energy E_{Corr} is

$$E_{Corr} = E^{Exact} - E^{HF} \quad . \tag{95}$$

At the MP2 level, the correlation energy can be separated into a sum over antiparallel and parallel spin components,

$$E_{Corr} = E^{(2)}_{SCS-MP2} = E^{(2)}_{OS} + E^{(2)}_{SS}\,, \tag{96}$$

where $E^{(2)}_{SS}$ and $E^{(2)}_{OS}$ are given by contributions from electron pairs with αα, ββ, and αβ spin as

$$E^{(2)}_{SS} = \frac{1}{2}\sum_{ij} e_{ij} + \frac{1}{2}\sum_{\bar{i}\bar{j}} e_{\bar{i}\bar{j}} \tag{97}$$

and

$$E^{(2)}_{OS} = \sum_{i\bar{j}} e_{i\bar{j}} \tag{98}$$

with the pair energies:

$$e_{ij} = \sum_{ab} (T^{ab}_{ij} - T^{ba}_{ij})(ia|jb)\,, \tag{99}$$

$$e_{\bar{i}\bar{j}} = \sum_{\bar{a}\bar{b}} (T^{\bar{a}\bar{b}}_{\bar{i}\bar{j}} - T^{\bar{b}\bar{a}}_{\bar{i}\bar{j}})(\bar{i}\bar{a}|\bar{j}\bar{b})\,, \tag{100}$$

$$e_{i\bar{j}} = \sum_{a\bar{b}} T^{a\bar{b}}_{i\bar{j}} (ia|\bar{j}\bar{b})\,, \tag{101}$$

where T are the doubles amplitudes. $(ia|jb)$ is a two–electron integral in Mulliken's notation, and ij and ab are occupied and virtual spin orbitals; β spin is designated by an over–line.

In the frame-work of MP2 theory, T, which defines the first order correction wave function, is

$$T_{ij}^{ab} = \frac{(ia|jb)}{\varepsilon_i + \varepsilon_j - \varepsilon_a - \varepsilon_b}, \tag{102}$$

where ε represents canonical HF orbital energies. Inserting equations 97 – 102, step wise, into the MP2 correlation energy equation as shown below gives the SCS–MP2 correlation energy expression. This simple modification increases the accuracy of MP2 dramatically.

The MP2 correlation energy is

$$E_0^{(2)} = \frac{1}{4}\sum_{ij}^{\substack{occ \\ sp.orb}}\sum_{ab}^{\substack{vir \\ sp.orb}} \frac{\left|\langle ij\|ab\rangle\right|^2}{\varepsilon_i + \varepsilon_j - \varepsilon_a - \varepsilon_b} \tag{103}$$

It can be rewritten from physicist's notation to chemist's notation as follows

$$\langle ij\|ab\rangle = \langle ij|ab\rangle - \langle ij|ba\rangle = [ia|jb] - [ib|ja] \tag{104}$$

The general definition of two electrons integral is as shown below,

$$\left[i_{\sigma_i} a_{\sigma_a} \middle| j_{\sigma_j} b_{\sigma_b}\right] = \iint \phi_i(1)\phi_a(1)\frac{1}{r_{12}}\phi_j(2)\phi_b(2)d^3r_1 d^3r_2 \times \sigma_i(1)\sigma_a(1)\sigma_j(2)\sigma_b(2) \tag{105}$$

$$= \delta_{\sigma_i\sigma_a}\delta_{\sigma_j\sigma_b}\int \phi_i(1)\phi_a(1)\frac{1}{r_{12}}\phi_j(2)\phi_b(2)d^3r_1 d^3r_2 \tag{106}$$

$$= \delta_{\sigma_i\sigma_a}\delta_{\sigma_j\sigma_b}(ia|jb) \tag{107}$$

Inserting the fluctuation potential matrix element into Eq. 103 obtains

$$E_0^{(2)} = \frac{1}{4}\sum_{ij}^{\substack{occ \\ sp.orb}}\sum_{ab}^{\substack{vir \\ sp.orb}} \frac{([ia|jb] - [ib|ja])^2}{\varepsilon_i + \varepsilon_j - \varepsilon_a - \varepsilon_b} \tag{108}$$

$(A - B)^2$ can be evaluated by the use of the expression below

$\sum_{A,B}(A-B)^2 = \sum_{A,B}[A(A-B)+B(B-A)] = 2\sum_{A,B}A(A-B)$, because "A" can be "B" and "B" can be "A". This is used to obtain equation 110.

Conversion of equation 109 from molecular spin orbitals to spatial molecular orbitals is shown below

$$\sum_{ijab}^{mso}\frac{\{[ia|jb]-[ib|ja]\}^2}{D_{ij}^{ab}} = \sum_{ijab}^{mo}\frac{[ia|jb]*\{[ia|jb]-[ib|ja]\}}{D_{ij}^{ab}} - \sum_{ijab}^{mo}\frac{[ib|ja]*\{[ia|jb]-[ib|ja]\}}{D_{ij}^{ab}} \quad (109)$$

$$= 2\sum_{ijab}^{mo}\frac{[ia|jb]*\{[ia|jb]-[ib|ja]\}}{D_{ij}^{ab}} \quad (110)$$

Expanding Eq. 103 gives

$$E_0^{(2)} = \frac{1}{4}\sum_{ij}^{occ\ sp.orb}\sum_{ab}^{vir\ sp.orb}\frac{[ia|jb]*([ia|bj]-[ib|ja])}{\varepsilon_i+\varepsilon_j-\varepsilon_a-\varepsilon_b} \quad (111)$$

Eq. 111 is converted from spin orbitals to molecular orbitals to obtain

$$E_0^{(2)} = \frac{1}{2}\sum_{ij}^{occ\ mo}\sum_{ab}^{vir\ mo}\frac{[ia|jb]*(4[ia|bj]-2[ib|ja])}{\varepsilon_i+\varepsilon_j-\varepsilon_a-\varepsilon_b} \quad (112)$$

Eq. 112 can be separated into its αα, ββ, and αβ components

$$E_0^{(2)} = \sum_{ij}^{occ\ mo}\sum_{ab}^{vir\ mo}\frac{2[ia|jb]*([ia|jb]-[ib|ja])}{\varepsilon_i+\varepsilon_j-\varepsilon_a-\varepsilon_b} + \frac{2[ia|jb]^2}{\varepsilon_i+\varepsilon_j-\varepsilon_a-\varepsilon_b} \quad (113)$$

Introducing scaling factors discussed above, results in

$$E^{(2)}_{SCS-MP2} = \sum_{ij}^{\substack{occ \\ mo}} \sum_{ab}^{\substack{vir \\ mo}} \frac{2[ia|jb]*\left((C_{Os} + C_{SS})[ia|jb] - (C_{SS})[ib|ja]\right)}{\varepsilon_i + \varepsilon_j - \varepsilon_a - \varepsilon_b} \tag{114}$$

$$E^{(2)}_{SCS-MP2} = \sum_{ij}^{\substack{occ \\ mo}} \sum_{ab}^{\substack{vir \\ mo}} \frac{2[ia|jb]*\left(\left(\frac{1}{3} + \frac{6}{5}\right)[ia|jb] - \left(\frac{1}{3}\right)[ib|ja]\right)}{\varepsilon_i + \varepsilon_j - \varepsilon_a - \varepsilon_b} \tag{115}$$

Therefore, the spin component scaled Moller-Plesset perturbation energy can be written

$$E_0^{SCS-MP2} = E^{HF} + E^{(2)}_{SCS-MP2} \tag{116}$$

This result improves the MP2 energy making it comparable to that of CCSD(T) but much less expensive [69].

Actual computation of the SCS-MP2 energy is mostly dominated by calculation of the two electron integrals over molecular orbitals. The MO exchange integrals (ia|jb) are computed from a transformation of the atomic orbitals (AO) or symmetry orbitals (SO) ERIs over restricted MO index ranges, in our case by the "mctrans" code in the UNDMOL package, i.e.,

$$[ia|jb] = (ia|jb) = \sum_{\mu,\nu,\lambda,\sigma} C_{\mu i} C_{\nu a} C_{\lambda j} C_{\sigma b} (\mu\nu \,|\, \lambda\sigma), \tag{117}$$

where, μ, ν, λ and σ denote SOs, and $\|C_{\mu i}\|$ is the MO coefficient matrix for the transformation from the SO to the MO basis.

The transformation process of Eq. (117) is performed in four steps:

$$(iv|\lambda\sigma) = \sum_{\mu} (\mu\nu \mid \lambda\sigma)\, C_{\mu i} \,, \tag{118}$$

$$(ia \mid \lambda\sigma) = \sum_{\nu} (i\nu \mid \lambda\sigma)\, C_{\nu a} \,, \tag{119}$$

$$(ia \mid j\sigma) = \sum_{\lambda} (ia \mid \lambda\sigma)\, C_{\lambda j} \,, \tag{120}$$

$$(ia \mid jb) = \sum_{\sigma} (ia \mid j\sigma)\, C_{\sigma b} \,. \tag{121}$$

where the cost of each step is ON^4, OVN^3, O^2VN^2, O^2V^2N, respectively, where N, O, V, represent the numbers of atomic basis functions, occupied orbitals, and virtual orbitals respectively. The cost of calculation of (ia|jb) is the sum of the quarter transformations and is seen to scale as the fifth power of the system size. The integrals formed are stored on disk. After reading the exchange and coulomb integrals from disk and the one electron molecular orbital integral contributions, the orbital energies ε_i are calculated (as in Eq. 30 in Chapter II).

The SCS-MP2 energy can then be calculated using the following scheme:

Loop i = 1, nocc

Loop j = 1, nocc

Loop a = 1, nvirt

Loop b = b, nvirt

$$t_{ab}^{ij} = (ia \mid jb)/(\varepsilon_i - \varepsilon_a + \varepsilon_j - \varepsilon_b)$$

$$E_{SCS-MP2} = E_{RHF} + (2 - \delta_{ij})\{(23/15) * (ia \mid jb) - (1/3)(ia \mid jb)\}t_{ab}^{ij}$$

End loop

End loop

End loop

End loop

Performance of the SCS-MP2 energy calculation

The MP2 and SCS-MP2 programs for correlation energies were programmed in a development version of the UNDMOL program. On MP2/6-31G* optimized geometries, energy calculations at the MP2 and SCS-MP2 level of theory using the Dunning cc-pVTZ basis [139] were carried out. These calculations were done with the implementation of the frozen core approximation (i.e., the molecular orbital corresponding to the C, N, O, F, 1s orbitals were kept doubly occupied).

The performance of the present SCS-MP2 code and MP2 is assessed relative to the higher correlation method QCISD(T). In this study, the test molecules are those described by Jung et al. [79], which also provides QCISD(T) results as well as results of an earlier implementation of SCS-MP2. Table 44 shows the percentage of total QCISD(T) correlation energy that is recovered by MP2 and SCS-MP2 by the use of the present code. The values from our implementation agree with those of Jung et al. [79]. The average recovery percentage for the molecules studied with the present SCS-MP2 code in this dissertation is (93.9 ± 1.8), that by Jung et al. [79] is (93.8 ± 1.8), and that from MP2 is (92.5 ± 5.8). The small difference from the results of the Jung et al. study is presumably due to differences in the integral evaluation and/or transformation. Table 44 reveals that SCS-MP2 (93.9 ± 1.8), performs better than MP2 (92.5 ± 5.8) not only in the average but notably in the standard deviation.

Table 44. Total correlation energy (CE) recovered by MP2, and SCS-MP2 relative to QCISD(T).

Molecule	QCISD(T) (mH)[a]	MP2 %CE	SCS-MP2 %CE
C_2H_4	-375.4	89.4	90.9
H_2O	-276.1	95.0	94.0
H_2O_2	-525.6	95.1	93.7
HCN	-371.8	94.2	92.9
HF	-281.3	96.9	94.9
H_2	-39.3	80.6	96.7
N_2	-398.5	96.1	93.9
Average %		92.5 ± 5.8 (92.5 ± 5.9)	93.9 ± 1.8 (93.8 ± 1.7)

[a]Ref. [79].
[a]The values in parenthesis are those from Jung et al. [79]

Open-shell-spin-component-scaled second-order Møller-Plesset perturbation theory (Open-shell SCS-MP2)

As noted in the preceding subsection, a highly efficient and size-extensive means of obtaining correlation energy for the electronic structures of many molecules is done by Møller-Plesset perturbation theory, also known as many-body perturbation theory (MBPT) [189]. In low order MBPT, accurate results can be obtained only when a reasonably good reference function is available to represent the problem. Existing spin-component-scaled MP2 is based on closed (restricted) HF, and is thus applicable to problems amenable to RHF. Unrestricted Hartree-Fock (UHF) has usually served as the reference for open-shell systems. This reference function has significant advantages in bond breaking situations. There are some disadvantages also, like the recurring existence

of several different UHF solutions, leading to ambiguities in the choice of an UHF solution. And most importantly, since UHF functions are not eigenfunctions of spin, they are often contaminated by states of higher spin multiplicity [189]. This harmful effect on correlation energy is observed in the low-order MBPT approximations, but is reduced in CCSD, CCSDT and its approximations CCSD(T), CCSDT-n, and CCSD+T(CCSD). Because MBPT(n) is unable to eliminate this spin contamination effect, in order to solve this problem, different UHF-based spin-projected MBPT methods have been developed; these remove just one (or a few) contaminants in UHF-MP2, but are not applicable easily in higher orders of MBPT. Moreover, the spin-projected MBPT methods will not usually be size extensive. In addition, they do not reliably determine relative energy differences between open- and closed-shell molecules at a given MBPT(n) level. In addition, evaluation of analytical gradients within such projected approaches, which are an essential part of any widely used method in quantum chemistry, is difficult. To eliminate spin contamination in open shell systems, calculations can be based on high-spin restricted open-shell Hartree-Fock (ROHF) solutions, which are spin eigenfunctions of the reference state. On this basis, Bartlett and co-workers developed the ROHF-CC method [189]. Hubac and Carsky [73, 192, 193] worked on ROHF-based-MBPT, but they redefined H_0 as a sum of diagonal Fock operators, changing the meaning of MBPT(n) from the usual canonical (Møller Plesset) Hartree-Fock case. The disadvantage is that certain invariant properties are lost. Wolinski and Pulay [194] presented another ROHF-MBPT method. This method retains the order-by-order, usual canonical orbital self-consistent field (SCF) theory, but brings in a non-diagonal resolvent operator, which requires an iterative solution. But this does not lead to high accuracy, except with the

inclusion of the triple contribution in MBPT(4) which will make it expensive and impractical, leading to the recommendation of a noniterative approach.

The ROHF-MBPT method presented by Bartlett and co-workers [72] is noniterative and can easily be applied to any order of perturbation theory. This method is not a fully spin adapted approach. The advantages are that it facilitates readily treating any order, subject to the projected spin eigenfunction property $\langle \Psi_{ROHF} | \hat{S}^2 | \Psi_{MBPT} \rangle = S(S+1)$, although $\langle \Psi_{MBPT} | \hat{S}^2 | \Psi_{MBPT} \rangle \neq S(S+1)$, and retains the invariance properties of MBPT/CC theory to transformations among just occupied or unoccupied orbitals. It also allows the development of analytical gradients.

This present work is based on the use of the ROHF-MBPT method of Bartlett and co-workers [195-198] to develop a method and computer program for spin-component scaling in open-shell systems. We refer to it as open-shell-spin-component-scaled second-order Møller-Plesset perturbation theory (open-shell SCS-MP2).

In the following equations, *i, j, k,* …… represent occupied orbitals; *a, b, c,* … represent unoccupied orbitals; and *p, q, r,* ….. are generic indices representing either kind of orbital.

The general expression for MBPT(n) energy is

$$E^{(n)} = \sum_{ia} t_i^{a(n-1)} f_{ai} + \frac{1}{4} \sum_{ijab} \tau_{ia}^{b(n-1)} \langle ij \| ab \rangle \qquad (122)$$

That for MBPT(2) is

$$E_0^{(2)} = \sum_{i}^{occ} \sum_{a}^{unocc} t_i^{a(1)} f_{ai} + \frac{1}{4} \sum_{ijab}^{occ,unocc} \tau_{ij}^{ab(1)} \left\{ [ia|jb] - [ib|ja] \right\} \quad (123)$$

Since the MBPT(n) energy is invariant to rotations that mix occupied or virtual orbitals among themselves, unitary transformations can be used to rotate the ROHF eigenvectors. This will bring the occupied-occupied and virtual-virtual blocks of the Fock matrices to diagonal form resulting in the formation of semicanonical orbitals. This also results in unequal α and β orbitals, but the eigenfunction property of the reference function is not affected.

Using semicanonical orbitals, the first-order T amplitudes can be expressed as follows:

First-order amplitudes

$$t_i^{a(1)} = \frac{f_{ia}}{D_i^a} \quad (124)$$

$$\tau_{ij}^{ab(1)} = t_{ij}^{ab(1)} = \frac{\langle ij \| ab \rangle}{D_{ij}^{ab}} \quad (125)$$

$$D_i^a = f_{ii} - f_{aa} \quad (126)$$

$$D_{ij}^{ab} = f_{ii} + f_{jj} - f_{aa} - f_{bb} \quad (127)$$

Substituting Equation 124, 125, 126 and 127 into Equation 123 will obtain Equation 128, which is the MP2 general expression

$$E_0^{(2)} = \sum \frac{|f_{ia}|^2}{D_i^a} + \frac{1}{4}\sum_{ijab} \frac{|\langle ij\|ab\rangle|^2}{D_{ij}^{ab}} \tag{128}$$

As before, a matrix element of the fluctuation potential is

$$\langle ij\|ab\rangle = \langle ij|ab\rangle - \langle ij|ba\rangle, \text{ in physicists notation} \tag{129}$$

Conversion from physicist's notation to chemist's notation

$$\langle ij\|ab\rangle = [ia|jb] - [ib|ja] \tag{130}$$

gives

$$E_0^{(2)} = \sum_{ia} \frac{|f_{ia}|^2}{D_i^a} + \frac{1}{4}\sum_{ijab} \frac{([ia|jb] - [ib|ja])^2}{D_{ij}^{ab}} \tag{131}$$

The operator, $f_{pq} = \langle p|h|q\rangle + \sum_{j=1}^{occ} \langle pj\|qj\rangle$, will be examined in greater detail.

For any xy orbital pair

$$f_{xy} = h_{xy} + \sum_{j}^{\substack{occ \\ mso}} \{ [xy|jj] - [xj|yj] \}$$

$$= h_{\tilde{x}\tilde{y}} \delta_{\sigma_x \sigma_y} + \sum_{j}^{occ} \sum_{\sigma_j=1}^{n_j} \left\{ \left(\tilde{x}\tilde{y} \middle| \tilde{j}\,\tilde{j} \right) \delta_{\sigma_x \sigma_y} - \left(\tilde{x}\tilde{j} \middle| \tilde{y}\tilde{j} \right) \delta_{\sigma_x \sigma_y} \delta_{\sigma_x \sigma_j} \right\}$$

$$\text{note}: \sigma_j = 1 \Rightarrow \sigma_j = \alpha$$

$$\sigma_j = 2 \Rightarrow \sigma_j = \beta \qquad (132)$$

$$n_j = 2 \quad \text{for} \quad \text{closed} \quad \text{shell}$$

$$n_j = 1 \quad \text{for} \quad \text{open} \quad \text{shell}$$

$$= \delta_{\sigma_x \sigma_y} \left\{ h_{\tilde{x}\tilde{y}} \delta_{\sigma_x \sigma_y} + \sum_{\tilde{j}}^{occ} \sum_{\sigma_j=1}^{n_j} \left[\left(\tilde{x}\tilde{y} \middle| \tilde{j}\,\tilde{j} \right) - \delta_{\sigma_x \sigma_j} \left(\tilde{x}\tilde{j} \middle| \tilde{y}\tilde{j} \right) \right] \right\}$$

$$= \delta_{\sigma_x \sigma_y} \left\{ f^{\alpha}_{\tilde{x}\tilde{y}} \delta_{\sigma_x \alpha} + f^{\beta}_{\tilde{x}\tilde{y}} \delta_{\sigma_y \beta} \right\}$$

$$f^{\alpha}_{\tilde{x}\tilde{y}} = h_{\tilde{x}\tilde{y}} + \sum_{\tilde{j}}^{occ} \left[n_j \left(\tilde{x}\tilde{y} \middle| \tilde{j}\,\tilde{j} \right) - \left(\tilde{x}\tilde{j} \middle| \tilde{y}\tilde{j} \right) \right] \qquad (133)$$

$$f^{\beta}_{\tilde{x}\tilde{y}} = h_{\tilde{x}\tilde{y}} + \sum_{\tilde{j}}^{occ} \left[n_j \left(\tilde{x}\tilde{y} \middle| \tilde{j}\,\tilde{j} \right) - (n_j - 1) \left(\tilde{x}\tilde{j} \middle| \tilde{y}\tilde{j} \right) \right], \ \delta_{nj} = 2 \qquad (134)$$

From equation 132 f_{ii} can be calculated as follows

$$f_{ii} = h_{ii} + \sum_{j}^{mso} \{ [ii|jj] - [ij|ij] \} \qquad (135)$$

Conversion from molecular spin orbitals to spatial molecular orbitals is as shown below

$$f_{\tilde{i}\,\tilde{i}} = h_{\tilde{i}\,\tilde{i}} \langle \sigma_i | \sigma_i \rangle + \sum_{\tilde{j}}^{occ} \sum_{\sigma_i = \alpha, \beta} \left[\left(\tilde{i}\,\tilde{i} \middle| \tilde{j}\,\tilde{j} \right) \langle \sigma_i | \sigma_i \rangle \langle \sigma_j | \sigma_j \rangle - \left(\tilde{i}\,\tilde{j} \middle| \tilde{i}\,\tilde{j} \right) \langle \sigma_i | \sigma_i \rangle^2 \right]$$

$$\langle \sigma_i | \sigma_i \rangle = \langle \sigma_j | \sigma_j \rangle = 1 \qquad (136)$$

$$\langle \sigma_i | \sigma_j \rangle^2 = \delta^2_{\sigma_i \sigma_j} = \delta_{\sigma_i \sigma_j}$$

$$f_{\tilde{i}\tilde{i}}^{\tilde{i}\tilde{i}} = h_{\tilde{i}\tilde{i}}^{\tilde{i}\tilde{i}} + \sum_{\tilde{j}}^{occ} \sum_{\sigma_i=\alpha,\beta} \left[\left(\tilde{i}\,\tilde{i} \middle| \tilde{j}\,\tilde{j} \right) - \delta_{\sigma_i\sigma_j} \left(\tilde{i}\,\tilde{j} \middle| \tilde{i}\,\tilde{j} \right) \right] \tag{137}$$

$$f_{\tilde{i}\tilde{i}}^{\sigma_i} = h_{\tilde{i}\tilde{i}}^{\sigma_i} + \sum_{\tilde{j}}^{occ} \sum_{\sigma_i=\alpha,\beta} \left[\left(\tilde{i}\,\tilde{i} \middle| \tilde{j}\,\tilde{j} \right) - \delta_{\sigma_i\sigma_j} \left(\tilde{i}\,\tilde{j} \middle| \tilde{i}\,\tilde{j} \right) \right] \tag{138}$$

$$f_{\tilde{i}\tilde{i}}^{\alpha} = h_{\tilde{i}\tilde{i}}^{\alpha} + \sum_{\tilde{j}}^{occ} \left[n_j \left(\tilde{i}\,\tilde{i} \middle| \tilde{j}\,\tilde{j} \right) - \left(\tilde{i}\,\tilde{j} \middle| \tilde{i}\,\tilde{j} \right) \right] \tag{139}$$

n_i = 1 or 2

if n_j =2 => closed shell

if n_j =1 => open shell

$$f_{\tilde{i}\tilde{i}}^{\beta} = h_{\tilde{i}\tilde{i}}^{\beta} + \sum_{\tilde{j}}^{occ} \left[n_j \left(\tilde{i}\,\tilde{i} \middle| \tilde{j}\,\tilde{j} \right) - (n_j - 1) \left(\tilde{i}\,\tilde{j} \middle| \tilde{i}\,\tilde{j} \right) \right] \tag{140}$$

Note that, unlike usual MP2, f_{ia} has nonzero entries. This result from transformations which change the wave function and, because of these nonzero entries, it is considered as a 1st order term. f_{ia} can be obtained from equation 133 as shown below

$$f_{ia} = \left\langle i \middle| h \middle| a \right\rangle + \sum_{j}^{\substack{occ \\ mso}} \left\langle ij \middle\| aj \right\rangle \tag{141}$$

$$f_{ia} = h_{ia} + \sum_{j}^{\substack{occ \\ mso}} \left\langle ij \middle| aj \right\rangle - \left\langle ij \middle| ja \right\rangle \tag{142}$$

$$f_{ia} = h_{ia} + \sum_{j}^{\substack{occ \\ mso}} \left([ia|jj] - [ij|aj] \right) \tag{143}$$

$$\sum_{ia} \frac{\left|f_{ia}\right|^2}{D_i^a} = \sum_{i}^{\substack{occ\\mso}} \sum_{a}^{\substack{vir\\mso}} \frac{\left|f_{ia}\right|^2}{f_{ii} - f_{aa}} \tag{144}$$

$$= \sum_{\tilde{i}}^{\substack{occ\\mo}} \sum_{\sigma_i=1}^{n_i} \sum_{\tilde{a}}^{\substack{vir\\mo}} \sum_{\sigma_a=1}^{2} \frac{\left|f_{a\ i}^{\sigma_i}\right|^2 \delta_{\sigma_i\sigma_a}}{f_{ii}^{\sigma_i} - f_{aa}^{\sigma_a}} \tag{145}$$

$$= \sum_{\tilde{i}}^{\substack{occ\\mo}} \sum_{\tilde{a}}^{\substack{vir\\mo}} \left[\frac{\left|f_{ia}^{\alpha}\right|^2}{f_{ii}^{\alpha} - f_{aa}^{\alpha}} + (n_i - 1) * \frac{\left|f_{ia}^{\beta}\right|^2}{f_{ii}^{\beta} - f_{aa}^{\beta}} \right] \tag{146}$$

$$\frac{1}{4} * 2 \sum_{ij}^{occ} \sum_{ab}^{unocc} \frac{[ia|jb] * \{[ia|jb] - [ib|ja]\}}{f_{\tilde{i}\tilde{i}} + f_{\tilde{j}\tilde{j}} - f_{\tilde{a}\tilde{a}} - f_{\tilde{b}\tilde{b}}} =$$

$$= \frac{1}{2} * \sum_{\tilde{i}\tilde{j}}^{occ} \sum_{\tilde{a}\tilde{b}}^{unocc} \sum_{\sigma_i=1}^{ni} \sum_{\sigma_j=1}^{nj} \sum_{\sigma_a=1}^{2} \sum_{\sigma_b=1}^{2} \frac{\left(\tilde{i}\tilde{a}\middle|\tilde{j}\tilde{b}\right)\delta_{\sigma_i\sigma_a}\delta_{\sigma_j\sigma_b} * \left\{\left(\tilde{i}\tilde{a}\middle|\tilde{j}\tilde{b}\right)\delta_{\sigma_i\sigma_a}\delta_{\sigma_j\sigma_b} - \left(\tilde{i}\tilde{b}\middle|\tilde{j}\tilde{a}\right)\delta_{\sigma_i\sigma_b}\delta_{\sigma_j\sigma_a}\right\}}{f_{\tilde{i}\tilde{i}}^{\sigma_i} + f_{\tilde{j}\tilde{j}}^{\sigma_j} - f_{\tilde{a}\tilde{a}}^{\sigma_a} - f_{\tilde{b}\tilde{b}}^{\sigma_b}} \tag{147}$$

$$= \frac{1}{2} * \sum_{\tilde{i}\tilde{j}}^{occ} \sum_{\tilde{a}\tilde{b}}^{unocc} \sum_{\sigma_i=1}^{ni} \sum_{\sigma_j=1}^{nj} \frac{\left(\tilde{i}\tilde{a}\middle|\tilde{j}\tilde{b}\right) * \left\{\left(\tilde{i}\tilde{a}\middle|\tilde{j}\tilde{b}\right) - \delta_{\sigma_i}\delta_{\sigma_j}\left(\tilde{i}\tilde{b}\middle|\tilde{j}\tilde{a}\right)\right\}}{f_{\tilde{i}\tilde{i}}^{\sigma_i} + f_{\tilde{j}\tilde{j}}^{\sigma_j} - f_{\tilde{a}\tilde{a}}^{\sigma_i} - f_{\tilde{b}\tilde{b}}^{\sigma_j}} \tag{148}$$

Equation 149 is obtained by substituting σ_j in expression 148,

$$= \frac{1}{2} \sum_{\tilde{i}\tilde{j}}^{occ} \sum_{\tilde{a}\tilde{b}}^{unocc} \sum_{\sigma_i=1}^{ni} \left[\frac{\left(\tilde{i}\tilde{a}\middle|\tilde{j}\tilde{b}\right) * \left\{\left(\tilde{i}\tilde{a}\middle|\tilde{j}\tilde{b}\right) - \delta_{\sigma_i\alpha}\left(\tilde{i}\tilde{b}\middle|\tilde{j}\tilde{a}\right)\right\}}{f_{\tilde{i}\tilde{i}}^{\sigma_i} + f_{\tilde{j}\tilde{j}}^{\alpha} - f_{\tilde{a}\tilde{a}}^{\sigma_a} - f_{\tilde{b}\tilde{b}}^{\alpha}} + (n_j - 1) * \frac{\left(\tilde{i}\tilde{a}\middle|\tilde{j}\tilde{b}\right) * \left\{\left(\tilde{i}\tilde{a}\middle|\tilde{j}\tilde{b}\right) - \delta_{\sigma_i\beta}\left(\tilde{i}\tilde{b}\middle|\tilde{j}\tilde{a}\right)\right\}}{f_{\tilde{i}\tilde{i}}^{\sigma_i} + f_{\tilde{j}\tilde{j}}^{\beta} - f_{\tilde{a}\tilde{a}}^{\sigma_a} - f_{\tilde{b}\tilde{b}}^{\beta}} \right] \tag{149}$$

To obtain equation 150 the number of electrons for n_i is inserted, for a high spin case when n_i is singly occupied, σ_i has only an α spin

$$= \frac{1}{2}\sum_{\tilde{i}\tilde{j}}^{occ}\sum_{\tilde{a}\tilde{b}}^{unocc}\left[\begin{array}{l}\dfrac{\left(\tilde{i}\tilde{a}\middle|\tilde{j}\tilde{b}\right)*\left\{\left(\tilde{i}\tilde{a}\middle|\tilde{j}\tilde{b}\right)-\left(\tilde{i}\tilde{b}\middle|\tilde{j}\tilde{a}\right)\right\}}{f^{\alpha}_{\tilde{i}\tilde{i}}+f^{\alpha}_{\tilde{j}\tilde{j}}-f^{\alpha}_{\tilde{a}\tilde{a}}-f^{\alpha}_{\tilde{b}\tilde{b}}}+(n_i-1)*\dfrac{\left(\tilde{i}\tilde{a}\middle|\tilde{j}\tilde{b}\right)^2}{f^{\beta}_{\tilde{i}\tilde{i}}+f^{\alpha}_{\tilde{j}\tilde{j}}-f^{\beta}_{\tilde{a}\tilde{a}}-f^{\alpha}_{\tilde{b}\tilde{b}}} \\ +(n_j-1)*\dfrac{\left(\tilde{i}\tilde{a}\middle|\tilde{j}\tilde{b}\right)^2}{f^{\alpha}_{\tilde{i}\tilde{i}}+f^{\beta}_{\tilde{j}\tilde{j}}-f^{\alpha}_{\tilde{a}\tilde{a}}-f^{\beta}_{\tilde{b}\tilde{b}}}+(n_i-1)(n_j-1)*\dfrac{\left(\tilde{i}\tilde{a}\middle|\tilde{j}\tilde{b}\right)*\left\{\left(\tilde{i}\tilde{a}\middle|\tilde{j}\tilde{b}\right)-\left(\tilde{i}\tilde{b}\middle|\tilde{j}\tilde{a}\right)\right\}}{f^{\beta}_{\tilde{i}\tilde{i}}+f^{\beta}_{\tilde{j}\tilde{j}}-f^{\beta}_{\tilde{a}\tilde{a}}-f^{\beta}_{\tilde{b}\tilde{b}}}\end{array}\right]$$

Note: $f^{\alpha}_{\tilde{i}\tilde{i}}+f^{\beta}_{\tilde{j}\tilde{j}}\neq f^{\beta}_{\tilde{i}\tilde{i}}+f^{\alpha}_{\tilde{j}\tilde{j}}$ (150)

and $D^{\sigma\sigma'}_{\tilde{i}\tilde{j}\tilde{a}\tilde{b}}=f^{\sigma}_{\tilde{i}\tilde{i}}+f^{\sigma'}_{\tilde{j}\tilde{j}}-f^{\sigma}_{\tilde{a}\tilde{a}}-f^{\sigma'}_{\tilde{b}\tilde{b}}$

We conjecture that as was the case for closed shell MP2, the triplet and the singlet contributions are scaled differently to the obtain $E_{(OS\text{-}SCS\text{-}MP2)}{}^{(2)}$ energy. Since the correlation for electron pairs are not expected to be strongly affected by the total spin of the system, the scaling factors are those proposed by Grimme which are C_{SS} = 1/3 and C_{OS} = 6/5.

This equation is then substituted in to the original OS-SCS-MP2 equation

$$E^{(2)}_{OS-MP2}=\sum_{ia}\frac{|f_{ia}|^2}{D^a_i}+\frac{1}{4}\sum_{ijab}\frac{\left([ia|jb]-[ib|ja]\right)^2}{D^{ab}_{ij}} \quad (151)$$

$$E^{(2)}_{(OS-SCS-MP2)}=\sum\frac{|f_{ia}|^2}{D^a_i}+$$

$$\frac{1}{2}\sum_{\tilde{i}\tilde{j}}^{occ}\sum_{\tilde{a}\tilde{b}}^{unocc}\left[\begin{array}{l}\dfrac{1}{3}\dfrac{\left(\tilde{i}\tilde{a}\middle|\tilde{j}\tilde{b}\right)*\left\{\left(\tilde{i}\tilde{a}\middle|\tilde{j}\tilde{b}\right)-\left(\tilde{i}\tilde{b}\middle|\tilde{j}\tilde{a}\right)\right\}}{f^{\alpha}_{\tilde{i}\tilde{i}}+f^{\alpha}_{\tilde{j}\tilde{j}}-f^{\alpha}_{\tilde{a}\tilde{a}}-f^{\alpha}_{\tilde{b}\tilde{b}}}+(n_i-1)*\dfrac{6}{5}*\dfrac{\left(\tilde{i}\tilde{a}\middle|\tilde{j}\tilde{b}\right)^2}{f^{\beta}_{\tilde{i}\tilde{i}}+f^{\alpha}_{\tilde{j}\tilde{j}}-f^{\beta}_{\tilde{a}\tilde{a}}-f^{\alpha}_{\tilde{b}\tilde{b}}} \\ +(n_j-1)*\dfrac{6}{5}*\dfrac{\left(\tilde{i}\tilde{a}\middle|\tilde{j}\tilde{b}\right)^2}{f^{\alpha}_{\tilde{i}\tilde{i}}+f^{\beta}_{\tilde{j}\tilde{j}}-f^{\alpha}_{\tilde{a}\tilde{a}}-f^{\beta}_{\tilde{b}\tilde{b}}}+(n_i-1)(n_j-1)*\dfrac{1}{3}*\dfrac{\left(\tilde{i}\tilde{a}\middle|\tilde{j}\tilde{b}\right)*\left\{\left(\tilde{i}\tilde{a}\middle|\tilde{j}\tilde{b}\right)-\left(\tilde{i}\tilde{b}\middle|\tilde{j}\tilde{a}\right)\right\}}{f^{\beta}_{\tilde{i}\tilde{i}}+f^{\beta}_{\tilde{j}\tilde{j}}-f^{\beta}_{\tilde{a}\tilde{a}}-f^{\beta}_{\tilde{b}\tilde{b}}}\end{array}\right]$$

(152)

Evaluation of the quantities follows the algorithm for closed-shell SCS-MP2, although there are more terms in the open-shell case. A practical concern is the development of an efficient unrestricted transformation program, which currently does not exist in UNDMOL. Full development of the method will require optimization of the weighing parameters (i.e., C_{SS} and C_{OS}), because, although they can be expected to be close to Grimme's values for closed shells, small changes are to be expected.

References

1. Khait, Y. G.; Song, J.; Hoffmann, M. R. *J. Chem. Phys.* **2002**, *117*, 4133–4145.

2. Pandey, R. R.; Khait, Y. G.; Hoffmann, M. R. *J. Phys. Chem. A* **2004**, *108*, 3119–3124.

3. Song, J.; Khait, Y. G.; Hoffmann, M. R. *J. Phys. Chem. A* **2001**, *105*, 779–790.

4. Pople, J. A.; Head–Gordon, M.; Raghavachari, K. *J. Chem. Phys.* **1987**, *87*, 5968–75.

5. Hoffmann, M. R. *J. Phys. Chem.* **1996**, *100*, 6125–30.

6. Miehlich, B.; Savin, A.; Stoll, H.; Preuss, H. *Chem. Phys. Lett.* **1989**, *157*, 200–6.

7. Becke, A. D. *J. Chem. Phys.* **1993**, *98*, 5648–52.

8. Hoffmann, M. R.; David Sherrill, C.; Leininger, M. L.; Schaefer, H. F., III. *Chem. Phys. Lett.* **2002**, 355, 183–192.

9. Boldyrev, A. I.; Schleyer, P. v. R.; Higgins, D.; Thomson, C.; Kramarenko, S. S. *J. Comput. Chem.* **1992**, *13*, 1066–78.

10. Hashimoto, M.; Hatanaka, Y. *Eur. J. Org. Chem.* **2008,** 2513–2523.

11. Bogdanova, A.; Popik, V. V. *J. Am. Chem. Soc.* **2003**, *125*, 14153–14162.

12. Arenas, J. F.; Lopez–Tocon, I.; Otero, J. C.; Soto, J. *J. Am. Chem. Soc.* **2002**, *124*, 1728–1735.

13. Mitsch, R. A. *J. Heterocycl. Chem.* **1964**, *1*, 59–60.

14. Mitsch, R. A. *J. Am. Chem. Soc.* **1965**, *87*, 758–61.

15. Han, M. S.; Cho, H.–G.; Cheong, B.–S. *Bull. Korean Chem. Soc.* **1999**, *20*, 1281–1287.

16. Clifford, E. P.; Wenthold, P. G.; Lineberger, W. C.; Ellison, G. B.; Wang, C. X.; Grabowski, J. J.; Vila, F.; Jordan, K. D. *J. Chem. Soc., Perkin Trans. 2 Physical Organic Chemistry* **1998**, 1015–1022.

17. Slipchenko, L. V.; Krylov, A. I. *J. Chem. Phys.* **2002**, *117*, 4694–4708.

18. Scheschkewitz, D.; Amii, H.; Gornitzka, H.; Schoeller, W. W.; Bourissou, D.; Bertrand, G. *Science (Washington, DC, U. S.)* **2002**, *295*, 1880–1881.

19. Feller, D.; Davidson, E. R.; Borden, W. T. *J. Am. Chem. Soc.* **1982**, *104*, 1216–18.

20. Pittner, J.; Nachtigall, P.; Carsky, P.; Hubac, I. *J. Phys. Chem. A* **2001**, *105*, 1354–1356.

21. Turro, N. J., *Modern Molecular Photochemistry*. ed.; **1978**; 'Vol.' p 628 pp.

22. Borden, W. T.; Davidson, E. R.; Feller, D. *Tetrahedron* **1982**, *38*, 737–9.

23. Jones, G., II. *J. Chem. Educ.* **1974**, *51*, 175–81.

24. Roos, B. O.; Taylor, P. R.; Siegbahn, E. M. *Chem. Phys.* **1980**, *48*, 157–73.

25. Ruedenberg, K.; Schmidt, M. W.; Gilbert, M. M.; Elbert, S. T. *Chem. Phys.* **1982**, *71*, 41–9.

26. Matsuda, K.; Iwamura, H. *J. Am. Chem. Soc.* **1997**, *119*, 7412–7413.

27. Dowd, P. *J. Amer. Chem. Soc.* **1970**, *92*, 1066–8.

28. Dowd, P.; Chang, W.; Paik, Y. H. *J. Am. Chem. Soc.* **1986**, *108*, 7416–17.

29. Borden, W. T. *J. Am. Chem. Soc.* **1975**, *97*, 5968–70.

30. Borden, W. T.; Davidson, E. R. *J. Am. Chem. Soc.* **1977**, *99*, 4587–94.

31. Ovchinnikov, A. A. *Theor. Chim. Acta* **1978**, *47*, 297–304.

32. Nachtigall, P.; Dowd, P.; Jordan, K. D. *J. Am. Chem. Soc.* **1992**, *114*, 4747–52.

33. Nachtigall, P.; Jordan, K. D. *J. Am. Chem. Soc.* **1993**, *115*, 270–1.

34. Filatov, M.; Shaik, S. *J. Phys. Chem. A* **1999**, *103*, 8885–8889.

35. Lai, M. S.; Hsueh, Y. M.; Chen, C. J.; Shyu, M. P.; Chen, S. Y.; Kuo, T. L.; Wu, M. M.; Tai, T. Y. *Am J Epidemiol* **1994**, *139*, 484–92.

36. Chen, C.–J.; Hsueh, Y.–M.; Lai, M.–S.; Shyu, M.–P.; Chen, S.–Y.; Wu, M.–M.; Kuo, T.–L.; Tai, T.–Y. *Hypertension (Dallas)* **1995**, *25*, 53–60.

37. Chen, C. J.; Wu, M. M.; Lee, S. S.; Wang, J. D.; Cheng, S. H.; Wu, H. Y. *Arteriosclerosis (Dallas, Tex.)* **1988**, *8*, 452–60.

38. Chen, C. J.; Chen, C. W.; Wu, M. M.; Kuo, T. L. *Br J Cancer* **1992**, *66*, 888–92.

39. Chen, C. J.; Wang, C. J. *Cancer Res.* **1990**, *50*, 5470–4.

40. Sonich–Mullin, C.; Fielder, R.; Wiltse, J.; Baetcke, K.; Dempsey, J.; Fenner–Crisp, P.; Grant, D.; Hartley, M.; Knaap, A.; Kroese, D.; Mangelsdorf, I.; Meek, E.; Rice, J. M.; Younes, M. *Regul. Toxicol. Pharmacol.* **2001**, *34*, 146–152.

41. Shah, P.; Strezov, V.; Stevanov, C.; Nelson, P. F. *Energy Fuels* **2007**, *21*, 506–512.

42. http://pulse.pharmacy.arizona.edu/resources/powerful explorations/mercury arsenic coal.pdf

43. http://www.dtsc.ca.gov/InformationResources/Arsenic_Relative_Study.cfm.

44. Huggins, F. E.; Senior, C. L.; Chu, P.; Ladwig, K.; Huffman, G. P. *Environ. Sci. Technol.* **2007**, *41*, 3284–3289.

45. Cullen, W. R.; Reimer, K. J. *Chem. Rev.* **1989**, *89*, 713–64.

46. Allan H. Smith; Elena O. Lingas; Rahman, M. *Bulletin of the World Health Organization* **2000**, *78*, 1092–1103.

47. http://www.greenfacts.org/en/arsenic/l–3/arsenic–2.htm#3p0. **2004**.

48. Walker, S. R.; Jamieson, H. E.; Lanzirotti, A.; Andrade, C. F.; Hall, G. E. M. *Can. Mineral.* **2005**, *43*, 1205–1224.

49. Monahan–Pendergast, M.; Przybylek, M.; Lindblad, M.; Wilcox, J. *Atmos. Environ.* **2008**, *42*, 23492–357.

50. Piecuch, P.; Kucharski, S. A.; Kowalski, K.; Musial, M. *Comput. Phys. Commun.* **2002**, *149*, 71–96.

51. Kowalski, K.; Piecuch, P. *J. Chem. Phys.* **2000**, *113*, 5644–5652.

52. Kowalski, K.; Piecuch, P. *J. Chem. Phys.* **2000**, *113*, 18–35.

53. Piecuch, P.; Wloch, M. *J. Chem. Phys.* **2005**, *123*, 224105/1–224105/10.

54. Fitzpatrick, S.; Ebdon, L.; Foulkes, M. E. *Int. J. Environ. Anal. Chem.* **2002**, *82*, 835–841.

55. Swaine, D. J. *Fuel Process. Technol.* **2000**, *65–66*, 21–33.

56. Zheng, B.; Hong, Y.; Zhao, W.; Zhou, H.; Xia, W.; Su, H.; Mao, D.; Yang, L.; Thornton, I. *Chin. Sci. Bull.* **1992**, *37*, 1725–9.

57. Finkelman, R. B. *Fuel Process. Technol.* **1994**, *39*, 21–34.

58. Clark, L. C.; Combs, G. F., Jr.; Turnbull, B. W.; Slate, E. H.; Chalker, D. K.; Chow, J.; Davis, L. S.; Glover, R. A.; Graham, G. F.; Gross, E. G.; Krongrad, A.; Lesher, J. L., Jr.; Park, H. K.; Sanders, B. B., Jr.; Smith, C. L.; Taylor, J. R. *JAMA, J. Am. Med. Assoc.* **1996**, *276*, 1957–1963.

59. Trumble, J. T.; Kund, G. S.; White, K. K. *Environ. Pollut.* **1998**, *101*, 175–182.

60. Zhang, J.; Zhao, Y.; Ding, F.; Zeng, H.; Zheng, C. *Front. Energy Power Eng. China* **2007**, *1*, 273–279.

61. Andren, A. W.; Klein, D. H.; Talmi, Y. *Environ. Sci. Technol.* **1975**, *9*, 856–8.

62. Yan, R.; Gauthier, D.; Flamant, G.; Peraudeau, G.; Lu, J.; Zheng, C. *Environ. Sci. Technol.* **2001**, *35*, 1406–1410.

63. Brassington, N. J.; Edwards, H. G. M.; Long, D. A.; Skinner, M. *J. Raman Spectrosc.* **1978**, *7*, 158–60.

64. Takeo, H.; Hirota, E.; Morino, Y. *J. Mol. Spectrosc.* **1970**, *34*, 370–82.

65. Urban, D. R.; Wilcox, J. *J. Phys. Chem. A* **2006**, *110*, 5847–5852.

66. Born, M.; Oppenheimer, R. *Ann. Phys. (Leipzig)* **1927**, *84*, 457.

67. Moller, C.; Plesset, M. S. *Phys. Rev.* **1934**, *46*, 618–22.

68. Nielsen, I. M. B. *Chem. Phys. Lett.* **1996**, *255*, 210–216.

69. Grimme, S. *J. Chem. Phys.* **2003**, *118*, 9095–9102.

70. Pulay, P.; Saebo, S.; Wolinski, K. *Chem. Phys. Lett.* **2001**, *344*, 543–552.

71. Hose, G. *J. Chem. Phys.* **1986**, *84*, 4505–18.

72. Purvis, G. D., III; Bartlett, R. J. *J. Chem. Phys.* **1982**, *76*, 1910–18.

73. Cizek, J. *J. Chem. Phys.* **1966**, *45*, 4256–66.

74. Curtiss, L. A.; Raghavachari, K.; Pople, J. A. *J. Chem. Phys.* **1993**, *98*, 1293–8.

75. Grimme, S. *J. Comput. Chem.* **2003**, *24*, 1529–1537.

76. Hubac, I.; Carsky, P. *Phys. Rev. A* **1980**, *22*, 2392–9.

77. Carsky, P.; Zahradnik, R.; Hubac, I.; Urban, M.; Kello, V. *Theor. Chim. Acta* **1980**, *56*, 315–28.

78. DiStasio, R. A., Jr.; Jung, Y.; Head–Gordon, M. *J. Chem. Theory Comput.* **2005**, *1*, 862–876.

79. Jung, Y.; Lochan, R. C.; Dutoi, A. D.; Head–Gordon, M. *J. Chem. Phys.* **2004**, *121*, 9793–9802.

80. Grimme, S. *J. Phys. Chem. A* **2005**, *109*, 3067–3077.

81. Gwaltney, S. R.; Bartlett, R. J. *J. Chem. Phys.* **1999**, *110*, 62–71.

82. Pople, J. A.; Krishnan, R.; Schlegel, H. B.; Binkley, J. S. *Int. J. Quantum Chem.* **1978**, *14*, 545–60.

83. Takatani, T.; David Sherrill, C. *Phys Chem Chem Phys: PCCP* **2007**, *9*, 6106–14.

84. Moller–Christensen, E. *Lancet:Lancet* **1934**, *II*, 1388–9.

85. Watts, J. D.; Gauss, J.; Bartlett, R. J. *J. Chem. Phys.* **1993**, *98*, 8718–33.

86. Scuseria, G. E.; Schaefer, H. F., III. *J. Chem. Phys.* **1989**, *90*, 3700–3.

87. Cramer, C. J., *Essentials of Computational Chemistry*. ed.; John Wiley & Sons: **2002**; 'Vol.' p.

88. Ruedenberg, K.; Sundberg, K. R. *Quantum Sci.* **1976**, 505–15.

89. Cheung, L. M.; Sundberg, K. R.; Ruedenberg, K. *J. Am. Chem. Soc.* **1978**, *100*, 8024.

90. Cheung, L. M.; Sundberg, K. R.; Ruedenberg, K. *Int. J. Quantum Chem.* **1979**, *16*, 1103–39.

91. Roos, B. O.; Szulkin, M.; Jaszunski, M. *Theor. Chim. Acta* **1987**, *71*, 375–84.

92. Olsen, J.; Roos, B. O.; Joergensen, P.; Jensen, H. J. A. *J. Chem. Phys.* **1988**, *89*, 2185–92.

93. Malmqvist, P. A.; Rendell, A.; Roos, B. O. *J. Phys. Chem.* **1990**, *94*, 5477–82.

94. Slipchenko, L. V.; Krylov, A. I. *J. Chem. Phys.* **2003**, *118*, 6874–6883.

95. Nakano, H.; Hirao, K. *Chem. Phys. Lett.* **2000**, *317*, 90–96.

96. Khait, Y. G.; Song, J.; Hoffmann, M. R. *Int. J. Quantum Chem.* **2004**, *99*, 210–220.

97. Roos, B. O. *In Ab Initio Methods in Quantum Chemistry II; Lawley, K. P., Ed; Wiley: Chichester, UK* **1987**, p399–445.

98. Olsen, J.; Roos, B. O.; Joergensen, P.; Jensen, H. J. A. *J. Chem. Phys.* **1988**, *89*, 5082.

99. Panin, A. I.; Simon, K. V. *Int. J. Quantum Chem.* **1996**, *59*, 471.

100. Malrieu, J.–P.; Heully, J.–L.; Zaitsevskii, A. *Theor. Chim. Acta* **1995**, *90*, 167–87.

101. Andersson, K.; Roos, B. O. *Adv. Ser. Phys. Chem.* **1995**, *2*, (Modern Electronic Structure Theory, Pt. 1), 55–109.

102. Hoffmann, M. R. *Adv. Ser. Phys. Chem.* **1995**, *2*, (Modern Electronic Structure Theory, Pt. 2), 1166–90.

103. Roos, B. O.; Andersson, K. *Chem. Phys. Lett.* **1995**, *245*, 215–23.

104. Olsen, J.; Jorgensen, P.; Helgaker, T.; Christiansen, O. *J. Chem. Phys.* **2000**, *112*, 9736–9748.

105. Khait, Y. G.; Hoffmann, M. R. *J. Chem. Phys.* **1998**, *108*, 8317–8330.

106. Kirtman, B. *J. Chem. Phys.* **1981**, *75*, 798–808.

107. Kuhler, K.; Hoffmann, M. R. *J. Math. Chem.* **1997**, *20*, 351–364.

108. Finley, J.; Malmqvist, P.–A.; Roos, B. O.; Serrano–Andres, L. *Chem. Phys. Lett.* **1998**, *288*, 299–306.

109. Murphy, R. B.; Messmer, R. P. *Chem. Phys. Lett.* **1991**, *183*, 443–8.

110. Nakano, H.; Nakatani, J.; Hirao, K. *J. Chem. Phys.* **2001**, *114*, 1133–1141.

111. Hoffmann, M. R. *Chem. Phys. Lett.* **1993**, *210*, 193–200.

112. Durand, P.; Malrieu, J. P. *Adv. Chem. Phys.* **1987**, *67*, 321–412.

113. Thomas, L. H. *Proc. Cambridge Philos. Soc.* **1927**, *23*, 542–8.

114. Fermi, E. *Z. Phys.* **1928**, *48*, 73–9.

115. Dirac, P. A. M. *Proc. Cambridge Philos. Soc.* **1930**, *26*, 376–85.

116. Teller, E. *Rev. Mod. Phys.* **1962**, *34*, 627–31.

117. Hohenberg, P. C.; Kohn, W.; Sham, L. J. *Adv. Quantum Chem.* **1990**, *21*, 7–26.

118. Kohn, W.; Sham, L. J. *Self–consistent equations including exchange and correlation effects*; Univ. of California, La Jolla, CA, USA.: **1965**; p^pp 21 pp.

119. Lee, C.; Yang, W.; Parr, R. G. *Phys. Rev. B: Condens. Matter* **1988**, *37*, 785–9.

120. Vosko, S. H.; Wilk, L.; Nusair, M. *Can. J. Phys.* **1980**, *58*, 1200–11.

121. Riley, K. E.; Op't Holt, B. T.; Merz, K. M., Jr. *J. Chem. Theory Comput.* **2007**, *3*, 407–433.

122. Raymond, K. S.; Wheeler, R. A. *J. Comput. Chem.* **1999**, *20*, 207–216.

123. Maung, N.; Williams, J. O.; Wright, A. C. *J. Mol. Struct.: THEOCHEM* **1998**, *453*, 181–189.

124. Gibson, S. T.; Greene, J. P.; Berkowitz, J. *J. Chem. Phys.* **1986**, *85*, 4815–24.

125 Seminario, J. M.; Politzer, P.; Editors, *Modern Density Functional Theory: A Tool for Chemistry. [In: Theor. Comput. Chem., 1995; 2]*. ed.; **1995**; 'Vol.' p 405 pp.

126. Moss, R. A.; Tian, J.; Chu, G.; Sauers, R. R.; Krogh–Jespersen, K. *Pure Appl. Chem.* **2007**, *79*, 993–1001.

127. Puzzarini, C.; Gambi, A.; Cazzoli, G. *J. Mol. Struct.* **2004**, *695–696*, 203–210.

128. Puzzarini, C.; Gambi, A. *Chem. Phys.* **2004**, 306, 131–141.

129. Zuev, P. S.; Sheridan, R. S. *J. Am. Chem. Soc.* **1994**, *116*, 9381–2.

130. Mlinaric–Majerski, K.; Veljkovic, J.; Kaselj, M. *Croat. Chem. Acta* **2000**, *73*, 575–584.

131. Fedorov, I.; Koziol, L.; Mollner, A. K.; Krylov, A. I.; Reisler, H. *J. Phys. Chem. A* **2009**, *113*, 7412–7421.

132. Averyanov, A. S.; Khait, Y. G.; Puzanov, Y. V. *J. Mol. Struct.: THEOCHEM* **1996**, *367*, 87–95.

133. Korkin, A. A.; Leszczynski, J.; Bartlett, R. J. *J. Phys. Chem.* **1996**, *100*, 19840–19846.

134. Mokambe, R. M.; Khait, Y. G.; Hoffmann, M. R. *J. Phys. Chem. A* **2010**, *114*, 8119–8125.

135. Jiang, W.; Khait, Y. G.; Hoffmann, M. R. *J. Phys. Chem. A* **2009**, *113*, 4374–4380.

136. Song, J.; Khait, Y. G.; Wang, H.; Hoffmann, M. R. *J. Chem. Phys.* **2003**, *118*, 10065–10072.

137. Dudley, T. J.; Hoffmann, M. R. *Mol. Phys.* **2003**, *101*, 1303–1310.

138. Devarajan, A.; Gaenko, A. V.; Khait, Y. G.; Hoffmann, M. R. *J. Phys. Chem. A* **2008**, *112*, 2677–2682.

139. Dunning, T. H., Jr. *J. Chem. Phys.* **1989**, *90*, 1007–23.

140. Kendall, R. A.; Dunning, T. H., Jr.; Harrison, R. J. *J. Chem. Phys.* **1992**, *96*, 6796–806.

141. Frisch, M. J.; Trucks, G. W.; Schlegel, H. B.; Scuseria, G. E.; Robb, M. A.; Cheesemann, J. R.; Zakrzewski, V. G.; Montgomery, J. A., Jr.; Stratmann, R. E.; Burant, J. C.; Dapprich, S.; Millam, J. M.; Daniels, A. D.; Kudin, K. N.; Strain, M. C.; Farkas, O.; Tomasi, J.; Barone, V.; Cossi, M.; Cammi, R.; Mennucci, B.; Pomelli, C.; Adamo, C.; Clifford, S.; Ochterski, J.; Peterson, G. A.; Ayala, P. Y.; Cui, Q.; Morokuma, K.; Rega, N.; Salvador, P.; Dannenberg, J. J.; Malick, D. K.; Rabuck, A. D.; Raghavachari, K.; Foresman, J. B.; Cioslowski, J.; Ortiz, J. V. B., A. G.; Stefanov, B. B.; Liu, G.; Liashenko, A.; Piskorz, P.; Komaromi, I.; Gomperts, R.; Martin, R. L.; Fox, D. J.; Keith, T.; Al–Laham, M. A.; Peng, C. Y.; Nanayakkara, A.; Challacombe, M.; Gill, P. M. W.; Johnson, C., B. W.; Wong, M. W.; Andres, J. L.; Gonzalez, C.; Head–Gordon, M.; Replogle, E. S.; Pople, J. A. *Gaussian 03, Gaussian, Inc.: Pithsburgh, PA,* **2002**.

142. Wloch, M.; Gour, J. R.; Kowalski, K.; Piecuch, P. *J. Chem. Phys.* **2005**, *122*, 214107/1–214107/15.

143. Kowalski, K.; Piecuch, P. *J. Chem. Phys.* **2004**, *120*, 1715–1738.

144. Schmidt, M. W.; Baldridge, K. K.; Boatz, J. A.; Elbert, S. T.; Gordon, M. S.; Jensen, J. H.; Koseki, S.; Matsunaga, N.; Nguyen, K. A.; et al. *J. Comput. Chem.* **1993**, *14*, 1347–63.

145. Gordon, M. S.; Schmidt, M. W. *Theory Appl. Comput. Chem.: First Forty Years* **2005**, 1167–1189.

146. Bjork, C. W.; Craig, N. C.; Mitsch, R. A.; Overend, J. *J. Am. Chem. Soc.* **1965**, *87*, 1186–1191.

147. Bushby, R. J.; Mann, S.; Jesudason, M. V. *Tetrahedron Lett.* **1983**, *24*, 4743–4.

148. Doering, W. v. E.; Rosenthal, J. W. *J. Am. Chem. Soc.* **1967**, *89*, 4534–5.

149. Rodriguez, E.; Reguero, M.; Caballol, R. *J. Phys. Chem. A* **2000**, *104*, 6253–6258.

150. Lahti, P. M.; Editor, *Magnetic Properties of Organic Materials*. ed.; 1999; 'Vol.' p 728 pp.

151. Wang, T.; Krylov, A. I. *J. Chem. Phys.* **2005**, *123*, 104304/1–104304/6.

152. Pranata, J. *J. Am. Chem. Soc.* **1992**, *114*, 10537–41.

153. Dowd, P.; Chang, W.; Partian, C. J.; Zhang, W. *J. Phys. Chem.* **1993**, *97*, 13408–12.

154. Du, P.; Borden, W. T. *J. Am. Chem. Soc.* **987**, *109*, 930–1.

155. Jadhav, R. A.; Fan, L.–S. *Environ. Sci. Technol.* **2001**, *35*, 794–799.

156. van der Hoek, E. E.; Comans, R. N. J. *Environ. Sci. Technol.* **1996**, *30*, 517–23.

157. Nelson, P. F. *Energy Fuels* **2007**, *21*, 477–484.

158. Zhao, Y.; Zhang, J.; Huang, W.; Wang, Z.; Li, Y.; Song, D.; Zhao, F.; Zheng, C. *Energy Convers. Manage.* **2008**, *49*, 615–624.

159. Staudt, J. E.; Engelmeyer, T.; Weston, W. H.; Sigling, R. **2002**.

160. Anderson, V. M.; Callomon, J. H. *J. Phys. B* **1973**, *6*, 1664–84.

161. Kushawaha, V. S.; Asthana, B. P.; Pathak, C. M. *J. Mol. Spectrosc.* **1972**, *41*, 577–83.

162. Essig, K.; Jones, H.; Ito, F.; Takeo, H. *J. Mol. Spectrosc.* **1995**, *170*, 152–7.

163. Knight, L. B., Jr.; Jones, G. C.; King, G. M.; Babb, R. M.; McKinley, A. J. *J. Chem. Phys.* **1995**, *103*, 497–505.

164. Urban David, R.; Wilcox, J. *J Phys Chem A A* **2006**, *110*, 5847–52.

165. Cheong, S. K.; Bunker, B. A.; Shibata, T.; Hall, D. C.; DeMelo, C. B.; Luo, Y.; Snider, G. L.; Kramer, G.; El–Zein, N. *Appl. Phys. Lett.* **2001**, *78*, 2458–2460.

166. Sun, L.; Bu, Y.; Yan, S. *Chem. Phys. Lett.* **2004**, *387*, 160–164.

167. Pankratov, A. N.; Uchaeva, I. M. *J. Mol. Struct.: THEOCHEM* **2000**, *498*, 247–254.

168. Kushawaha, V. S.; Asthana, B. P.; Pathak, C. M. *J. Mol. Spectrosc.* **1972,** 41, 577.

169. Theis, D.; Khait, Y. G.; Hoffmann, M. R. *J. Chem. Phys. 135*, 044117/1–044117/14.

170. Mbote, Y. E. B.; Khait, Y. G.; Hardel, C.; Hoffmann, M. R. *J. Phys. Chem. A* **2010**, *114*, 8831–8836.

171. Ebdon, L.; Pitts, L.; Cornelis, R.; Crews, H.; Donard, O. F. X.; Quevauviller, P.; Editors, *Trace Element Speciation for Environment, Food and Health*. ed.; **2001**; 'Vol.' p 391 pp.

172. Senior, C. L.; Bool, L. E.; Srinivasachar, S.; Pease, B. R.; Porle, K. *Fuel Process. Technol.* **2000**, *63*, 149–165.

173. Zhang, J.; Zhao, Y.; Ding, F.; Zeng, H.; Zheng, C. *Front. Energy Power Eng. China* **2007,** *1*, 273–279.

174. Lemly, D. A. *Ecotoxicol. Environ. Safety A* **2004**, *59*, 44–56.

175. Carrington, A.; Currie, G. N.; Levy, D. H.; Miller, T. A. *Mol. Phys.* **1969**, *17*, 535–42.

176. Verma, K. K.; Reddy, S. P. *J. Mol. Spectrosc.* **1977,** *67*, 360–73.

177. Barrow, R. F.; Lemanczyk, R. Z. *Can. J. Phys.* **1975**, *53*, 553–4.

178. Crowther, S. A.; Brown, J. M. *J. Mol. Spectrosc.* **2004**, *225*, 196–205.

179. Crowther, S. A.; Brown, J. M. *J. Mol. Spectrosc.* **2004**, *225*, 206–221.

180. Konings, R. J. M.; Booij, A. S.; Kovacs, A. *Chem. Phys. Lett.* **1998**, *292*, 447–453.

181. Mijlhoff, F. C. *Recl. Trav. Chim. Pays–Bas* **1965**, *84*, 74–80.

182. Mijlhoff, F. C. *Acta Crystallogr.* **1965**, *18*, 795–8.

183. Urban, D. R.; Wilcox, J. *J. Phys. Chem. A* **2006**, *110*, 8797–8801.

184. "Schefel; oxides". *Gmelins Handbuch der Anorganischen Chemie, Erzsbd. 3 Springer Verlag, Berlin* **1980**.

185. Steudel, R.; Sandow, T.; Steidel, J. *Z. Naturforsch., B: Anorg. Chem., Org. Chem.* **1985**, *40B*, 594–600.

186. Meyer, B., *Sulfur, Energy, and Environment*. ed.; **1977**; 'Vol.' p 448 pp.

187. Bartlett, R. J. *Annu. Rev. Phys. Chem.* **1981**, *32*, 359–401.

188. Lauderdale, W. J.; Stanton, J. F.; Gauss, J.; Watts, J. D.; Bartlett, R. J. *Chem. Phys. Lett.* **1991**, *187*, 21–8.

189. Lauderdale, W. J.; Stanton, J. F.; Gauss, J.; Watts, J. D.; Bartlett, R. J. *J. Chem. Phys.* **1992**, *97*, 6606–20.

190. Carsky, P.; Hubac, I. *Theor. Chim. Acta.* **1991**, *80*, 401–425.

191. Rittby, M.; Bartlett, R. J. *J. Phys. Chem.* **1988**, *92*, 3033–6.

192. Cizek, J. *Advan. Chem. Phys.* **1969**, *14*, 35–89.

193. Cizek, J.; Paldus, J. *Int. J. Quantum Chem.* **1971**, *5*, 359–79.

194. Wolinski, K.; Pulay, P. *J. Chem. Phys. s* **1989**, *90*, 3647–59.

195. Gauss, J.; Lauderdale, W. J.; Stanton, J. F.; Watts, J. D.; Bartlett, R. J. *Chem. Phys. Lett.* **1991**, *182*, 207–15.

196. Scuseria, G. E.; Schaefer, H. F., III. *Chem. Phys. Lett.* **1988**, *152*, 382–6.

197. Noga, J.; Bartlett, R. J. *J. Chem. Phys.* **1987**, *86*, 7041–50.

198. Noga, J.; Bartlett, R. J. *J. Chem. Phys.* **1988**, *89*, 3401.